NTNU – Trondheim
Norwegian University of
Science and Technology

Deep-seated faults and hydrocarbon leakage in the Snøhvit Gas Field, Hammerfest Basin, southwestern Barents Sea

Mohammed Seid Mohammedyasin

Petroleum Geosciences
Submission date: June 2015
Supervisor: Stephen John Lippard, IGB
Co-supervisor: Professor Ståle Emil Johansen, IPT
                  Kamaldeen Olakunle Omosanya, IPT

Norwegian University of Science and Technology
Department of Geology and Mineral Resources Engineering

Mohammed Seid Mohammedyasin

Deep-seated faults and hydrocarbon leakage in the Snøhvit Gas Field, Hammerfest Basin, southwestern Barents Sea

Master's thesis in Petroleum Geosciences

Trondheim, June 2015

Supervisor: Prof. Stephen John Lippard (IGB)
Co-supervisors: Dr. Kamal'deen Olakunle Omosanya (IPT)
                Prof. Ståle Emil Johansen (IPT)

Norwegian University of Science and Technology

Faculty of Engineering Science and Technology

Department of Geology and Mineral Resources Engineering

NTNU – Trondheim
Norwegian University of
Science and Technology

Abstract

High-quality 3D seismic data are used to analyze the history of fault growth and hydrocarbon leakage in the Snøhvit Field, southwestern Barents Sea. The aim of this work is to evaluate the role of tectonic fracturing as a mechanism driving fluid-flow in the study area. To achieve this aim, an integrated approach including seismic interpretation, multiple seismic attribute analysis, fault modeling and displacement analysis was used.

The six major faults in the study area are dip-slip normal faults which are characterized by complex lateral and vertical segmentation. The three main episodes of fault reactivation interpreted were in late Jurassic (Kimmeridgian), early Cretaceous and Paleocene times. Fault reactivation in the study area is mainly through dip-linkage. Throw-distance plots of the representative faults also revealed along-strike linkage and multi-skewed C-type profiles. The throw profiles show that faults in the study area evolved through polycyclic activity involving both blind propagation, syn-sedimentary activity and that they have their maximum displacement at the reservoir zone. The expansion and growth indices provide evidence for coeval fault activity with sedimentation and interaction of the faults with a free surface during their evolution.

Hydrocarbon-related high-amplitude anomalies in the study area have negative amplitude, reverse polarity and are unconformable with structural reflectors. The interpreted fluid accumulations are spatially located at the upper tips of the major faults and gas chimneys. Four episodes of fluid migration in the study area are linked to periods of fault reactivation and Neogene glaciations. An important piece of information from this is that fluid leakage in the Snøhvit Gas Field is driven by tectonic fracturing, uplift and erosion. The interpreted deep-seated faults are the main conduits for shallow fluid accumulations.

Preface

This thesis is submitted for the partial fulfillment of a Master Degree (MSc) in Petroleum Geosciences, specializing in Petroleum Geology during the spring semester of 2015 at the Norwegian University of Science and Technology. It mainly addresses the links between deep-seated faults and hydrocarbon leakage in the Snøhvit Field, Hammerfest Basin, southwestern Barents Sea.

Mohammed Seid

Dedication

To my sister Mushra Seid for her efforts to raise and bring me to school!

Acknowledgement

To Almighty Allah is glory for his countless blessings, 'Ni'emah', til this day!

Table of Contents

List of figures

List of tables

Abbreviations

HAA   High amplitude anomaly

RMS   Root Mean Square

URU   Upper Regional Unconformity

Ha   an arbitrary horizons that separated Unit 9 into two (U9a and U9b)

BSR   Bottom simulating reflectors

AFC   Asterias Fault Complex

TFFC   Troms-Finnmark Fault Complex

DHI   Direct hydrocarbon indicator

AVO   Amplitude versus Offset

TOC   Total Organic Carbone

TWTT   Two way travel time

U1, U2 …   Unit 1. Unit 2…..

Chapter 1 Introduction

1.1 Rationale

Fluid-flow or migration is associated with excess pore-fluid pressure which can be attributed to temporal and spatially varying processes, such as rapid sediment loading (Dugan and Flemings, 2000), uplift and erosion (Doré and Jensen, 1996), dissociation of gas hydrate (Mienert et al., 2005), polygonal faulting (Andresen and Huuse, 2011; Cartwright et al., 2007; Gay et al., 2011; Ostanin et al., 2012a), and leakage from deep and shallow source and reservoir rocks (Heggland, 1998; Hovland and Judd, 1988; Solheim and Elverhøi, 1985). Focused fluid-flow systems usually serve as conduits for fluids and sediment remobilization. They have been the interest of many studies and yet significant works are needed (Barnett et al., 1987; Cartwright et al., 2007; Dupré et al., 2010; Gay et al., 2011; Huuse et al., 2010).

Vertical migration of gas through subsurface strata can cause widely distributed acoustic low-velocity zones. The gas causes fluctuations in the compressional velocity field which again causes scattering and deterioration of the seismic wave and create regions of chaotic seismic signals (Arntsen et al., 2007). Hence, fluid-flow processes can be manifested on seismic profiles as seabed pockmarks, mud volcanoes, and methane derived carbonate mounds, and in the subsurface as seismic blow-out pipes, vertical seismic/gas chimneys, paleo-pockmarks and amplitude anomalies (Vadakkepuliyambatta et al., 2013). In the Barents Sea, glacial lineations and iceberg plough marks (Andreassen et al., 2008; Elverhøi and Solheim, 1983) are also related with the presence of gaseous hydrocarbons (Chand et al., 2008).

The flow mechanism can be triggered by the presence of stratigraphic boundaries, leaking faults and increase in seafloor temperature during fast deposition of glacio-marine sediments (Chand et al., 2012). Out of all these trigger mechanisms, the role of tectonism or faulting in hydrocarbon migration/leakage on continental margins is still poorly understood. Fluids can migrate laterally and vertically through fault zones, salt diapirs, erosional surfaces like active canyons and paloecanyons, polygonal faults or buried chimneys (Gay et al., 2011).

In the special case of the Snøhvit Field, uplift and erosion has been invoked as the major factor for fluid leakage at the detriment of tectonics and other mechanisms (Cavanagh et al., 2006; Chand et al., 2014, 2008; Laberg et al., 1998; Ostanin et al., 2012b). For example, Cavanagh et al. (2006) and Rodrigues Duran et al. (2013) proposed multiphase erosion including glacial

erosion, loading/unloading, and Cenozoic exhumation as the main causes of hydrocarbon migration in the Hammerfest Basin. On the other hand, Ostanin et al. (2013) discussed the role of fault reactivation and polygonal faulting as a mechanism driving fluid leakage in the area. Most of these works were based on basin modelling, seabed fluid flow features and shallow seismic characterization. Hence, there is an impetus to understand and further investigate the influence of deep-seated faulting as a mechanism for fluid migration in the Hammerfest Basin.

This work is therefore done to elucidate the growth history and displacement character of faults in the Snøhvit Field, their mode of reactivation and relationship with fluid migration or leakage. The study area is located in the Hammerfest Basin within longitude 71° to 72°N and latitude 21° to 24°E, between the Loppa High to the north and the Finnmark Platform to the south. It is separated from the Loppa High by the Asterias Fault Complex (AFC), from the Tromsø Basin to the west by southern segment of the Ringvassoy-Loppa Fault Complex, and from the Finnmark Platform by the Troms-Finnmark Fault Complex (TFFC) (Figure 1.1).
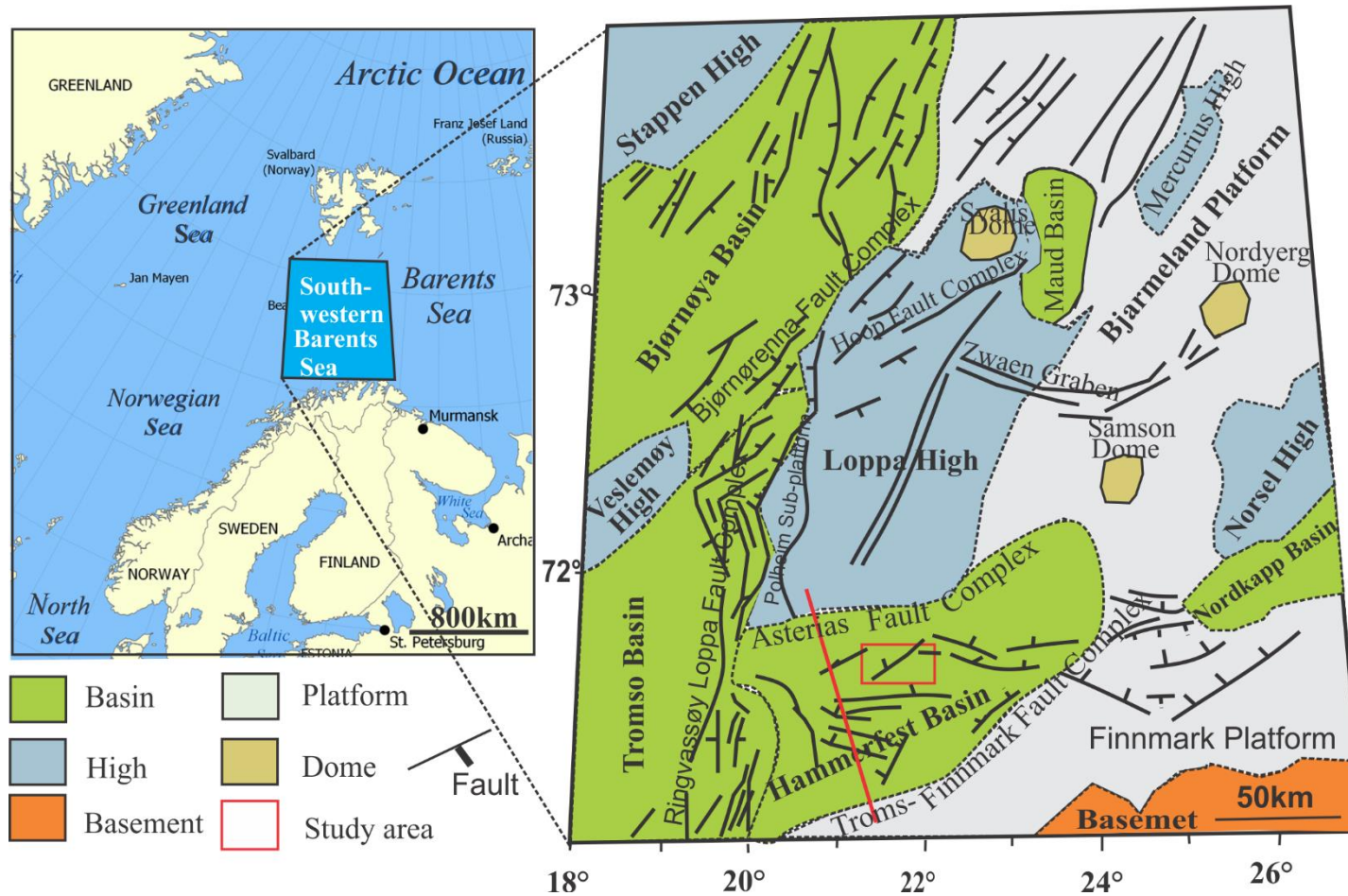
Figure 1.1 The location map and the tectonic framework of southwestern Barents Sea and the Snøhvit Field (red rectangle) within the Hammerfest Basin (modified from Gabrielsen et al.,1990; Nickel et al., 2012). *N.B: The red line is the location of Figure 2.2*

1.2 Aims of the study

- To assess the history of fault growth using multiple approaches including seismic interpretation, seismic attribute analysis and fault displacement analysis
- To find evidence for fluid leakage by mapping seismic high-amplitude anomalies
- To investigate and link fault activity as a mechanism for fluid leakage in the study area.
- To understand timing of hydrocarbon leakage, their driving mechanisms and overall fluid plumbing system.

1.3 Analysis of fluid flow features on seismic reflection data

Fluid flow features on seismic data can be visualized as gas chimney and seismic pipes, high-amplitude anomalies (HAAs), buried and seabed pockmarks.

1.3.1 Gas chimneys

Gas chimneys are acoustic maskings which create dimmed and distorted amplitudes and does not show any clear stacking unlike seismic pipes which show vertical stacking of high or low amplitude anomalies (Andresen, 2012; Berndt, 2005; Løseth et al., 2011, 2001; Moss and Cartwright, 2010). They are described in different ways in the literature as columnar disturbances, wipeout zones, dimmed and distorted amplitudes in seismic data (Andresen and Huuse, 2011; Berndt, 2005; Heggland, 1998; Heggland et al., 1999; Hustoft et al., 2010; Løseth et al., 2009). The gas chimneys in this study are associated with high-amplitude anomalies (HAAs) at their roof zones (Figure 1.2a).

1.3.2 Seismic high-amplitude anomalies (SHAA)

Seismic high-amplitude anomalies represent the change in acoustic properties related to lithology or sub-surface fluid accumulations (Alves et al., 2015; Calvès et al., 2008; Løseth et al., 2009). Direct hydrocarbon indicators (DHI's) such as bright spots, flat spots, polarity reversal etc., are seismic high-amplitude anomalies related to hydrocarbons in the subsurface (Løseth et al., 2009). High-amplitude anomalies (HAAs) can have opposite polarity to the seabed i.e., "soft-on-hard" anomalies or similar in polarity with the seabed, "hard-on-soft" anomalies (Alves et al., 2015) (Figure 1.2b & c).
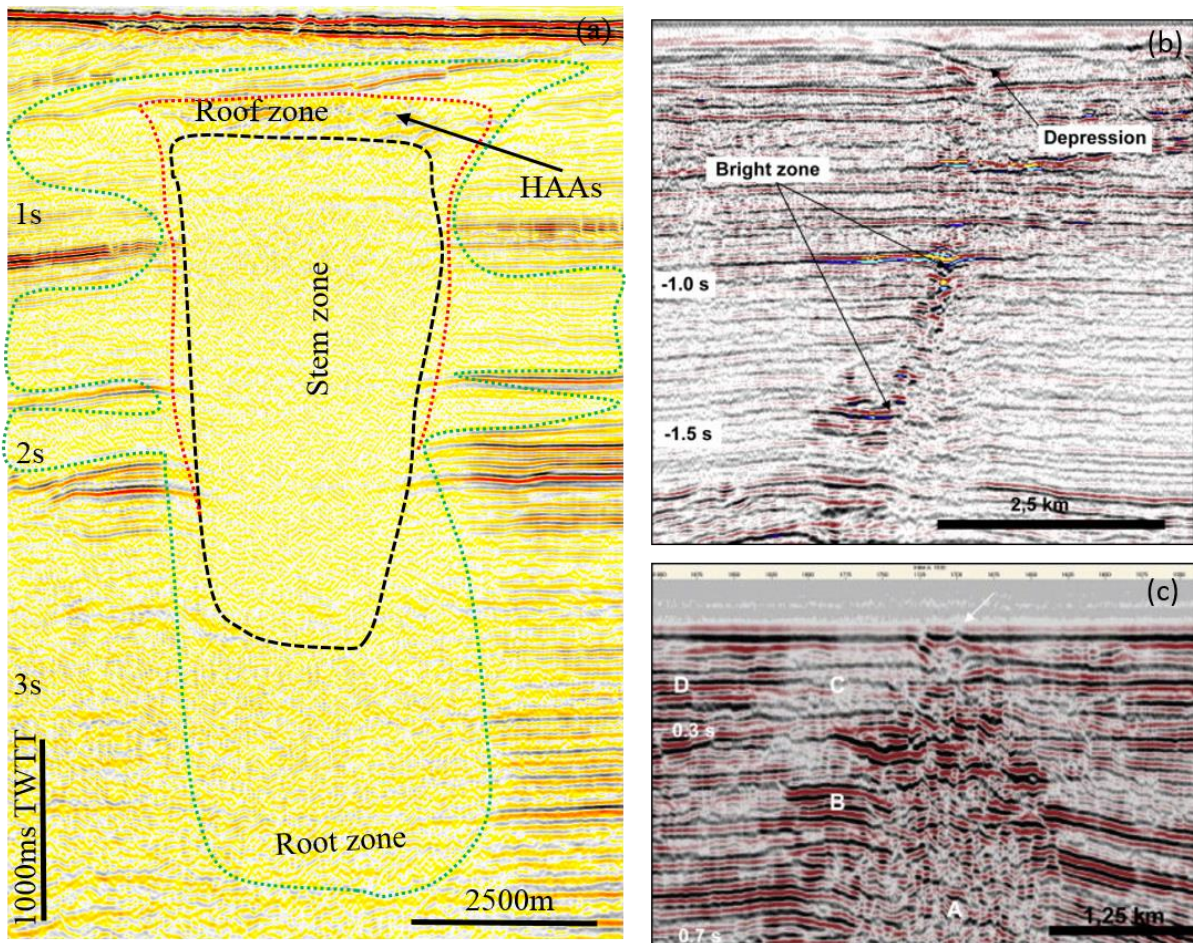
Figure 1.2 Gas chimney and high-amplitude anomalies . Gas chimney root, stem and roof zones are outlined and the green line indicates lateral migration along permeable formations or gas charging into sediments in this study area (b) Vertically stacked high-amplitude anomalies in the hanging-wall part of a fault in response to upward gas leakage along the fault zone (c) Acoustic masking related to gas chimney (A), surrounded by high amplitude (B), and outer zone of dim amplitude anomalies (C) related to gas charged slightly permeable layers and evenly distributed gas in sediments, respectively (Løseth et al., 2009).

1.3.3 Pockmarks

Pockmarks are isometric cone to sub-circular shape depressions on the seafloor (Figure 1.3). The accepted conceptual model of pockmark formation is by upward migration of gas through faults and fractures in sediments which forms gas accumulation pockets in the near-seabed. Further accumulation results in doming and tensional fractures on the sea floor leading to the formation of unit pockmarks (Hovland and Judd, 1988). The coalescence of these unit pockmarks in time forms numerous composite pockmarks. However, the type of fluid can be any fluid. Different conceptual models have been tested in order to understand about pockmark forming mechanisms. Pockmarks form by fluid escape and first proposed by Josenhans et al.,

(1978) can be into two modes; (1) by catastrophic eruption of gas from overpressured shallow gas accumulations, and (2) continuous fluid discharge hindering or dissolving sediments around the seep (Hovland and Judd, 1988; Pilcher and Argent, 2007). The failure of the capillary pressure was suggested as the main cause for the formation of the pockmarks. Seal fails when buoyancy pressure exceeds the capillary pressure during hydrate crystallization and gas accumulations, which leads to the formation of large escape of gases to the seafloor initiating dissolution of the surrounding sediment by ocean water and forms pockmarks (Cathles et al., 2010). The linear arrangement of pockmarks indicates their association with fault zones (Haskell et al., 1999).
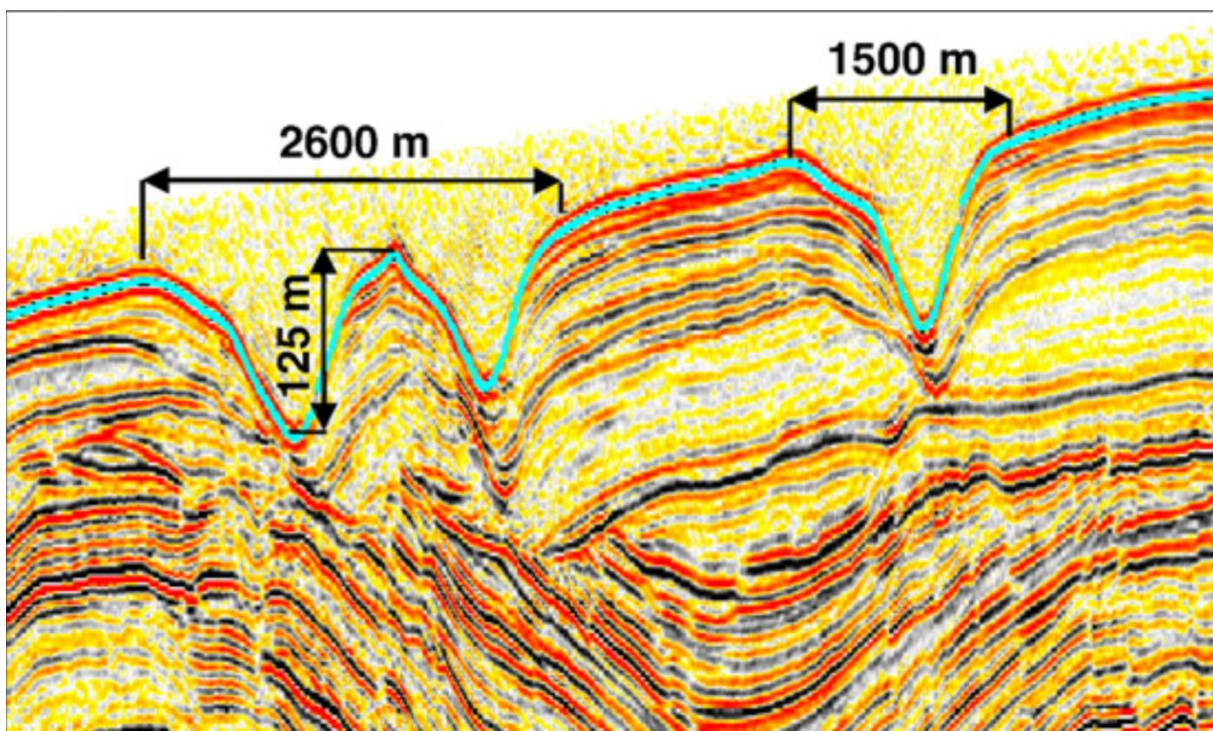
Figure 1.3 Pockmarks of different sizes (West African continental margin) forming depressions on the seabed (Pilcher and Argent, 2007).

1.4 Fluid plumbing systems

Deep-sourced hydrocarbon plumbing systems are often sourced from thermogenic gas migration and shallow sourced gas migration can be from organic gas (Andresen and Huuse, 2011; Andresen, 2012; Ostanin et al., 2012b). The main trigger and driving mechanisms are: thermogenic maturation, salt tectonics, sedimentary loading and sea-level fluctuations (Andresen, 2012; Jolly and Lonergan, 2002). Timing of the main faulting and reactivation

phases can be use to predict periods of fluid-flow if the hydrocarbon has been mature before (Figure 1.4).
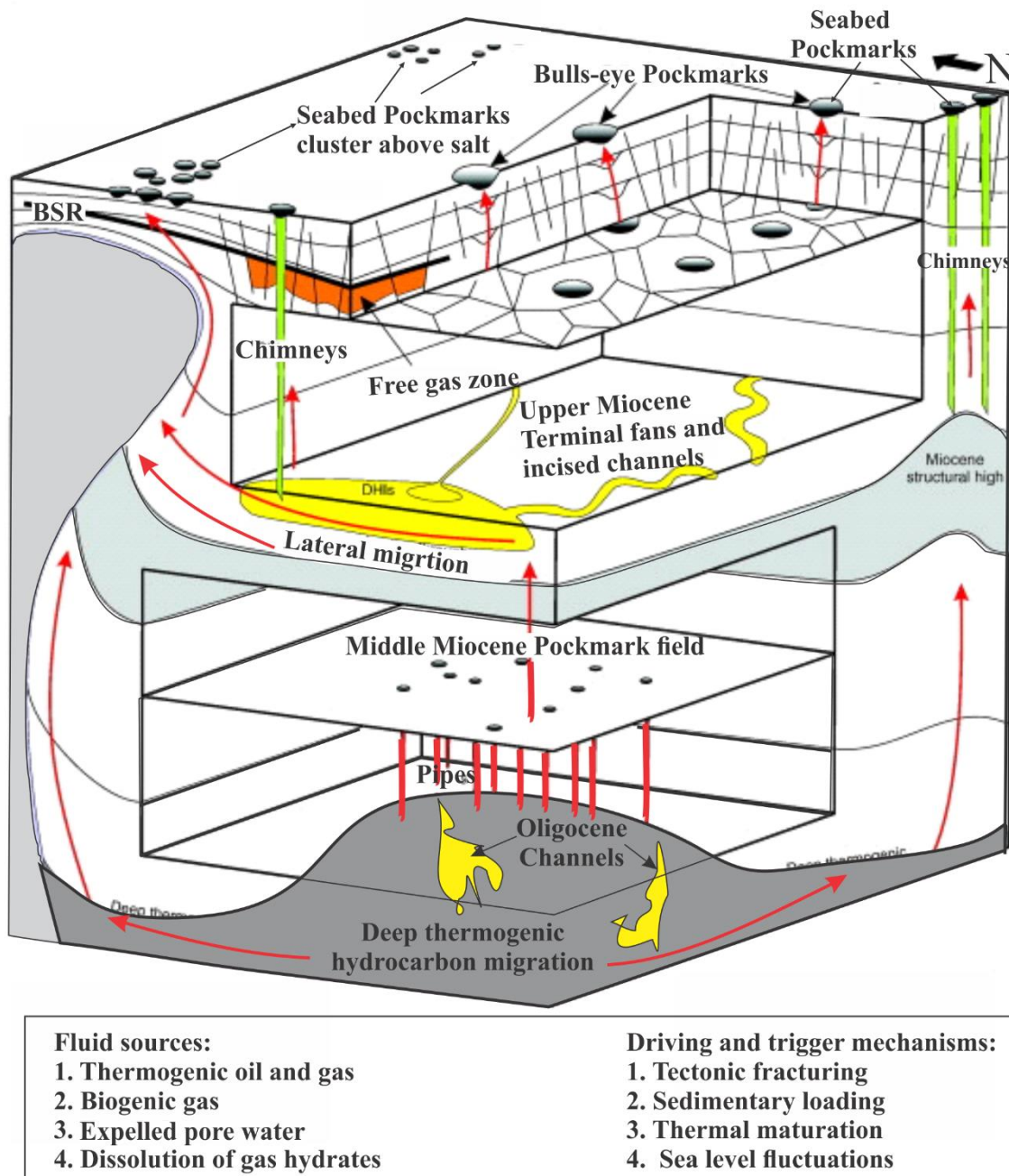
Figure 1.4 Hydrocarbon plumbing systems (Lower Congo Basin, offshore Angola) illustrating the fluid sources, migration pathways and the resulted fluid flow features in the subsurface and on the seabed (modified from Andresen, 2012).

1.5 Analysis of fault nucleation, growth, linkage and reactivation

Traditional fault analysis was based on simple blind faults (Watterson, 1986). Displacement distributions along normal blind faults usually show maximum displacements (d_{max}) at the centre of the fault plane, gradually decreasing towards the tips (Barnett et al., 1987). Individual blind faults have symmetrical and directionally skewed displacement-distance (t-x) plots in the fault initiation stage (Figure 1.5c). Displacement profiles may vary from mesa-type, cone-type to hybrid profiles comprising both C- and M-types (Kim and Sanderson, 2005; Muraoka and Kamata, 1983). The position of d_{max} for C-type profiles corresponds to the nucleation point where fault propagation was initiated (Mansfield and Cartwright, 1996).

However, in complex tectonic settings faults can have complicated nucleation, growth and reactivation histories (Bellahsen and Daniel, 2005; Walsh et al., 2002). This produces complex geometries and displacement patterns of the faults. Syn-sedimentary faults on the other hand can have upward increasing throw-depth profiles (Figure 1.5b). Hybrid displacement and distance plots suggest fault linkage and segmentation (Walsh and Watterson, 1989). Elliptical fault displacement profiles are consistent with the propagation of blind faults (Baudon and Cartwright, 2008).

After initial growth, different faults can be reactivated along the dip-slip direction and linked at displacement minima (Figure 1.5a & d). Fault reactivation along the dip and interaction along the strike directions can significantly modify the throw and displacement profiles, respectively. Similarly, lateral growth and interaction of faults can result into different fault segments along strike (Figure 1.5e). Linkages of the segments merge some of the segments during interaction (Figure 1.5f). Finally, all the segments can join together to form a through-going larger fault (Figure 1.5g). Analyzing these profiles can provide hints into the growth history of faults and their consequence on hydrocarbon migration.
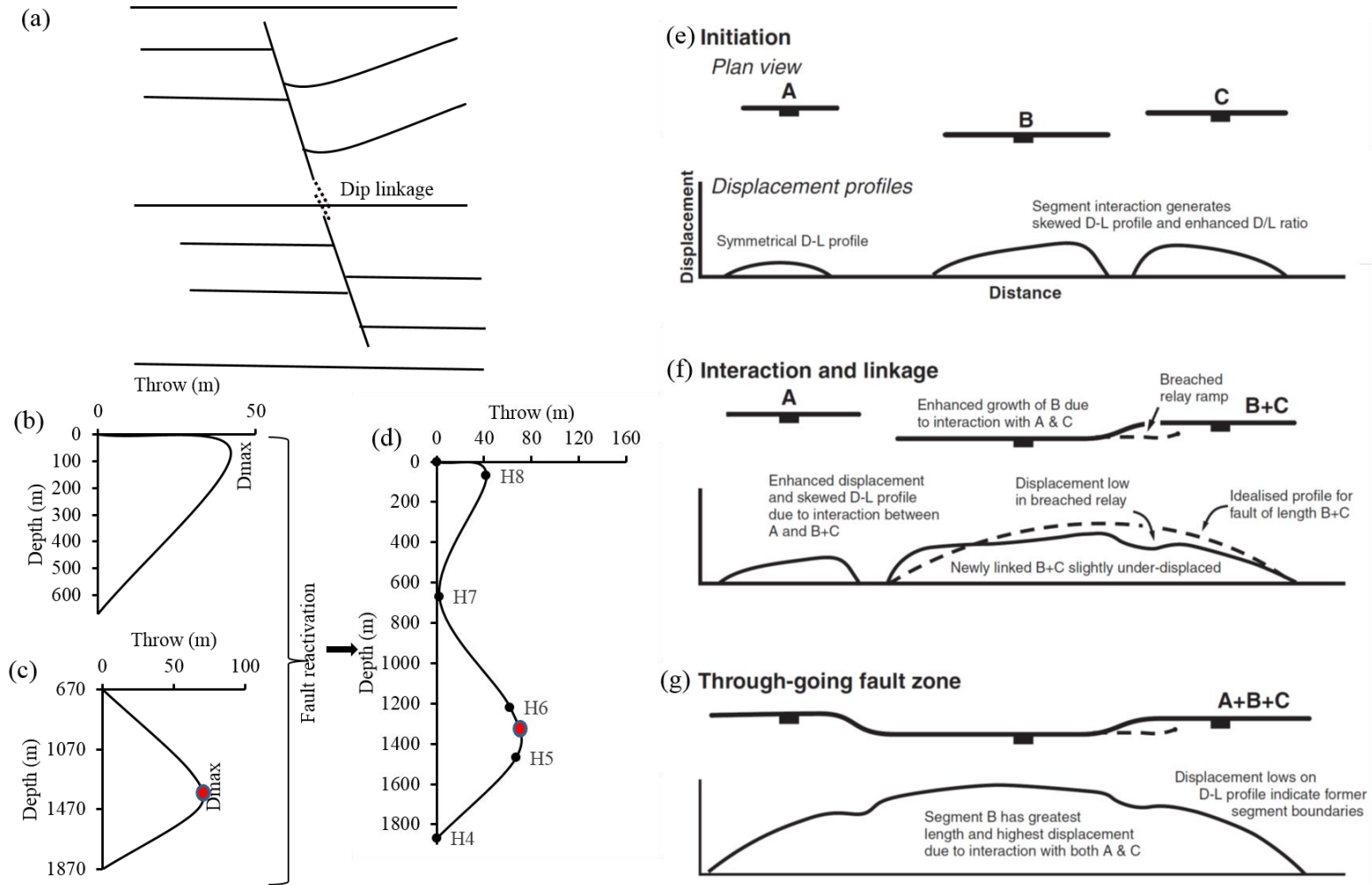
Figure 1.5 Fault reactivation and interaction during fault growth: (a) fault reactivation is in the dip direction (b) throw-depth profile for syn-sedimentary fault, (c) isolated/blind faults and (d) dip linkage of the faults in (b) and (c). Fault interaction along the strike direction in three stages, i.e. (e) initiation (f) interaction and linkage along the strike and (g) through-going fault stages (Gawthorpe and Leeder, 2000).

1.6 Thesis structure

This thesis is divided into five chapters; introduction, regional geological setting of the area, data and methods, results, and discussion and conclusions, respectively. The content of each Chapter is highlighted in Table 1.1.

Table 1.1 The structure of the thesis and the main contents in each of the Chapters.

	Content
Chapter 1	• This chapter gives a brief overview about hydrocarbon migration on continental margins and also provides the rationale and aims of this work • Introduces fluid flow features • Gives the background to fault nucleation and growth through graphical illustrations
Chapter 2	• Briefly summarizes the tectonics of the southwestern Barents Sea area • Summarizes the stratigraphy and depositional environment of the study area • The source, reservoir and seal rocks are systematically summarized from previous works
Chapter 3	• The work flow and the methods used for this study • 3D seismic stratigraphic and fault interpretation • Mapping of high-amplitude anomalies
Chapter 4	• This chapter is divided into three main parts as it presents the main results from: (1) seismic stratigraphic interpretation; (2) fault analysis and displacement plots (t-z, t-x, EI and GI), (3) Seismic high amplitude anomalies
Chapter 5	• The main results and findings are discussed by emphasizing fault reactivation and growth history, and controls of the deep-seated faults on hydrocarbon migration from the source to the shallow subsurface. Based on this the main sources of hydrocarbons are identified and timing of migration phases are reconstructed • Finally, the main conclusions of this work are drawn; recommendations and future research directions are suggested

Chapter 2 Geological Setting

2.1 Tectonic evolution of the southwestern Barents Sea

The tectonic history of the western Barents Sea (Figure 2.1) can be traced back to the Caledonian Orogeny that strikes through northernmost Norway and northeastwards into the Barents Shelf (Barrère et al., 2009; Breivik et al., 2005, 2002; Gee et al., 2008; Gernigon and Brönner, 2012; Gernigon et al., 2014; Gudlaugsson et al., 1998; Marello et al., 2013; Ritzmann and Faleide, 2007; Roberts, 2003). The Caledonian fabric is obscured in most parts of Barents Sea, except on Svalbard by late Proterozoic and Mesozoic sedimentary basins (Breivik et al., 2002; Gee et al., 2008).

Extensional tectonics during late Palaeozoic in the western Barents Sea segmented the basins into fan-shaped array of block-faulted basins separated by highs (Faleide et al., 1984; Gudlaugsson et al., 1998; Rønnevik and Jacobsen, 1984). The Upper Carboniferous to Lower Permian shallow marine carbonate with evaporite deposits are overlain by late Permian clastic deposition in response to Uralian Orogeny (Johansen et al., 1992).

Triassic crustal extension in the North Atlantic and locally important differential compaction over the late Paleozoic grabens has played an important role in accommodation space development (Glørstad-Clark et al., 2010). Intense rifting in mid Jurassic to early Cretaceous occurred in the southwestern Barents Sea (Faleide et al., 2008, 1993). Westward shift in extensional rifting increased the amount of megasequences with time towards the present day continental-ocean boundary in the southwestern Barents Sea (Klitzke et al., 2014).

In late Cretaceous to Paleocene continental breakup between Norway and Greenland was taken up by strike-slip movements along the De Geer Zone. The southwestern Barents Sea margin developed during the Eocene opening of the Norwegian-Greenland Sea (Breivik et al., 1998; Faleide et al., 2008). Deep marine conditions persisted in the SW Barents Sea throughout Eocene time, with deposition of significant sandy submarine fans during the Middle Eocene (Ryseth et al., 2003). The passive margin evolved in response to subsidence and sediment loading during the widening and deepening of the Norwegian-Greenland Sea. Sedimentation was modest until the late Pliocene when the Northern Hemisphere glaciation led to rapid progradation. Increase in sedimentation rate formed huge, regional depocentres near the shelf edge offshore Mid-Norway and in front of bathymetric troughs in the northern North Sea and

western Barents Sea (Faleide et al., 2008). Uplift and glacial erosion during Pliocene to Pleistocene (Dimakis et al., 1998; Doré and Jensen, 1996; Dörr et al., 2012; Faleide et al., 1996; Green and Duddy, 2010; Henriksen et al., 2011; Vorren et al., 1991) has evolved the deep marine fans in the adjacent oceanic domains along the northern and western passive margins (Knies et al., 2009).

2.2 Evolution of the Hammerfest Basin

The graben in the Hammerfest Basin has been affected by the extensional tectonics in the Carboniferous (Berglund et al., 1986) and further evolved during the Caledonian orogenic collapse (Gernigon et al., 2014; Ritzmann and Faleide, 2007). This causes tilting of the Loppa High and Hammerfest Basin in late Carboniferous to early Permian with reactivation of the underlying basement fault trends (Figure 2.2). Differential basin subsidence with depocenters in the northeastern and southwestern part of the Hammerfest Basin during Permian coincided with the reactivation of the Troms-Finnmark Fault Complex and showed that the Asterias Fault Complex was not active during this period (Berglund et al., 1986).

Well defined early Triassic sediments onlap on north-south oriented structural highs and indicate their tectonic reactivation during this period. The post-rift erosion during the Cretaceous over the Loppa High and local tectonic uplift has caused deep erosion into Triassic in the western part of the AFC. Intense syn- and post-rift erosion during the Cretaceous resulted a locally thinner basin towards its center and thicker towards the periphery of the basin. The late Triassic was a period of quiescence and deposition. From late Triassic to mid Jurassic deposition was controlled by the interplay of tectonic subsidence, eustatic sea level and sediment input. The mid Jurassic represents a change from sandstones to shales across the Bathonian–Callovian unconformity (Breivik et al., 1998). Sea level rise during mid Jurassic led to the deposition of the Stø Formation (Berglund et al., 1986). This formation is the main reservoir in the Snøhvit Field, and represents a tectonically controlled transgressive wave-dominated estuary (Ottesen et al., 2005). Subsequent erosion of structural highs and deposition was restricted to both shallow and deep marine deltas along the northern and southern margins of the basin (Ottesen et al., 2005). However, the initial sediment distribution was controlled by doming accompanied by E-W trending normal faulting (Faleide et al., 1984) and with the formation of horst and graben structures. During late Jurassic the Hekkingen Formation was deposited (Berglund et al., 1986).

Marine sedimentation started as a result of transgression of the central part of the Hammerfest Basin during mid Palaeocene. A SSW progradation of sediment from the platform areas to NNE of the basin occurred during the late Palaeocene. Subsidence and continued erosion was dominant during Oligocene and Miocene (Knutsen and Vorren, 1991).

2.3 Stratigraphy and depositional setting of the Snøhvit Field

The Snadd Formation depositional environments range from offshore through shelf and shallow marine to paralic and fluvial (Figure 2.1). Flooding surfaces are used to divide the formation into stratigraphic level and sequences stratigraphic hierarchies.

The Middle to Upper Triassic formations are characterized by interbedded shales and sandstones that contain coal fragments and carbonaceous rocks overlain by shaly and silty units that contain increasingly interbedded sandstones upward (Linjordet and Olsen, 1992).

The early to mid-Jurassic formations are characterized by shallow marine to coastal plain depositional environments with fluctuating coastlines. They consist of the Tubåen, Nordmela and Stø Formations, stratigraphically from bottom to top (Figure 2.1). The Tubåen Formation has thick sandstone bodies with thin shale beds. It is conformably overlain by silty shales and very fine grained sandstones of the Nordmela Formation. The Nordmela Formation consists of fining upward sandstones and is conformably overlain by the Stø Formation (Figure 2.1). Between the mid to late Jurassic a major hiatus was observed from five wells drilled in the Snøhvit area. The hiatus is followed by organic rich shales of the Hekkingen Formation deposited on a marine shelf with anaerobic bottom water conditions (Linjordet and Olsen, 1992).
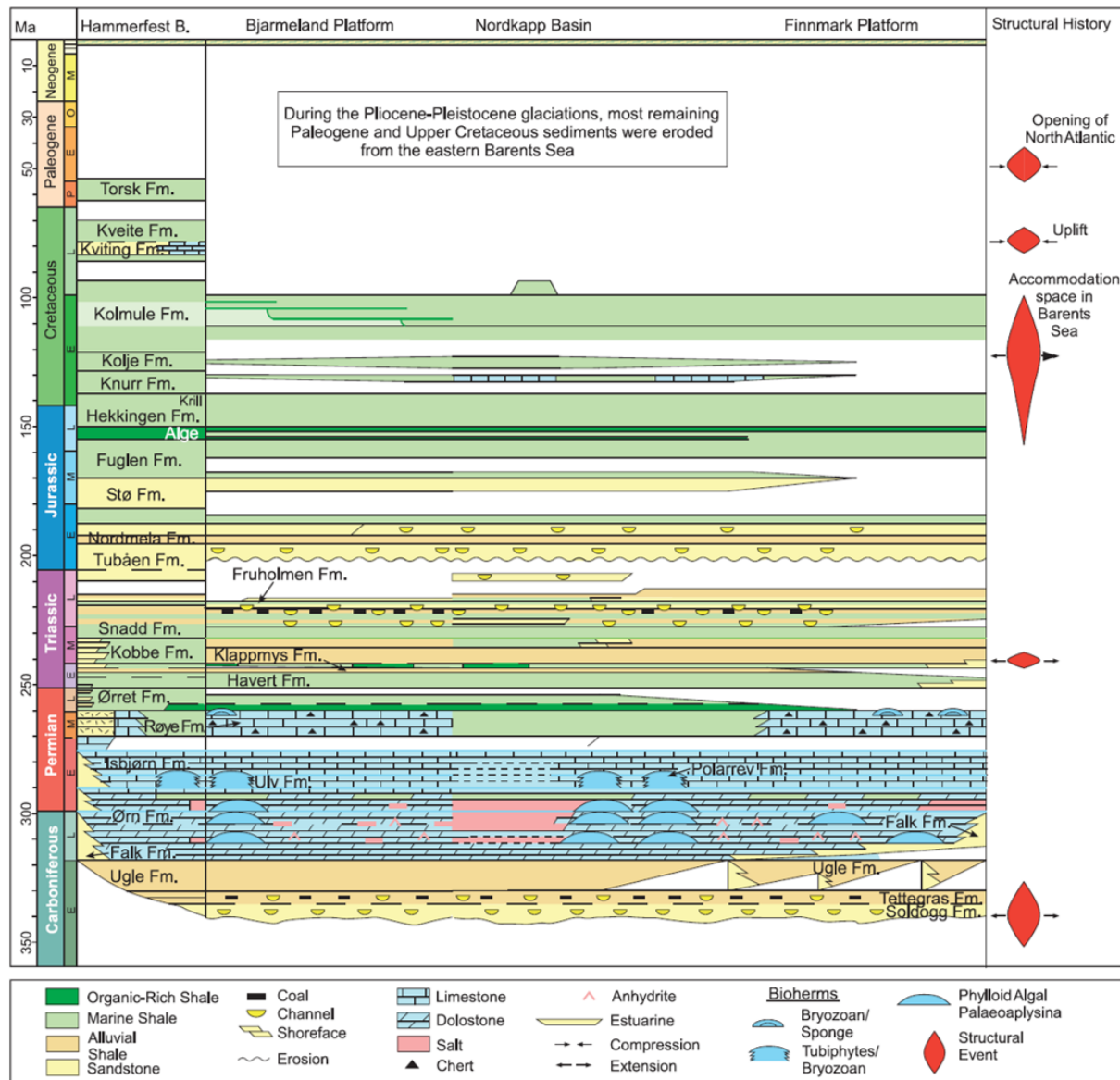
Figure 2.1 Lithostratigraphy of the Hammerfest Basin , modified from (Ohm et al., 2008), major hiatuses/erosion events are left blank in the stratigraphic column.

The second hiatus is between the Upper Jurassic and Lower Cretaceous strata and the third is between the Lower and Upper Cretaceous strata. The Cretaceous stratigraphy is dominated by by shales and claystones with thin sandstone and siltstone, and interbedded limestones with claystones to the top parts. The fourth hiatus is between the Cretaceous and Tertiary strata (Linjordet and Olsen, 1992) and followed by the claystones. Paleocene to Eocene claystones containing stringers of sand, siltstone, dolostone and tuffs are dominant at the base and soft clay to the upper part of the Pliocene to Pleistocene sequences, separated by a major hiatus (Linjordet and Olsen, 1992). The several phases of glacial erosion have removed the Eocene to Miocene

sediments, and followed by deposition of the claystone and sandstone dominated Nordland Group at the top.

2.3.1 Source, reservoir and seal rocks

The Hekkingen, Nordmela, Snadd and Kobbe Formations are the potential source rocks in the Hammerfest Basin, and in particular for the Snøhvit Field (Linjordet and Olsen, 1992). The Upper Jurassic Hekkingen formation is the most prolific oil prone source rock with 10% organic carbon (TOC) (Rodrigues Duran et al., 2013), hydrogen index (HI) goes upto 300 mgHC/g TOC, and hydrocarbon negative index (S2). The Hekkingen Formation was deposited under marine conditions but mixed with terrestrial sediment influx. The variation reflects the distance of the paleocoastline and terrigeneous influx in anoxic conditions in the early diagenetic phase (Ohm et al., 2008). It is dominated by mixed organic sources, and has reached to the oil window in the Snøhvit and Goliat Fields. The hydrocarbon maturation in this formation is reached the oil window in the Snøhvit field. Even though most of the hydrocarbon is generated in the Hekkingen Formation, its contribution to the reservoirs is restricted by the underlying seal rock (Fuglen Formation) and most of the migration out of the source rocks is from the Hekkingen Formation (Rodrigues Duran et al., 2013).

The Nordmela Formation has less variation in maturity and input organic matter than the Hekkingen Formation. It is dominated by alluvial shale containing kerogen which influenced by terrestrial organic matter (OM).The Snadd Formation has a wide variation in depositional environment within the mixed organic sources or transitional environment area, and terrestrial to marine environment, while the Kobbe Formation is more influenced by organic sources in which the terrestrial inputs were restricted (Ohm et al., 2008).

The Stø and Tubåen Formations are the main reservoir rocks. The Stø Formation is the main reservoir in the Hammerfest Basin, and also in the Snøhvit Field, dominated by moderately well-sorted mature sandstones. It was deposited in prograding coastal regimes with marked shale/siltystone intervals within the sand layers that represent regional transgression in the late Toarcian and late Aalenian (Dalland et al., 1988). The Tubåen Formation is dominated by sandstone with subordinate shales and minor coals. The upper and lower parts are sand rich and separated by a shaly interval. It believed that this formation was deposited in high energy marginal marine environment (Dalland et al., 1988).

The Fuglen and upper part of the Hekkingen Formations are the seal rocks. The Fuglen Formation is dominated by mixed organic sources and slightly less marine environment than the Hekkingen Formation (Ohm et al., 2008). It is characterized by pyritc mudstones with interbedded thin brownish limestones (Dalland et al., 1988). The Triassic source rocks, Snadd and Kobbe Formations, are generally oil mature and over mature to gas mature in the Hammerfest Basin. The TOC content for the Snadd and Kobbe Formations goes upto 2% and 3% and HI of 150 mgHC/g TOC and 200 mgHC/g TOC, respectively. The shallow depth gas anomalies would be the result of large volume gas migration form the Triassic source rocks and an upward migration of gas from the Hekkingen Formation due to lack of top seal layers (Rodrigues Duran et al., 2013).
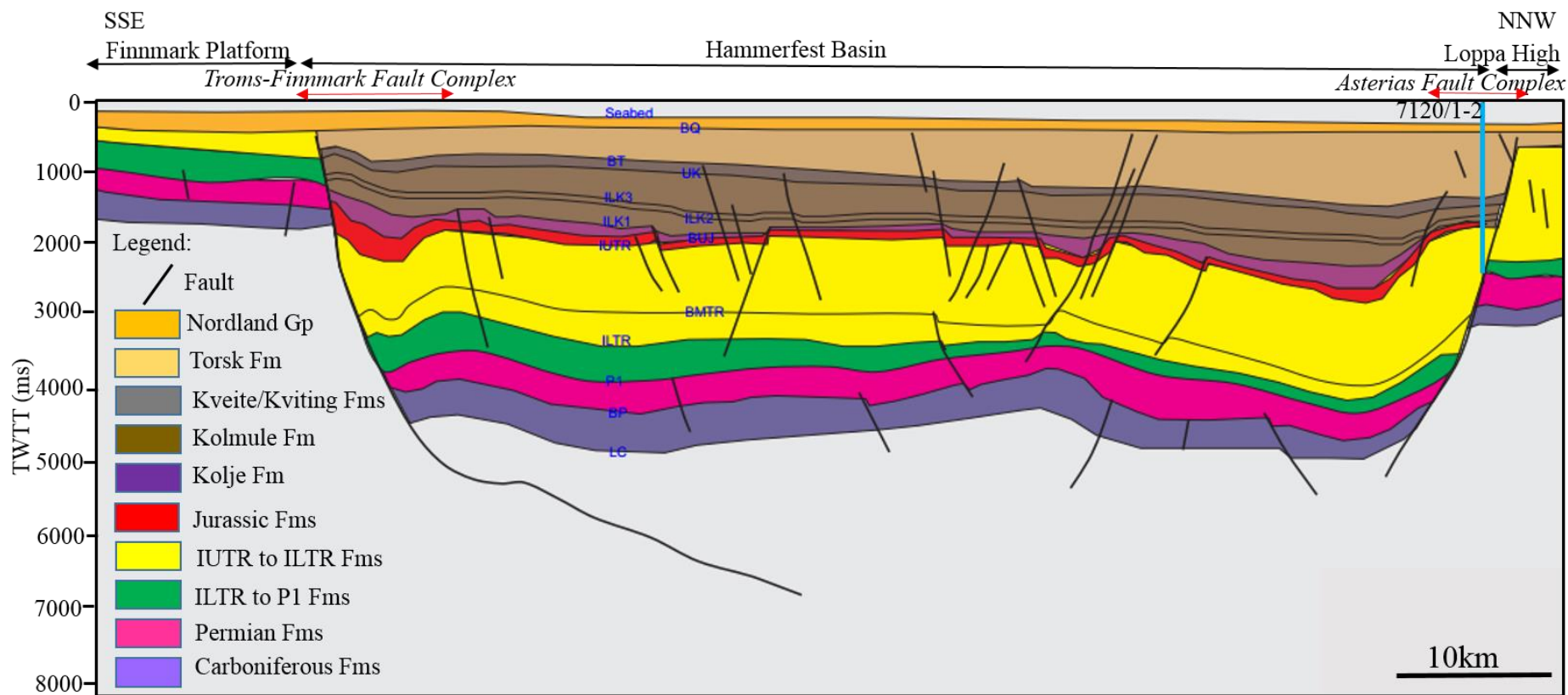
Figure 2.2 Stratigraphy of dip line BSSO1-104 showing the Hammerfest Basin , the Troms-Finnmark Platform and the Loppa High separated by the Troms-Finnmark Fault Complex and Asterias Fault Complex respectively (Modified from Gabrielsen et al., 1990). Where LC: Lower Carboniferous; BP: Base of Permian; P1: top of Permian; ILTR: Intra-lower Triassic; BMTR: Base of Middle Triassic; IUTR: Intra-upper Triassic; BUJ: Base of Upper Jurassic; ILK1, ILK1, ILK2 & ILK3 are Lower Cretaceous; UK: Upper Cretaceous; BT: Base of Triassic and BQ: Base of Quaternary.

Chapter 3 Data and Methods

3.1 Three-dimensional seismic data

This study uses a pre-stack time-migrated (PSTM), zero-phase 3D seismic data covering an area of approximately 486 km^2 in water depths of 250 to 3600 m in the Snøhvit Field. The study area is located in the Hammerfest Basin, SW Barents Sea (Figure 1.1), within latitude 71°28'17" to 71°43'40" and longitude 20°16'43" to 21°43'53". The seismic data (SIS FM TVFGC) was processed by Geco-Prakla, Stavanger, in 1997. It consists of 825 inlines and 3775 crosslines, each measuring approximately 47 km and 10 km in length. The inlines are oriented in NNE-SSW direction perpendicular to fault strike while the crosslines are oriented parallel to fault strike. The vertical sampling interval and bin spacing for the seismic volume are 4 ms and 12.5 x 12.5 ms, respectively.

The data is displayed in SEG normal polarity (American convention), such that a downward decrease in acoustic impedance corresponds to a negative amplitude reflection or trough and a downward increase in acoustic impedance is represented by positive amplitude reflection or peak. Troughs in this work are displayed as red reflectors while the white and black reflectors represent the zero crossings and peak, respectively.

Zero-phase seismic data are the most widely used in seismic interpretation work because (1) time and amplitude are co-located, (2) symmetrical wavelet with the majority of the energy being concentrated in the central lobe, (3) the time of tracked horizons coincides with the travel time of the subsurface interface causing the reflection, and (4) the resolution is better than other wavelets of the same content in frequency (Brown, 2004; Brown, 2008). Zero-phase seismic data are characterized by symmetrical wavelet, maximum amplitude at the center of the wavelet and have better resolution than minimum phase (Figure 3.1). However, acquisition and processing are mostly done in minimum phase which are phase shifted to enhance interpretation especially stratigraphic interpretation.

The data quality is affected by acoustic masking in the western and northern parts of the seismic volume. It was impossible to pick the faults and horizons within and across these locations. Besides, the data quality is also affected by the intense faulting in the western part of the field (Figure 3.2). The reflectors in the Triassic, Permian and Carboniferous successions are also

19

lacking continuity, which makes it difficult to pick the horizons with a high degree of confidence.
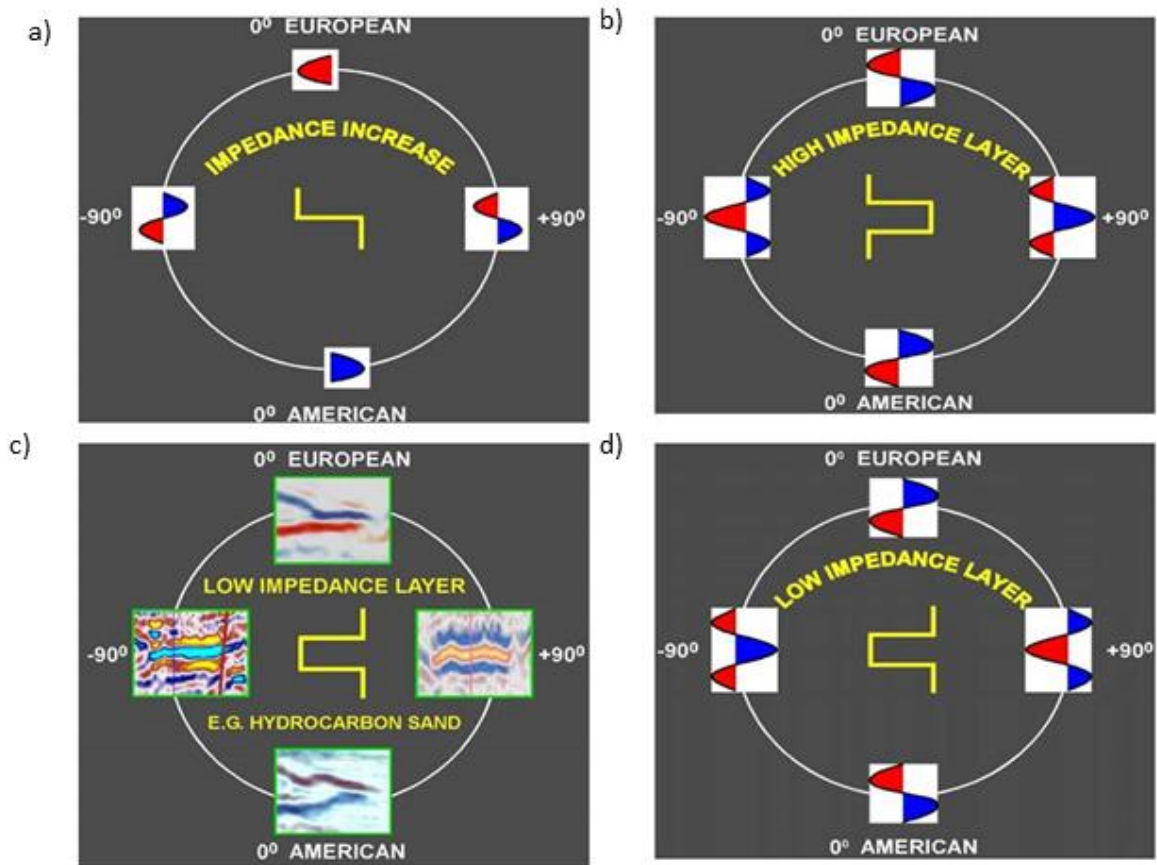
Figure 3.1 Phase and polarity standards (Brown, 2008). A shift in polarity in European and American convention is represented differently for zero-phase and ±90 phases. For zero-phase, an increase in acoustic impedance displayed as peak (red) in the European convention and trough (blue) in American convention (a) , such as in carbonate (b) while when the wave pass from high to low acoustic impedance (c & d) the reverse will be displayed, such as in hydrocarbon sand (c & d). The shift in polarity can also be displayed as +90 or -90 polarity and each of them has different representation in American and European conventions.
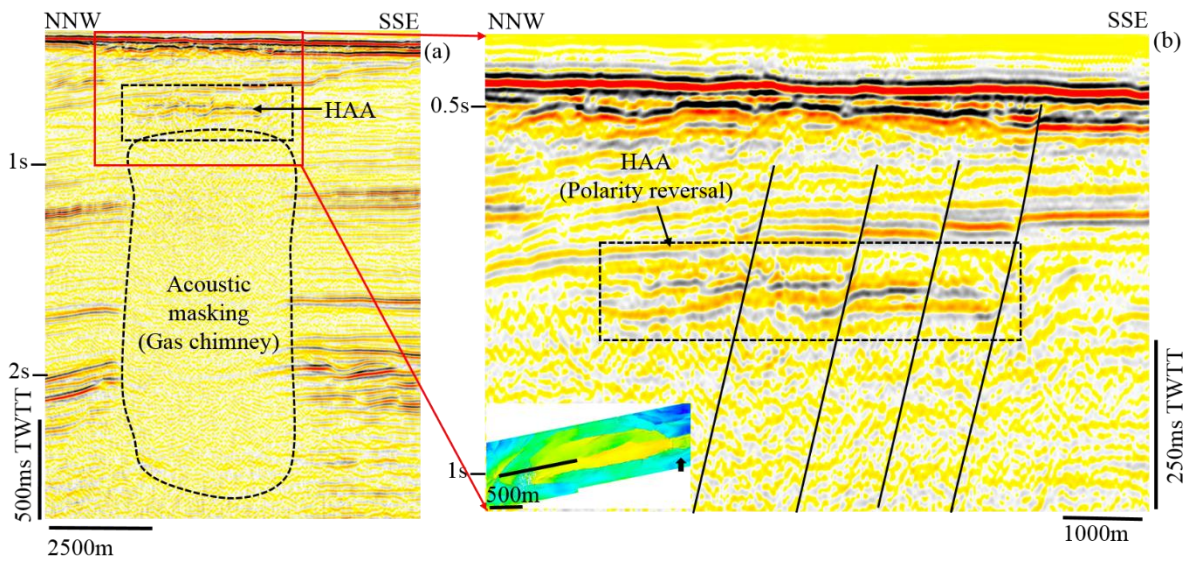
Figure 3.2 Acoustic masking *(gas chimney)* at southwestern part of the field affected continuity of the horizons and the degree of confidence in the seismic interpretation. Acoustic masking in the study area is related to gas or fluid leakage from the subsurface. The location of the seismic line is shown in (b). N.B: *TWTT-Two Way Travel Time, HAA- High-amplitude Anomaly.*

3.1.1 Seismic resolution

Seismic resolution is the ability to distinguish between two separate objects in order to be seen in seismic data. The seismic resolution is dependent on the wavelength (λ) which in turn is inversely proportional to the frequency (*f*) and the velocity of the wave. The minimum wavelength in order to distinguish two discernible features should be one fourth of the wavelength (Brown, 2004). Hence, low frequency data has lower vertical resolution than high frequency data of the same object while high frequency seismic can resolve smaller features better. For the seismic volume used in this thesis, vertical resolution is 10 m and 15 m using average velocity of 2000 m/s TWTT and a dominant frequency of 50 Hz (*see equations 1 and 2*).

The horizontal resolution refers to the minimum lateral proximity between two points that can still be recognized as individual points rather than one (Yilmaz and Doherty, 1987). Horizontal or lateral migration depends on the spacing of the recording hydrophones and the width of the Fresnel zone. For a perfectly migrated seismic reflection data, the lateral resolution is equal to the bin spacing which is 12.5 m for the seismic cube used in this work. Migration enhances

lateral resolution; specifically the pre-stack and depth migrations have better lateral resolution than post-stack and time migrations, respectively.

$$\lambda = \frac{v}{f} \dotfill \text{eq.1}$$

$$\lambda = \frac{2000}{50} = 40 \text{ m for shallower horizons at velocity of 2000 m/s TWTT}$$

$$\lambda = \frac{3000}{50} = 60 \text{ m by assuming 3000 m/s TWTT for deeper horizons}$$

$$t = \frac{\lambda}{4} \dotfill \text{eq.2}$$

$$t = \frac{40}{4} = 10 \text{ m for shallower horizons}$$

$$t = \frac{60}{4} = 15 \text{ m for deeper horizons}$$

3.2 Borehole or well data

Five exploration wells were used for stratigraphic correlation and depth conversion. The wells include 7120/5-1, 7120/6-1, 7120/6-2 S, 7121/4-1 and 7121/5-1 (Table 3.1). Important wireline logs such as sonic (us/ft), density (g/cc), gamma ray (API), neutron (PU) and caliper logs (inches) were used for lithology identification, correlation, hydrocarbon mapping, and estimation of time-to-depth relationship. All of the five exploration wells were drilled on the Snøhvit graben structure, and are plugged and abandoned (NPD, 2015). Besides the wells, core photos in each of the wells in the target zones enhanced further stratigraphic characterization.

Table 3.1 The general information of the five wells in the study area, where MD: measured depth, TVD: true vertical depth (NPD, 2015).

Well name	MD/TVD (m)	Water depth (m)	Oldest Penetrated age	Oldest formation penetrated	Content
7120/5–1	2700/2699	296	Late Triassic	Fruholmen	shows
7120/6–1	2820/2820	314	Late Triassic	Tubeån	Oil/gas
7120/6–2S	3242/3035	321	Late Triassic	Snadd	Oil/gas
7121/4-1	2609/2609	335	Late Triassic	Fruholmen	Oil/gas
7121/5–1	3200/3197	336	Late Triassic	Snadd	Oil/gas

3.3 Seismic interpretation

The main methods used in this work include: (1) mapping of the horizons, faults, and high amplitude anomalies (2) fault and horizon modelling (3) fault displacement analysis and (4) seismic attribute analysis using root mean square (RMS) amplitude, variance and chaos. The overall workflow is summarized in Figure 3.3.

3.3.1 Mapping of horizons, faults and high-amplitude anomalies

The workflow for this section is outlined on Figures 3.3 and 3.4 , respectively.

Mapping of Horizons a) Isochron maps b) Isopach maps	Mapping of faults a) Structural frame work modelling b) Fault modelling	Mapping of HAAs a) Geometry of HAAs b) Seismic attribute analysis (RMS amplitude)
Stratigraphic characterization a) Seismic stratigraphy b) Seismic geomorphology c) Seismic attribute analysis (RMS amplitude)	Fault analysis a) Descriptive graphical analysis b) Throw analysis c) Displacement analysis	Migration pathway detection Combine multi attribute analysis (RMS amplitude, chaos, variance etc.)

Understand subsurface flow drainage mechanisms
• Structural and stratigraphic controls on fluid flow

Figure 3.3 Flowchart showing the overall workflow followed in this thesis together with all the methods used, where HAA: high amplitude anomalies; RMS: Root Mean Square amplitude.
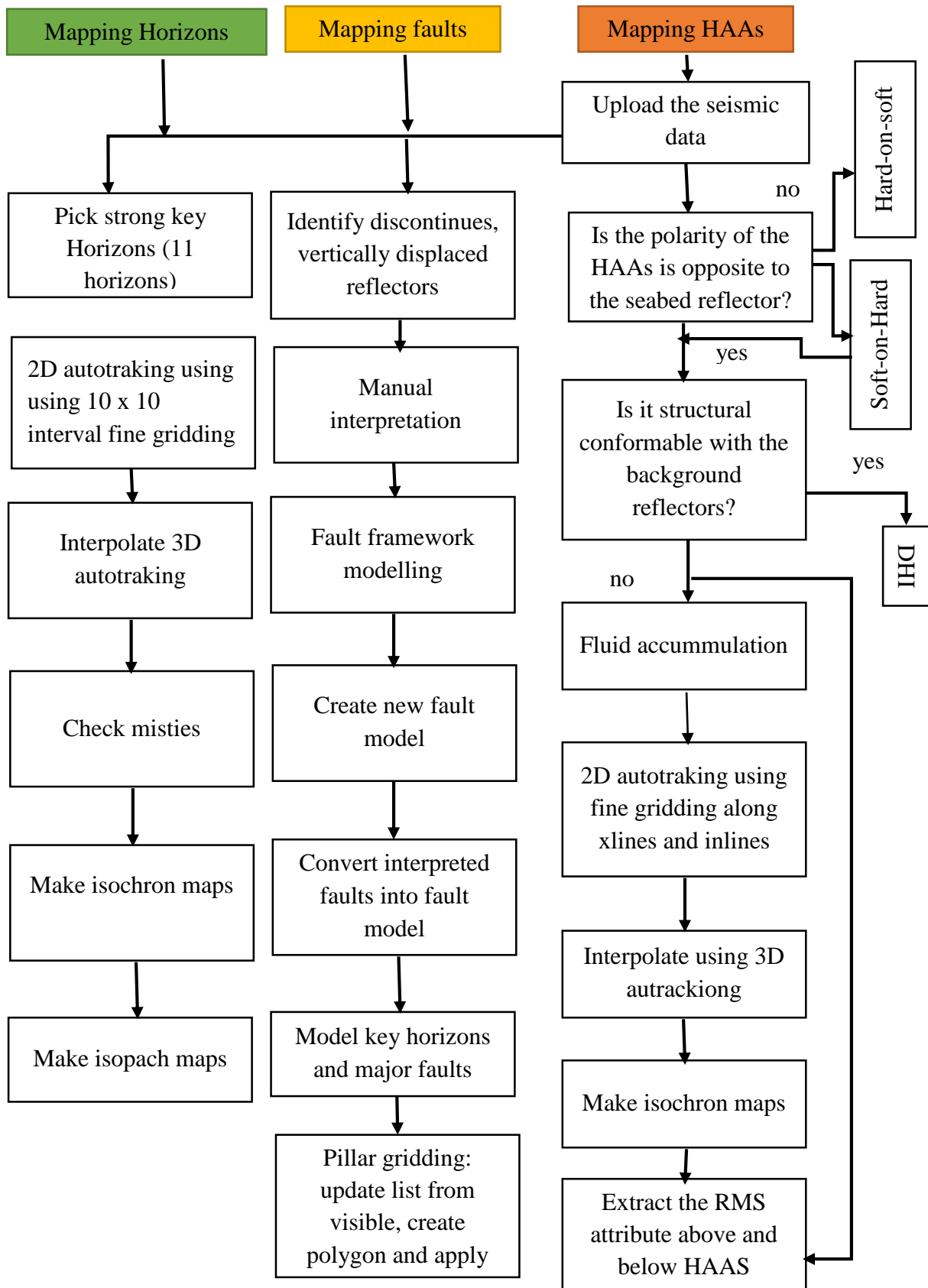
Figure 3.4 Detail workflow for mapping and modelling of faults and horizons, and mapping and RMS amplitude analysis of HAAs used in Petrel. DHI: direct hydrocarbon indicators.

Mapping of horizons

The first task in mapping of the horizons is well-to-seismic tie in which formation tops from the boreholes were linked to their time-equivalent reflectors on the seismic data (Figure 3.5). The horizons in this work were interpreted using the 2D autotracking tool in Petrel®2014 across individual seismic profiles (Figure 3.6). Subsequently, the interpretation was extended into the seed grid at inlines and crossline spacing of 10 (equivalent to 125 m). The complete grids were later converted into surfaces in order to display the horizons as isochron maps (Figure 4.6). In situations where the reflectors are continuous, the 3D autotracking tool was used instead. The misties across horizons were corrected with the aid of the seed grid shown in Figure 3.6. Overall, eleven (11) major horizons were interpreted picked and discussed in Chapter 4. Furthermore, isochore or two-way travel time (TWTT) maps were generated from the isochron maps in order to assess areas characterized by thickness variation and affected by faulting. Ten isochore or TWTT thickness maps were generated from the eleven interpreted isochron maps.
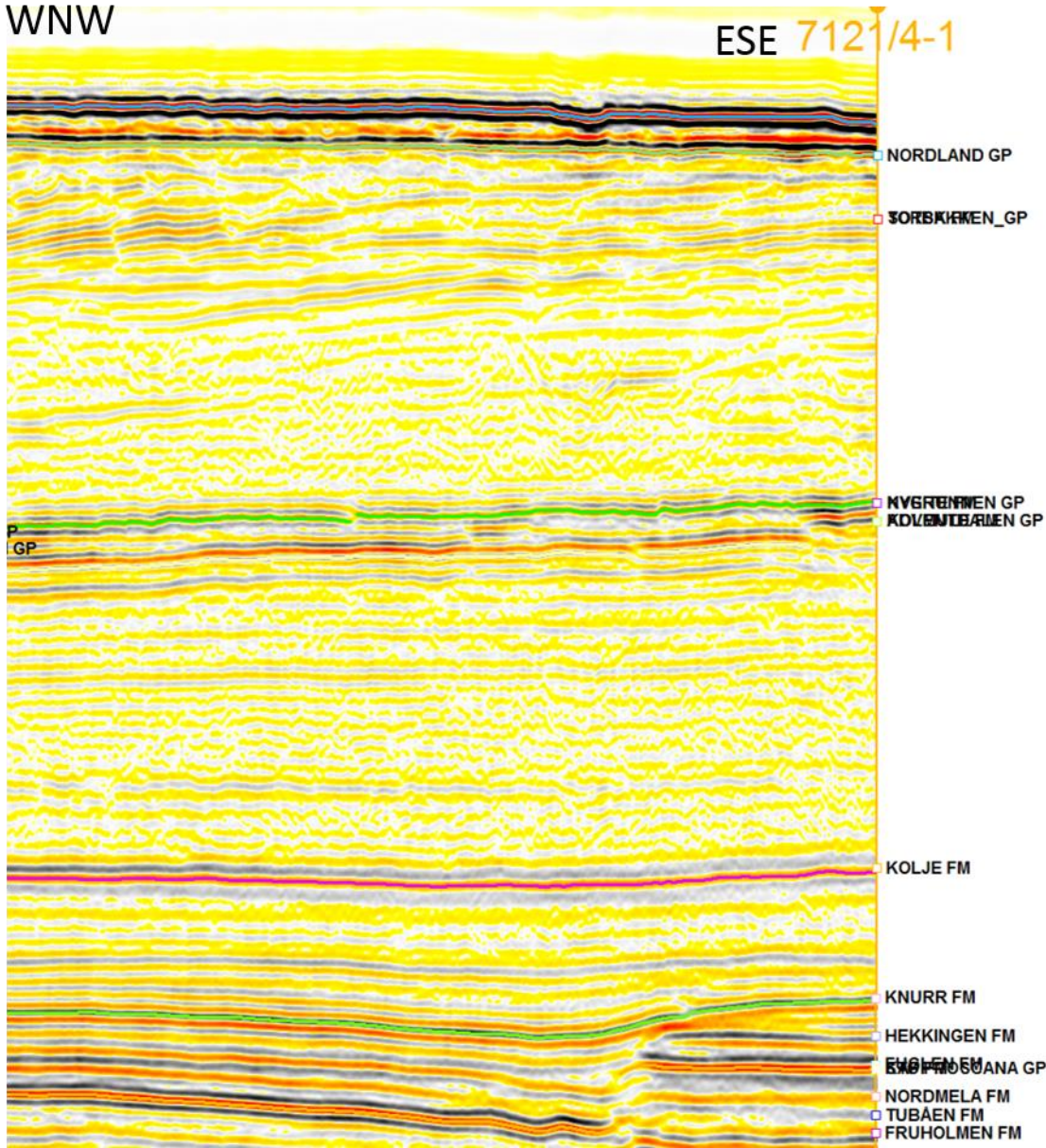
Figure 3.5 Seismic-to-well tie was used for horizons mapping in which formation tops from boreholes were linked to their time-equivalent reflectors on seismic data.
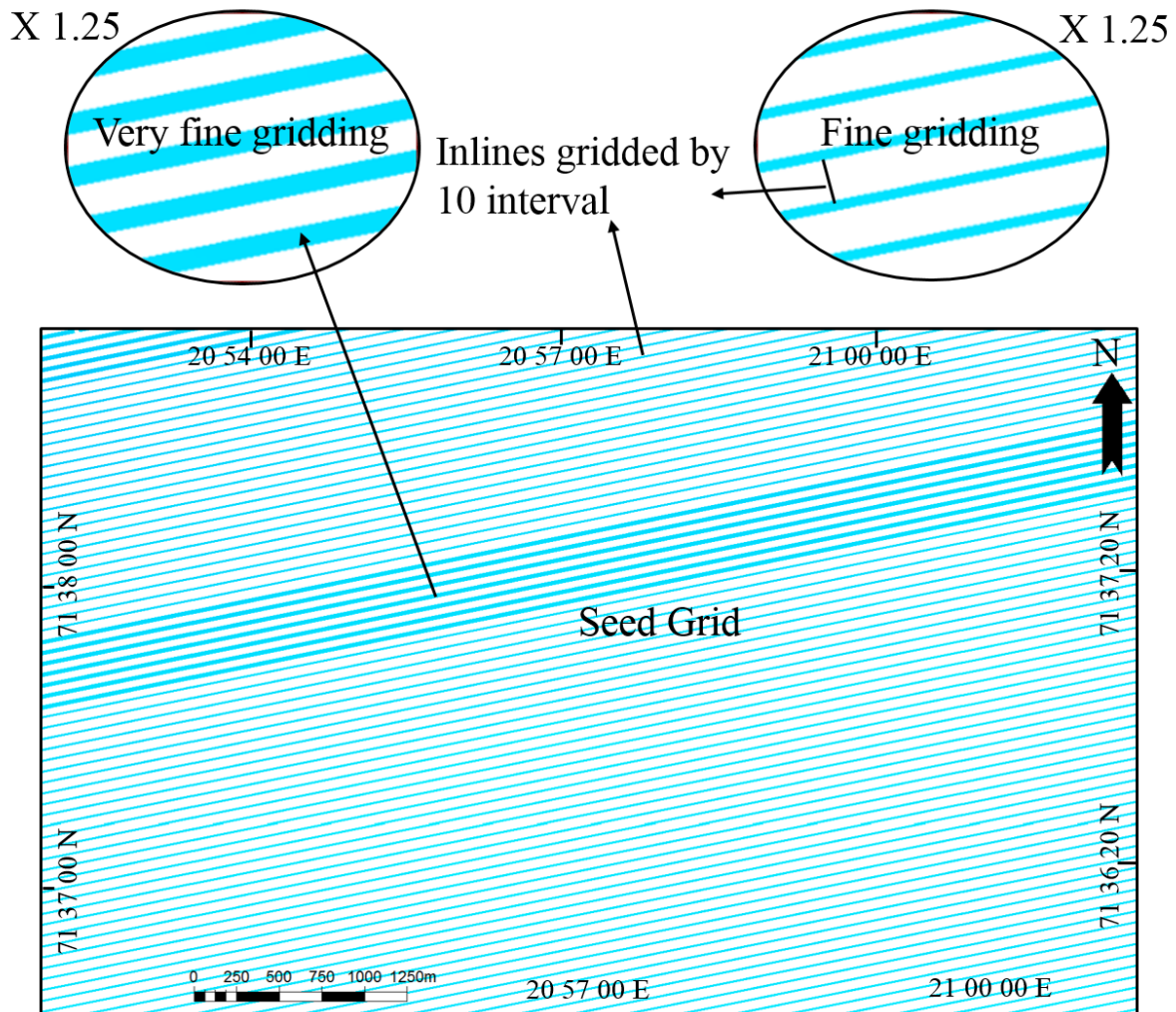
Figure 3.6 Seed gridding used for horizon interpretation . The 2D auto tracked lines were interpolated using 3D auto tracking technique. The seismic interpretation was done at fine gridding of 10 inlines and crosslines (equivalent to 125 m).

Fault interpretation

Faults on the seismic sections can be recognized based on their discontinuous reflectors which indicate their location, and the dip separation can be estimated by correlation of similar reflectors across the faults (Brown, 2004). Vertically displaced discontinuous reflectors and reflection shadows along the fault zone were used to observe and pick faults. The dip separation was observed on vertical seismic section and the horizontal traces on fault surface maps were visualized (cf. Fossen, 2010). The vertical (throw) dip separations were measured at fault cut-off points on the hanging wall and footwall sections (Figure 3.9). Faults in this study were manually interpreted across section profiles at inline and crossline interval of 5 (62.5 m).

Interpretation of seismic high-amplitude anomalies (HAA)

The nature and polarity of the seabed was used to distinguish between high-amplitude anomalies related to lithology from those connected to fluid leakage and accumulations. There is an acoustic impedance contrast when seismic waves move from the sea water to the seabed and into the underlying bedrocks as a result of increase in velocity and density (Sheriff and Geldart, 1995). Anomalies similar in polarity with the seabed are treated as "hard-on-soft" i.e., related to the lithology or diagenetic effects. The anomalies with opposite polarities when compared to the seabed are characterized as "soft-on-hard" which are the result of fluid leakage or accumulations in the subsurface (Alves et al., 2015).

The first step in mapping the anomalies is to examine the phase and polarity of the seabed, then find 'soft-on-hard' reflections in the seismic volume. The second step is to examine whether this anomaly is structurally conformable with the background reflectors (Figure 2.22). This helps to distinguish the soft-on-hard reflectors that are flat spots or hydrocarbon water contacts. Since this is not enough to identify them, amplitude extraction above and below the anomalies was done to further characterize the anomalies as those related to fluid accumulations or direct hydrocarbon indicators (Figure 3.11).

3.3.2 Fault and horizon framework modelling

The fault framework modelling of all the mapped faults was done in the time domain and an average interval velocity of 2 km/s was used to calculate the dip and dip direction of the faults (Figure 3.7). However, these dip values can be also calculated using the strike, horizontal length and vertical depth of the faults. The average dip and dip direction of all faults was estimated from the modelled fault framework. Furthermore, graphical analysis of the faults includes the use of rose diagrams and equal area plots. Fault attitudes such as strike and dip data, were imported into graphical fault analysis tool GEOrient software. Rose diagrams are circular frequency histograms that are used for plotting directional (azimuthal) data such as fault strike (e.g., Figure 4.10). On the other hand, equal area projections are used to plots fault dip and strike (e.g., Figure 4.11). Both plots are used to identify the orientation of the faults that controls the vertically upward/focused fluid flow in the study area. Fault and horizons models are prerequisite for fault analysis especially when using the RDR plugin® in Petrel® 2014 (Figure 3.7 and 3.8).

3.3.3 Fault displacement analysis

In order to understand the history of fault growth, linkage and reactivation, fault displacement data are used (Omosanya and Alves, 2014; Tvedt et al., 2013). Fault displacement data used in this thesis include the plot of displacement- distance (t-x), throw-depth (t-z), expansion and growth indices. Throw of faults was measured as a difference between the hangingwall and footwall depth/time of a given horizon, and was constrained by the differences between the hangingwall and footwall cut-off value on the seismic profiles (Figure 3.9).

Throw-depth (t-z) plots were determined from the throw across faulted horizons, and then plotted against depths to the midpoints between the respective hanging-wall and footwall cut-offs (Baudon and Cartwright, 2008a, 2008b; Reeve et al., 2015). These plots provide insights about potential reactivation of fault by dip linkage (Mansfield and Cartwright, 1996; Omosanya and Alves, 2014; Tvedt et al., 2013), and also distinguishing faults that developed through syn-sedimentary activity from blind or radial propagation of tips (Childs et al., 2003; Omosanya and Alves, 2014).

Time-to-depth relationship from check-shot velocity data nearby four wells (7120/5-1, 7120/6-1, 7121/4-1 and 7121/5-1) was determined to compare throw values in time (ms TWTT) and depth (m). The best fitting polynomial function was determined from time-depth domain relationships (Figure 3.10a). The correlation coefficient is nearly one (0.9996) showing that the depth in time and depth domain are strongly correlated and the average interval velocity used for this conversion (2 km/s) was correct. So, plotting the throw profiles in time and in depth domain is the same (Figure 3.10b and c).

Expansion Index (EI) has been used to define periods of most significant fault growth form normal faults (Beach, 1984; Bischke, 1994; Gibbs, 1983; Mansfield and Cartwright, 1996; Pochat et al., 2009; Thorsen, 1963) but does not contain any information about absolute slip rate (Cartwright et al., 1998). Expansion indices and t-z plots can be used to constrain timing of fault activity. It is the ratio of footwall to hangingwall stratal thickness (Figure 4.17 and Eq. 3).

$$EI = \frac{\text{Thickness of hangingwall strata}}{\text{Thickness of footwall starata}} \dotfill \text{Eq.3}$$

Where, EI > 1 represents thickening in the hangingwall

The Growth Index (GI) is the ratio of the difference in thicknesses between the hangingwall and the footwall strata divided by the thickness of hangingwall strata (Figure 4.18 and Eq. 4). Growth index records can indicate the timing and depict the growth history of faults (Henriksen et al., 2011; Hongxing and Anderson, 2007; Pochat et al., 2009). It is a measure of relative throw rate to the sedimentation rate in the footwall.

$$GI = \frac{\text{Thickness of hangingwall strata} - \text{Thickness of footwall strata}}{\text{Thickness of hangingwall strata}} \dotfill \text{Eq.4}$$

Throw and displacement profile analyses provide clear picture of fault propagations, reactivations and linkages which thereby are inked to timing of fluid leakage in the study area. These indirect inferences were used in the role of the faults on fluid and hydrocarbon plumbing in the study area.
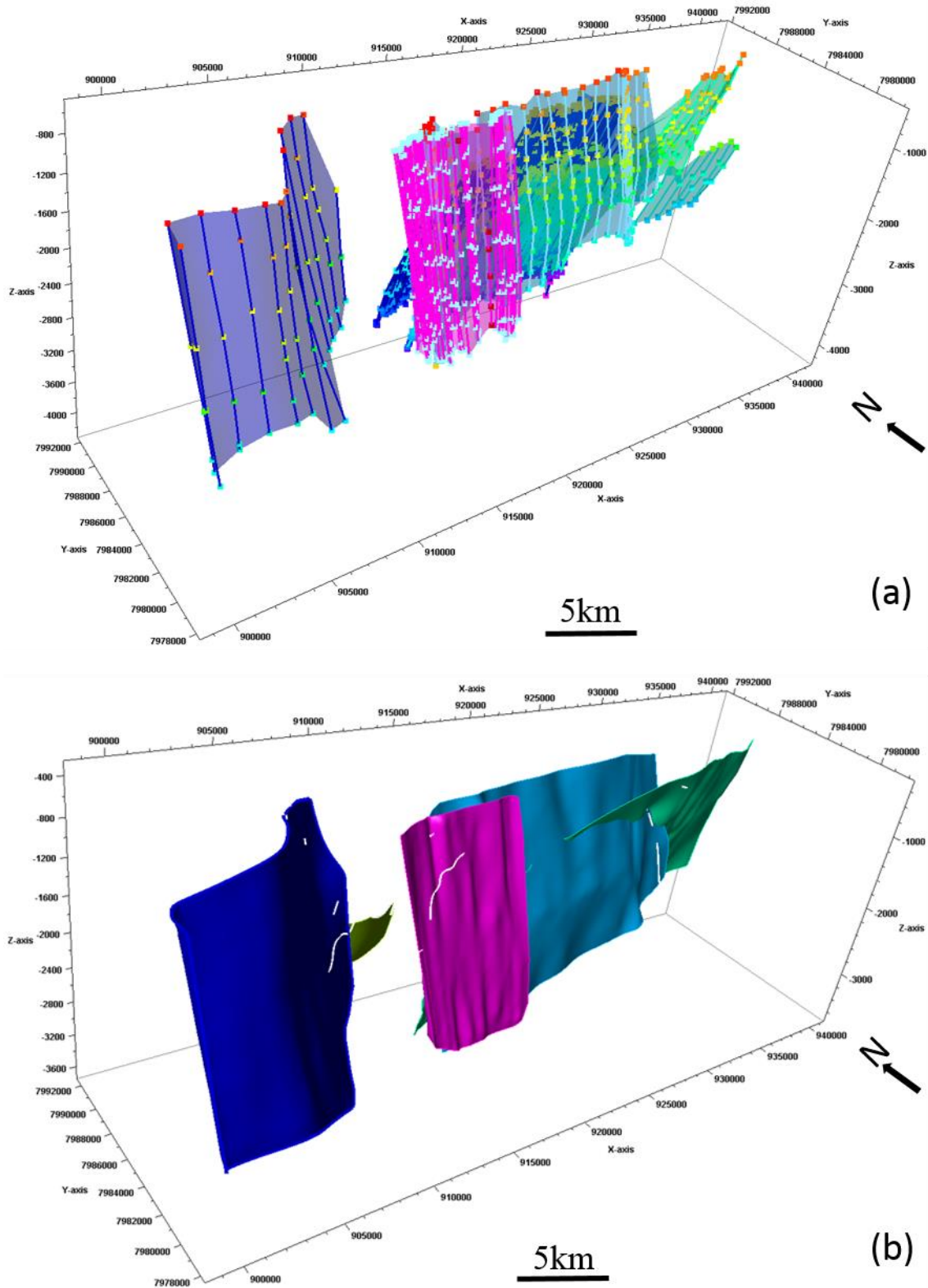
Figure 3.7 Fault modelling (a) Example of un-modeled major faults and (b) modelled equivalent of the major faults. Fault modelling is used to remove and reduce uncertainty associated with fault mapping.
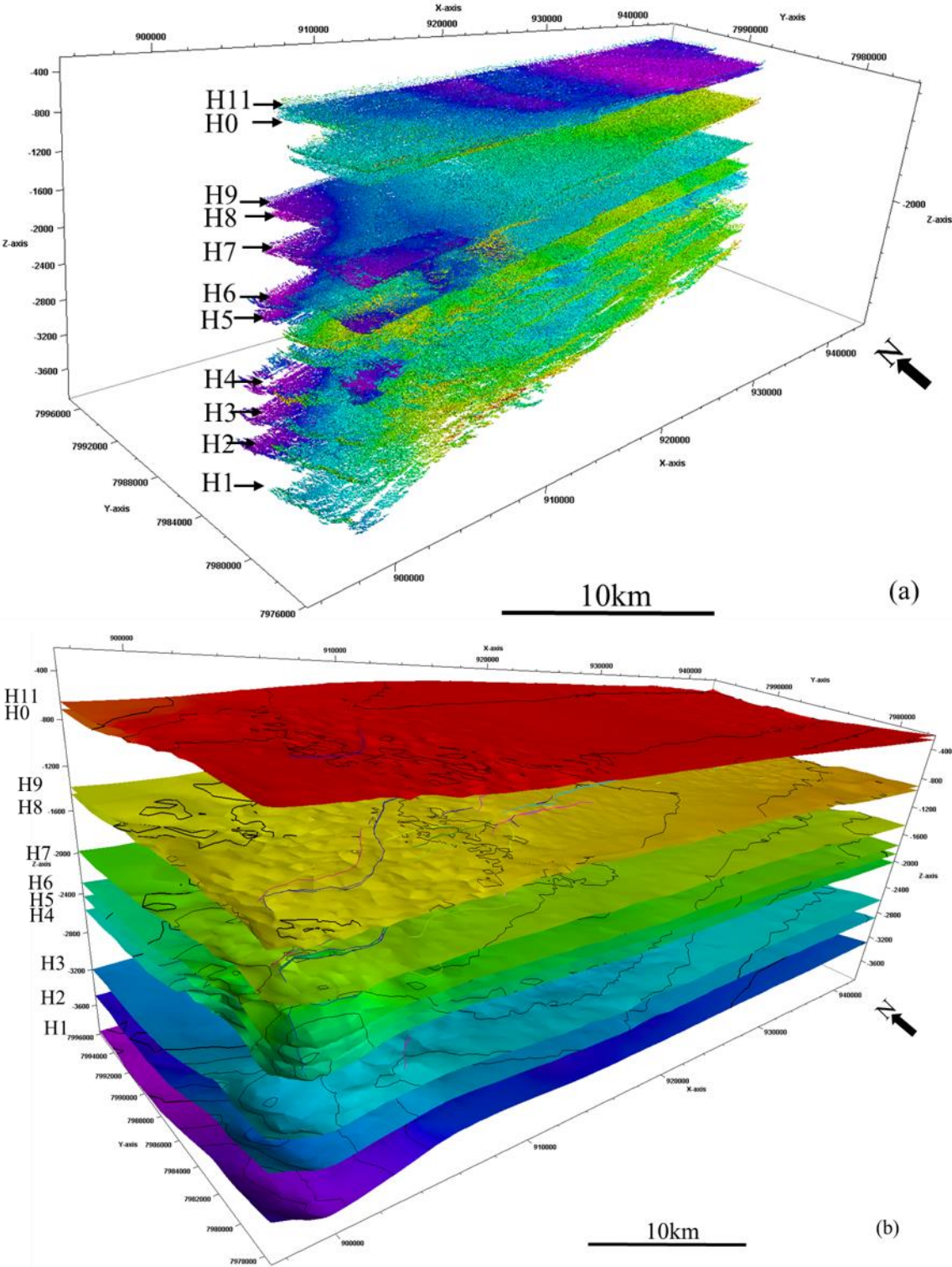
Figure 3.8 Horizon modelling (a) Examples of interpreted and un-modeled stratigraphic surfaces (b) Modeled time isochron maps for horizons H1 to H11.
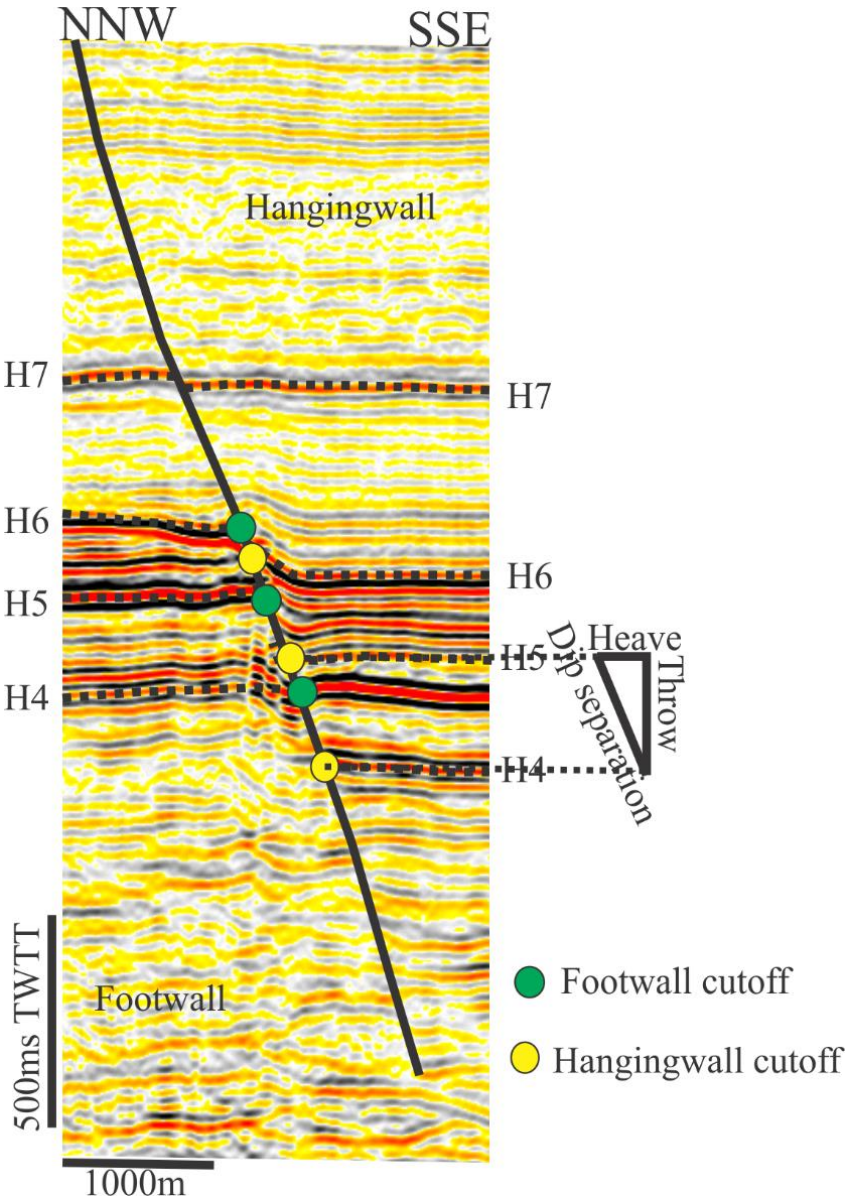
Figure 3.9 Throw estimation from the hanging-wall and footwall cut-offs. The dip displacement is the square root of the sum of the square of heave and throw.

$$y = 0.0004x2 + 0.3542x + 184.53$$
$$R^2 = 0.9992$$
$$R = 0.9995$$
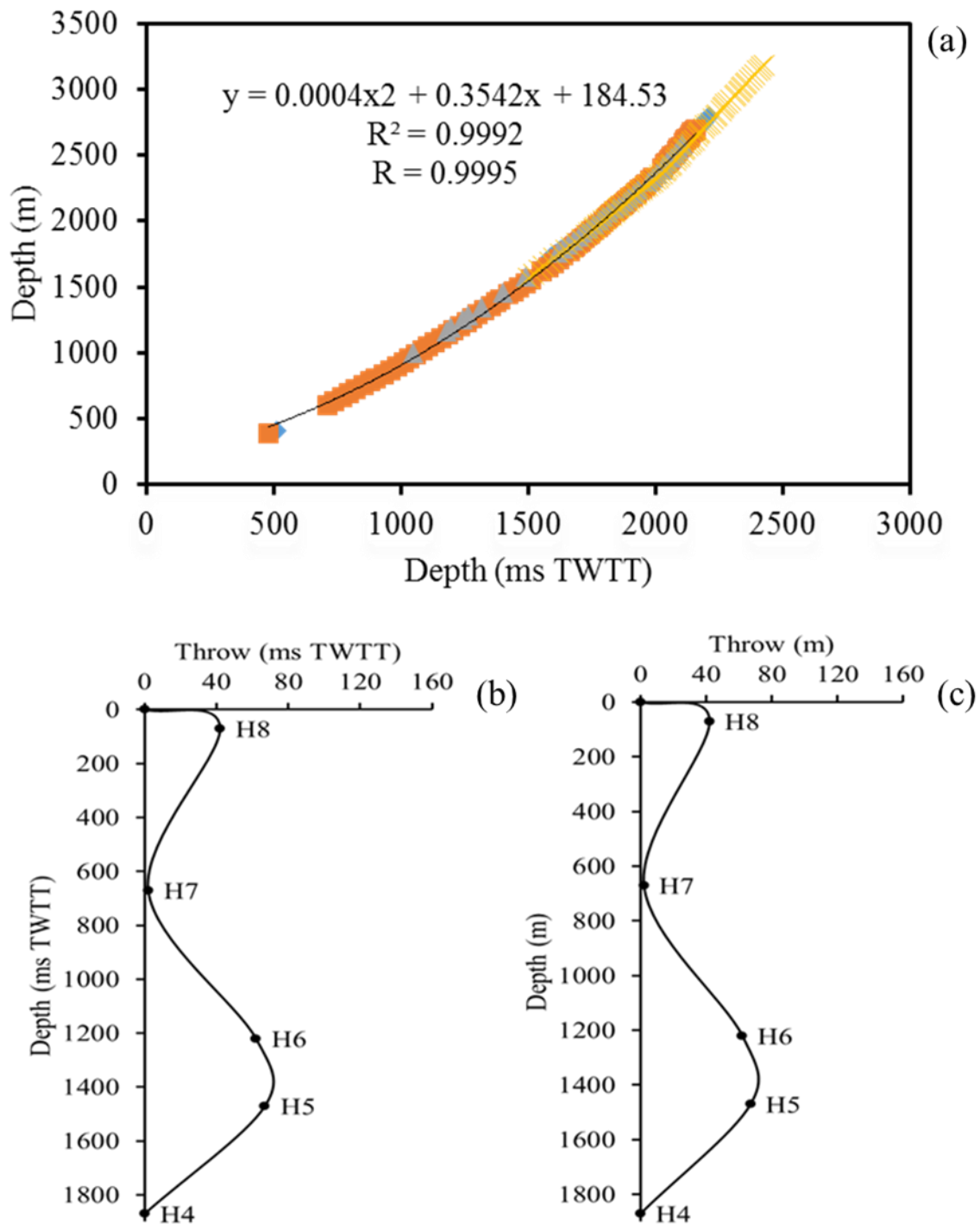
Figure 3.10 Time-to-depth relationship a) Plots of throw profile in time and depth domains using checkshot data from nearby wells (7120/5-1, 7120/6-1, 7121/4-1 and 7121/5-1). The correlation coefficient of correlation (R) is ~1showing that there is perfect linear relationship between throw in time and depth. (b) Throw-time (ms) plot and (c) Throw-depth (m) are similar in geometry and shape profiles.

3.3.4 Seismic attribute analysis

Seismic attributes were extracted from the seismic volume to analyze the high-amplitude anomalies and assess their relationship with stratigraphy or geomorphic features. The seismic attribute used include RMS amplitude, chaos, variance and the geobody extraction.

Root Mean Square (RMS) amplitude was computed between the horizons and used to detect the occurrence of high-amplitude anomalies (HAA). RMS amplitude is calculated as the square root of the sum of the squared amplitudes divided by the number of samples (Brown, 2004). The RMS amplitudes combined the effect of positive and negative amplitude that possibly due to the presence of hydrocarbon or fluid. Hence, RMS amplitude seismic attributes are sensitive to sandstone-bearing depositional systems or fluid in a siliciclastic environment (e.g. Figure 3.11).

Chaos attribute map the chaotic signal pattern contained within a seismic data and are a measure of the "lack of organization" in the dip and azimuth estimation method. Chaos in the signal can be affected by gas migration paths, salt body intrusions, and for seismic classification of chaotic texture (e.g. Figure 4.34). Subsequently, variance seismic attribute measures dissimilarity of seismic traces (e.g. Figure 4.33). Variance maps convert a volume of continuity into a volume of discontinuity, highlighting structural and stratigraphic boundaries (Brown, 2004).

The combined attributes are used to show the migration pathways, highlight gas chimneys and the static fluid accumulations. The results from these attribute analysis are input for the geobody extraction. The opacity of the geobodies is filtered using the color of the high-amplitude anomalies at frequency threshold of 20%.
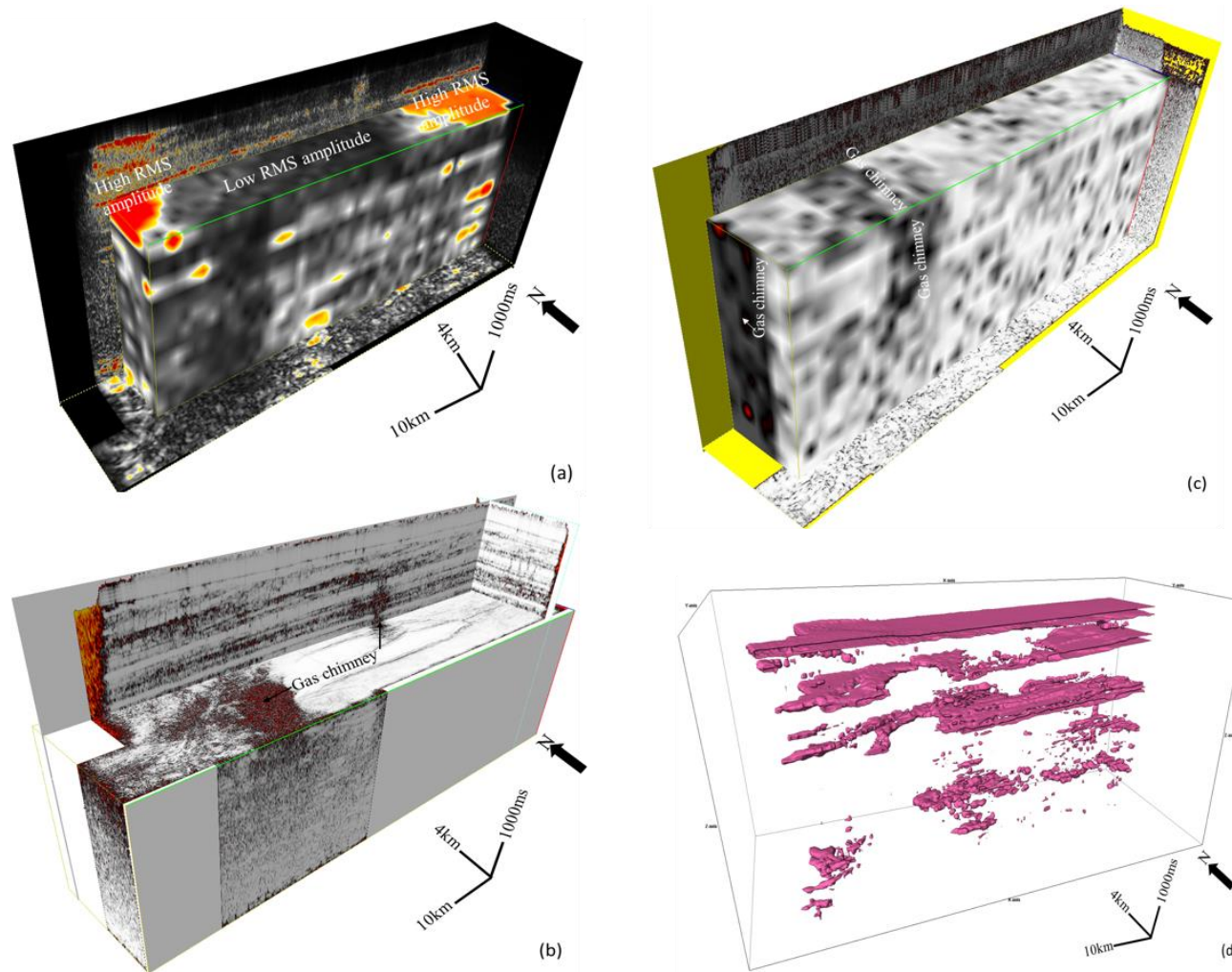
Figure 3.11 Seismic attribute cubes (a) RMS cube showing the low amplitude (black) and high amplitude (red) (b) and (c) variance and chaos cube showing gas chimneys and (d) the box probe of RMS amplitude highlighting the geometry of the high-amplitude anomalies.

Chapter 4 Interpreted horizons, faults and High-amplitude anomalies

4.1 Seismic stratigraphy of the study area

Eleven (11) horizons were interpreted in the study area from the seabed reflector (H11) to the top Carboniferous (H1). The seabed is characterized by numerous E-W and N-S orientated seabed furrows or plough marks (Figure 4.1). The linear E-W furrows are dominantly observed in the eastern and western parts of the seabed while the non-linear N-S furrows are observed at the central parts of the seabed. The upper tips of most of the faults at the Torsk Formation were interpreted beneath the large depressions on the seabed reflector. These are pockmark features, which vary in size from mega-pockmarks (> 1km wide) to giant pockmarks (> 100 m wide) and large pockmarks (< 100 m wide) (Figure 4.1).
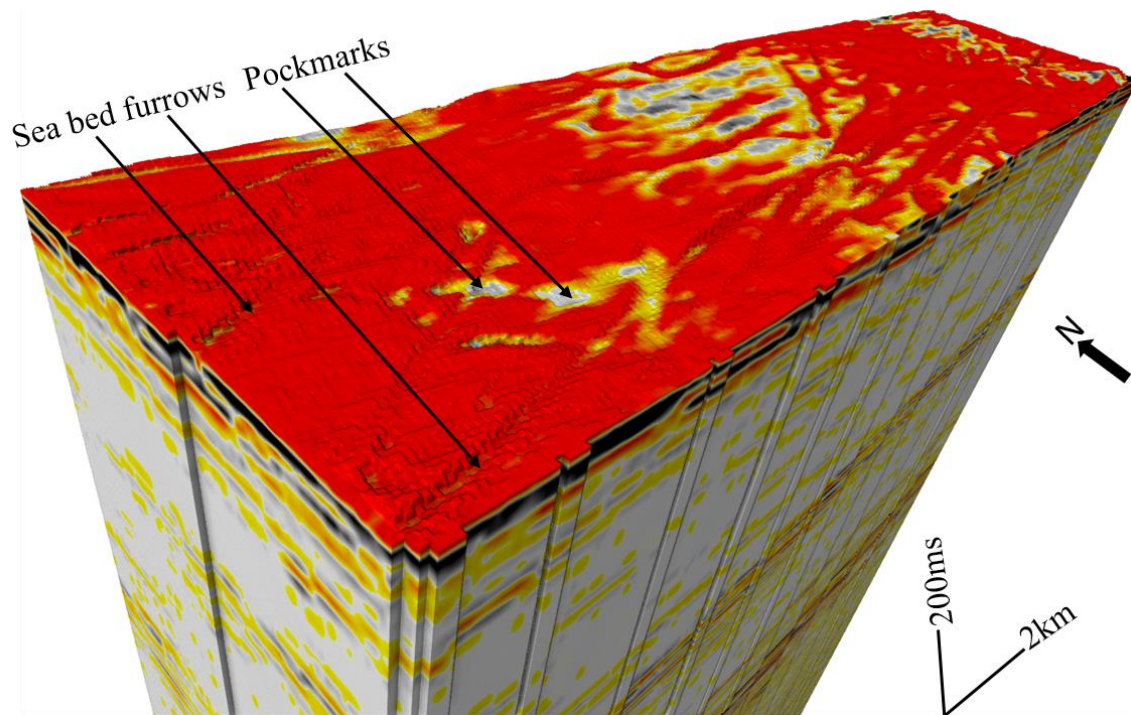
Figure 4.1 Interpreted seabed furrows and pockmarks. The furrows are generally oriented E-W directions while the pockmarks are oriented in both the E-W and N-S directions.

The interpreted horizons were used to divide the stratigraphy of the study area into ten units. These units reflect the influence of faulting and presence of high-amplitude anomalies

suspected to be fluid leaked from the reservoir rock. The characteristic of each of the units is discussed as follows:-

Unit 1

The top of Unit 1 (U1) is marked by H1 at c.3500 ms TWTT (3844 m). This unit is the deepest unit in the study area and is Carboniferous in age (Gabrielsen et al., 1990). It is characterized by strong, continuous and high amplitude reflectors. Unit 1 is composed of channel deposits and carbonates (Ohm et al., 2008).

Units 2 to 8

Unit 2 (U2) and Unit 3 (U3) consist of Permian rocks and are relatively flat in the NNW part of the field and are also affected by acoustic masking on the top central part of U3. The bottom part of the U2 is slightly thickening towards the SSE direction with average thickness by 100 m. On the contrary, the top part of U2 is thickening towards NNW direction (Figure 4.3). Unit 4 (U4) is thick along the graben structure and thin on the horst. This unit is composed of the Triassic Fruholmen, Snadd and Kobbe Formations (Ohm et al., 2008).

Furthermore, Unit 5 (U5) corresponds to the reservoir zone and it is marked by sediments between H4 and H5. Unit 5 has uniform in thickness throughout the section. This unit is further divided into sub-unit 5a (U5a) which consists of Tubåen and Nordmela Formations, and sub-unit 5b (U5b) comprises of Stø, Hekkingen and Knurr Formations from bottom to top. U5a is relatively uniform in thickness throughout the field and approximately 100-200 m (100-200 ms TWTW) thick (Figure 4.9). The thickness of U5b varies in the western and eastern parts of the field. In the western part, U5b has thickness of below 50 (50 ms TWTT) and it is up to 200 m (200 ms TWTT) in the eastern part (Figure 4.10). The thickness maps also show thickness differences on both sides of the footwall and hangingwall of the major faults.

Unit 6 (U6) comprises the Kolje Formation and follows the topography of the Unit 5. It can be subdivided into lower and upper sub-units, U6a and U6b which are separeted by a strong continuous reflector (Figure 4.2). U6a is very thin on the graben structure and thick in the horst part which indicates that it is an infilling of the accommodation created by Jurassic faults. On the other hand, the U6b reflector is flat implying that accommodation space was not further created during its deposition.

Unit 7 (U7) comprises the Kolmule Formation and is relatively uniform in thickness. Unit 8 (U8) is composed of the Kveite and Kviting Formations and has very strong reflectors with intense discontinuities. It is highly faulted and characterized by high amplitude anomalies.

Units 9 and 10

Unit 9 (U9) comprise the Torsk Formation and is further subdivided into lower and upper parts (U9a and U9b). The lower part (U9a) is between horizon H9 and an arbitrary horizon (Ha) that marks the upper tips of the major faults, gas chimneys and shallowest HAA anomalies.   The sediments in this unit are downlapping towards the bottom reflector (H3) and thinning towards the SSE. Lenticular features (on crossline 1497 and inline 2448) are observed at the top prograding unit (U9b). The upper part (U9b) unit is toplapping towards H10 and underlain by a NNW to SSE retrograding lower part (Figure 4.2).

Unit 10 (U10) corresponds to the Nordland Group and it is the topmost unit deposited in the area. At its lower part, Unit 10 is marked by the regional angular unconformity called the Upper Regional Unconformity (URU). This unconformity marks the commencement of Pliocene to Pleistocene glaciations.
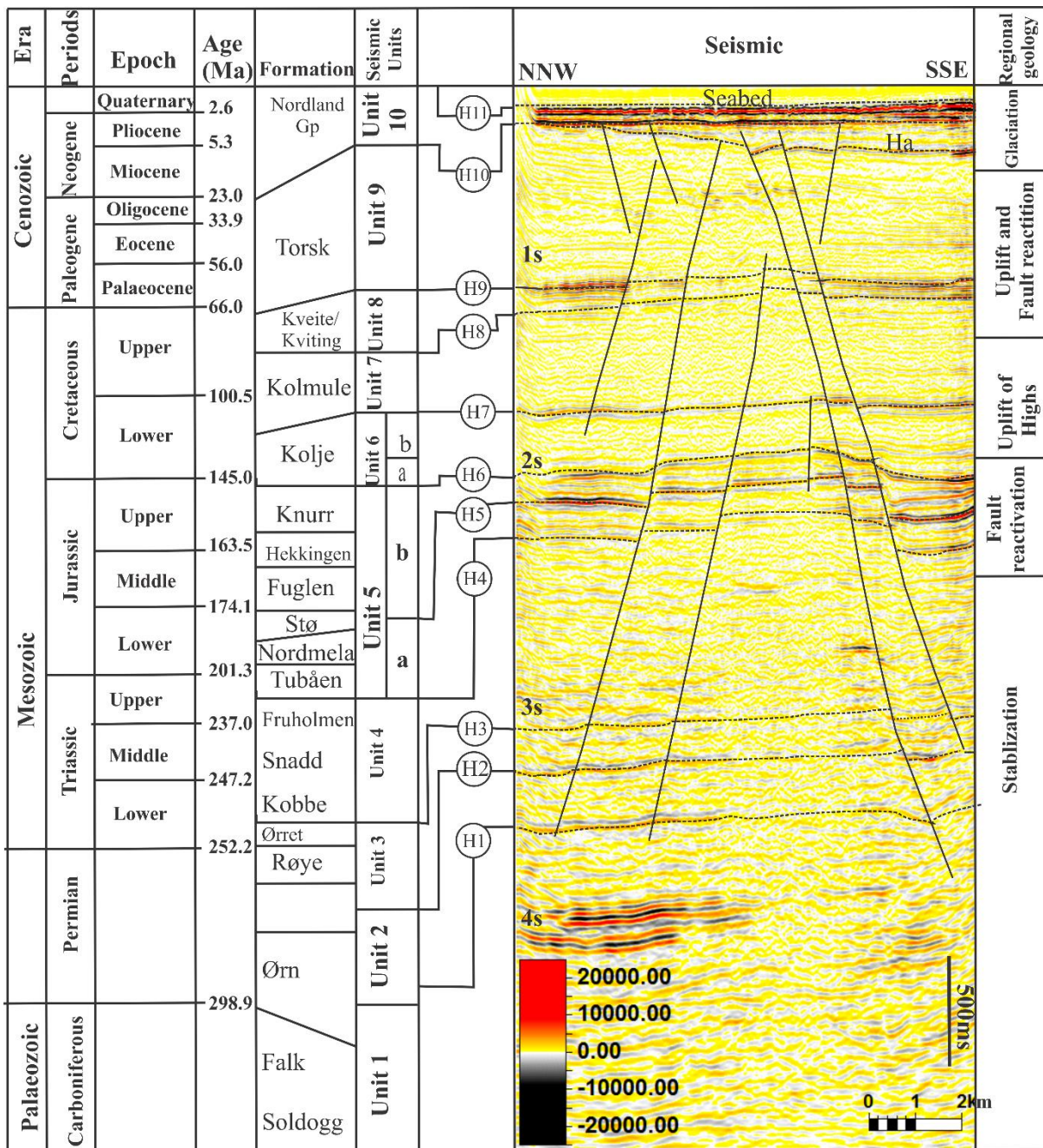
Figure 4.2: Seismic stratigraphy of the Snøhvit Field showing the major units with their interpreted formation tops and the summarised tectonic history of the study area (modified from Ostanin et al., 2013). *See the location on Figure 4.6a. Ha is an arbitrary horizon that divides Unit 9 into U-9a and U-9b.*
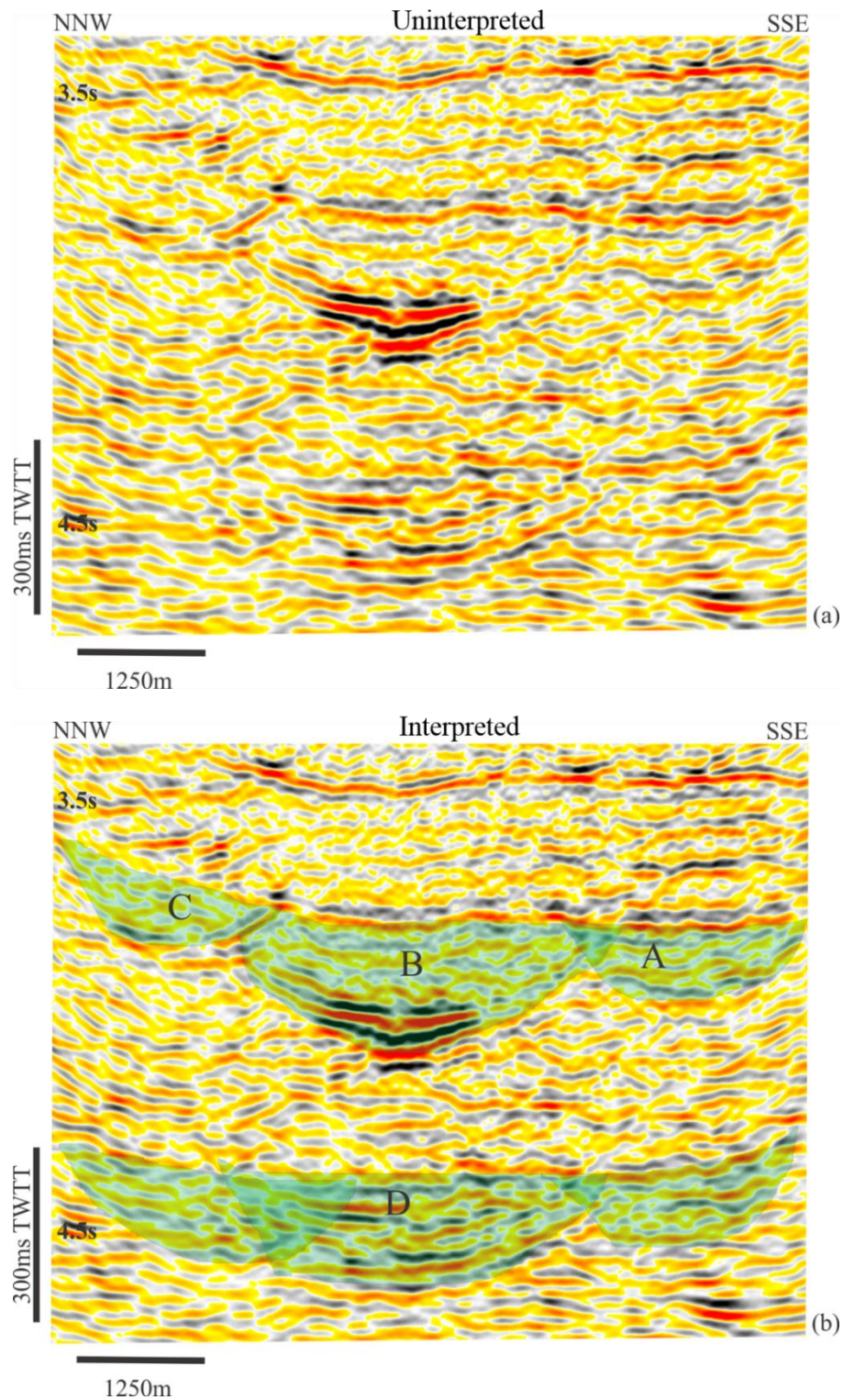
Figure 4.3 Channel features on the crosslines (a) Uninterpreted and (b) interpreted seismic sections showing channels interpreted within Unit 1. The channel sets change in character from NNW direction to SSE, shown as A, B and C. *See the location of the line on Figure* 4.6*a.*
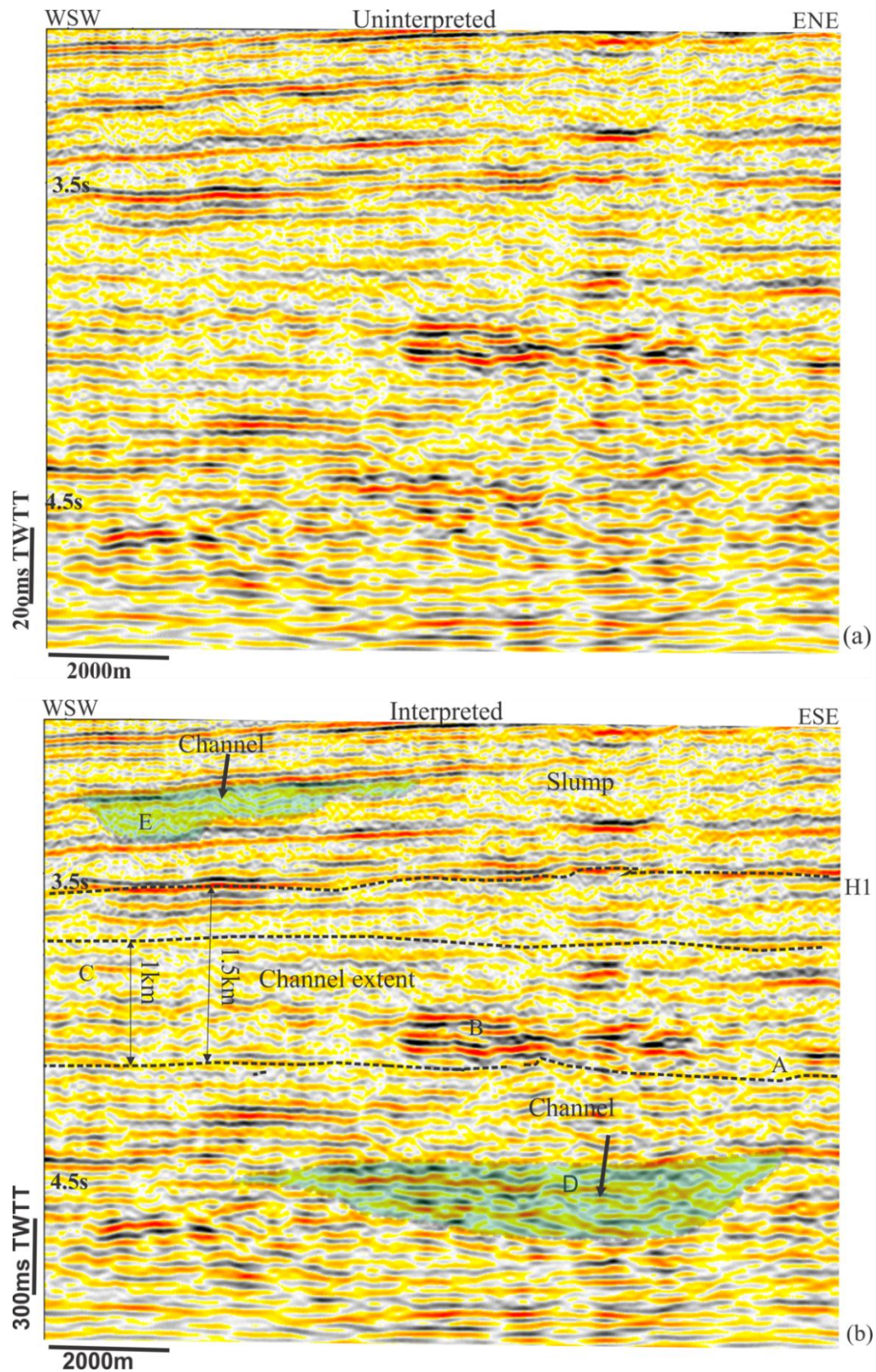
Figure 4.4 (a) Uninterpreted and (b) interpreted seismic sections showing the interpreted channel and slump deposits . The concave upward feature can be traced down to the WSW direction. *See the location of the line on Figure 4.6b.*
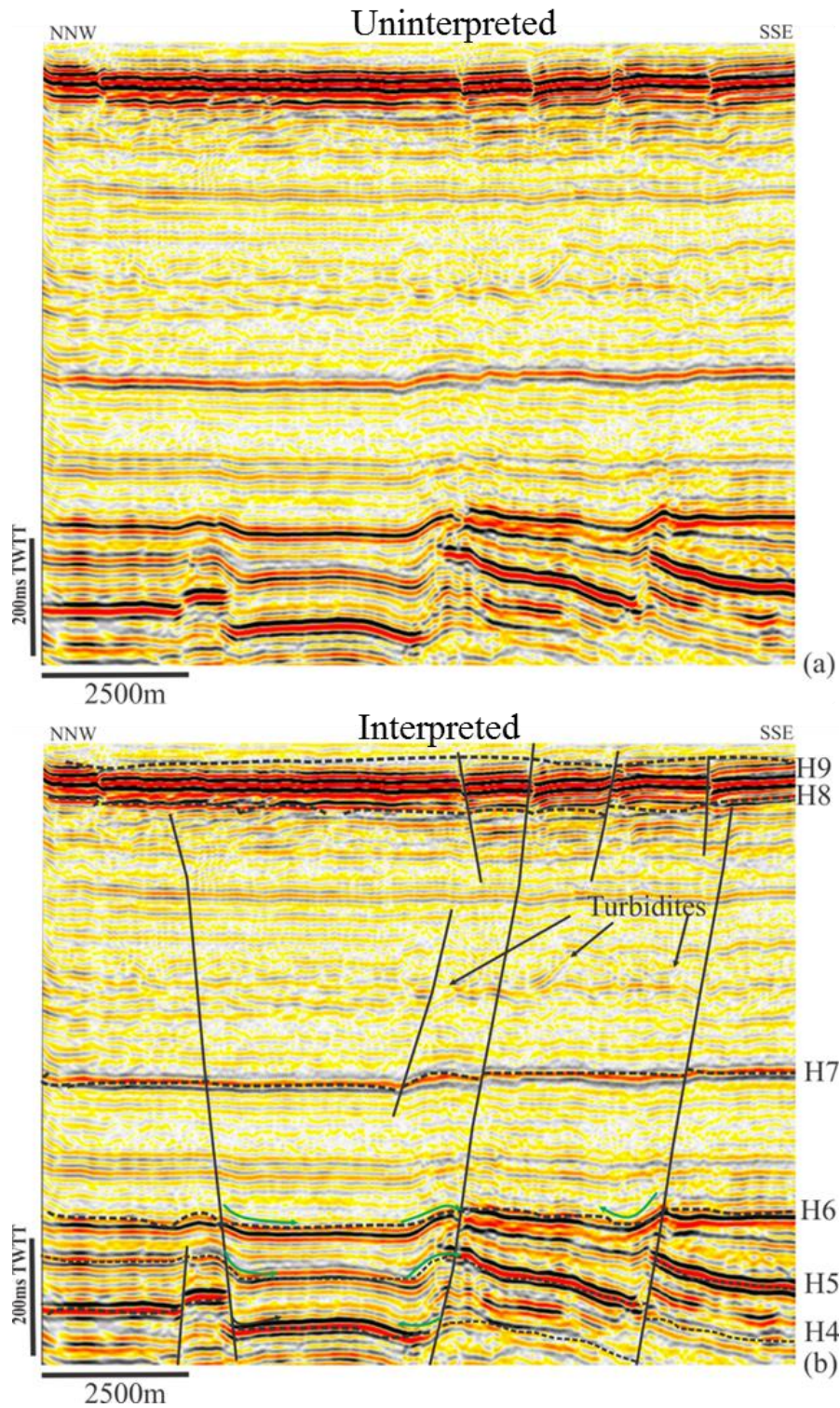
Figure 4.5 (a) Uninterpreted and (b) interpreted seismic sections showing thickening along WSW dipping fault and drag of sediments along the flank of the horst structure in Unit 5 (Reservoir zone). Turbidites were also recognized in Unit 7. See the location of this line on Figure 4.6c.
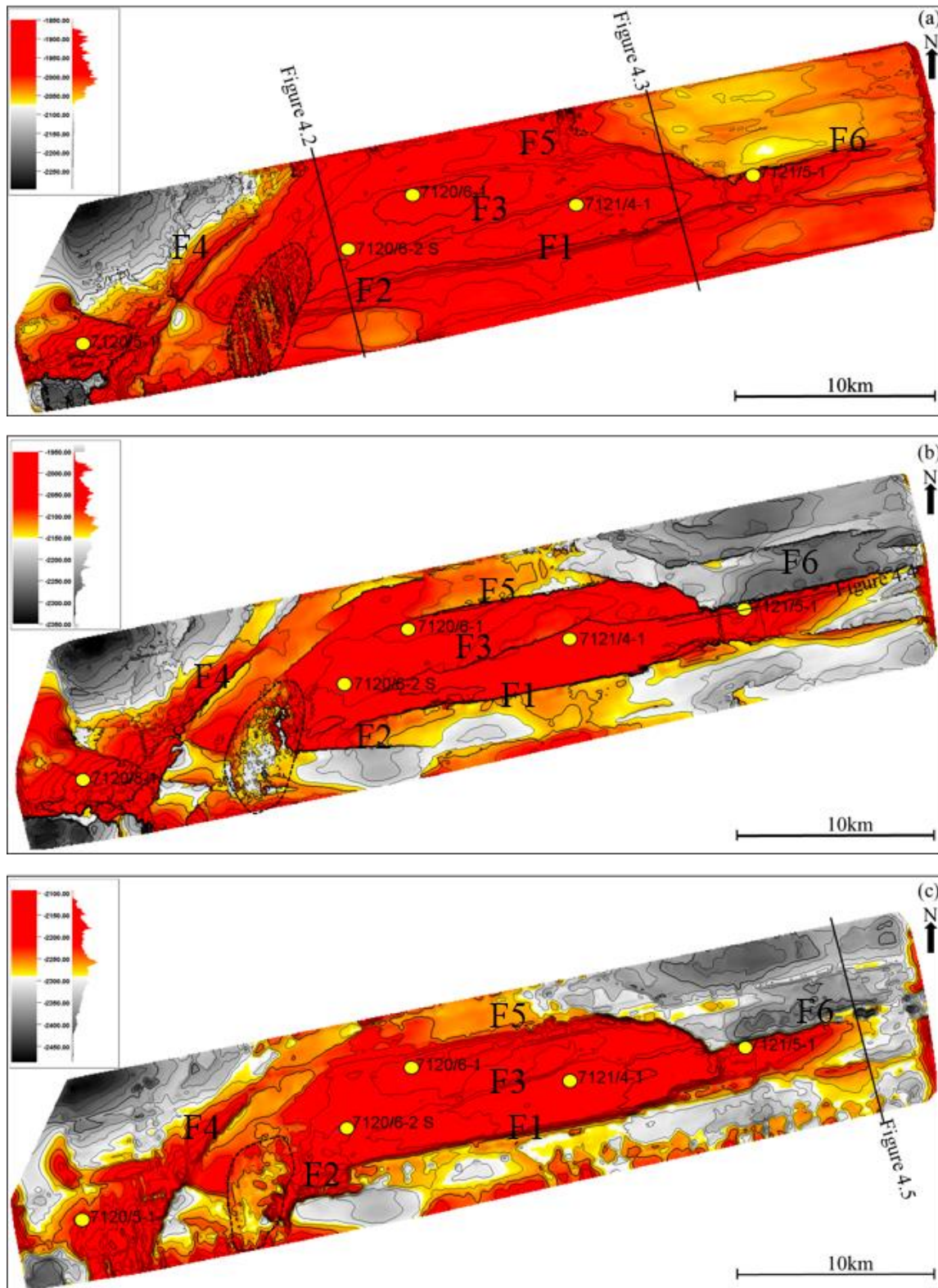
Figure 4.6 Structural time (*isochron*) maps of the key horizons (a) H6 (b) H5 and (c) H4. The major faults offsetting these horizons are characterized by steep gradients. *The black dotted-circle indicates areas of poor data quality linked to the presence of gas chimney, yellow dots indicated the location of the boreholes.*
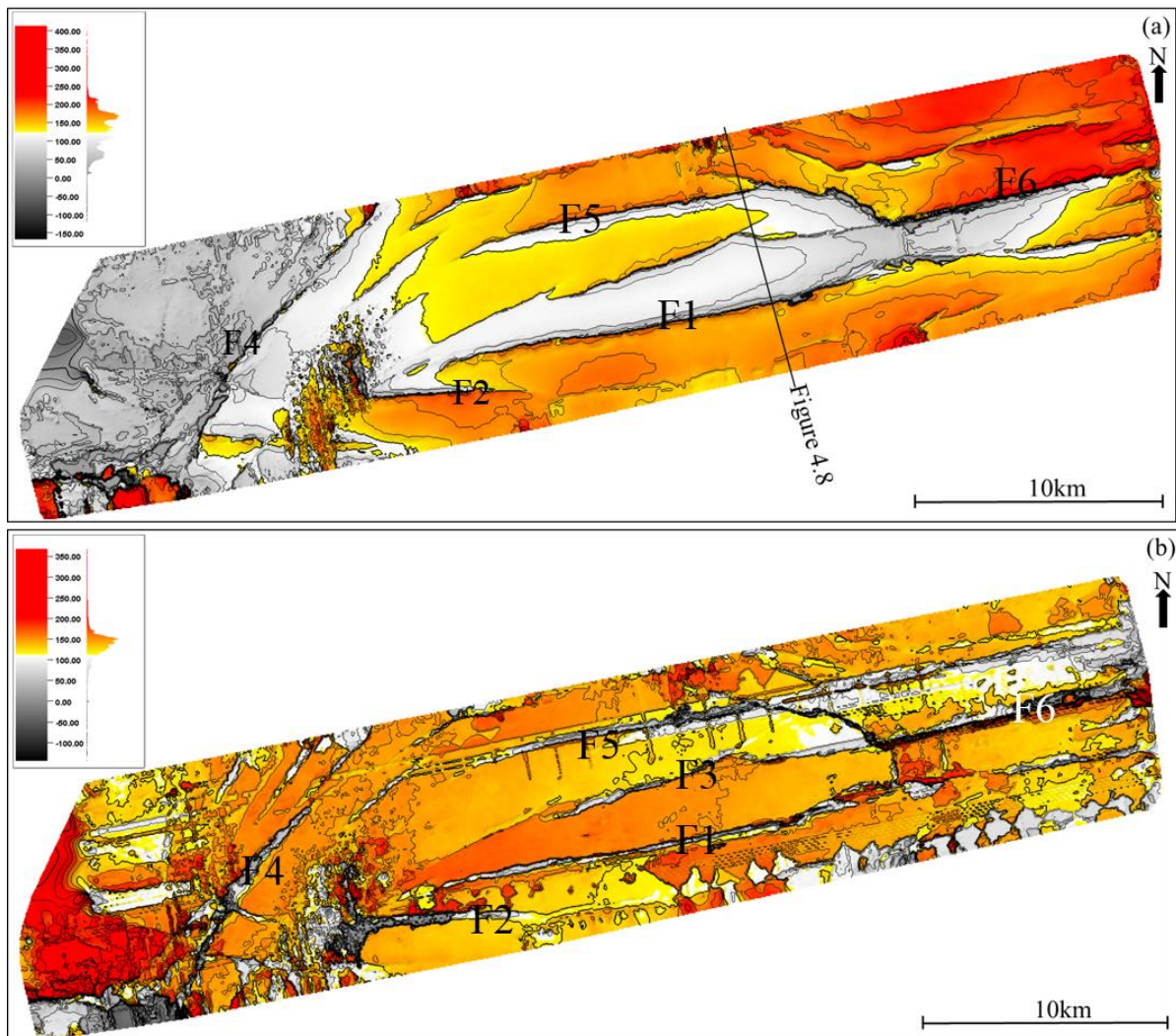
Figure 4.7 Two-Way Travel Time thickness (*isochore*) maps between horizons H4 and H5 (Unit 5a) and horizons H5 and H6 (Unit 5b) showing thickening and thinning to the west, respectively.

4.2 Fault analysis

4.2.1 Interpreted faults

Sixty-two faults (62) faults were interpreted and used for fault characterization and categorized based on size into three major categories; (1) Type A or major faults- are faults offsetting the reservoir zone and which are extended down to Triassic, Permian and Carboniferous formations and include the major deep-seated faults (F1, F2, F3, F4, F5, F5 and F6), (2) Type B or intermediate faults which were identified throughout the seismic volume and are more dominant within the Palaeocene to Pliocene units, and (3) Type C or minor faults which are more dominant within the late Cretaceous (within Kveite/Kviting Formations) and Eocene (Figures 5.1, 5.2 and 5.3) intervals. The major faults are extensive laterally (> 10 km) and are vertically continuous down to deeper depths of 3000 m and more (Figure 4.9). The intermediate faults are found in both shallow and deeper depths, but more dominant at shallower depths (Figure 4.10). The minor faults occur dominantly within Unit 8 in the Kveite/Kviting Formations (Figure 4.11).

Six representative major faults were selected for displacement analysis (F1 to F6) and to examine the role of faulting in fluid leakage in the area (Figure 4.7). Fault 1 (F1) is located in the southern part of the study area (Figure 4.3). This fault offsets Unit 4 to Unit 9 (Figure 4.7b). Fault 2 (F2) is located at the southern end of the field (Figure 4.3). Fault 3 (F3) is the longest fault (Figure 4.15) and is the most deep-seated fault in the study area and it is located in the central part of the field where it divides the field into northern and southern segments of the graben structure. Fault 4 (F4) is located in the western part of the field (Figure 4.9).

The general strike direction of the faults is parallel to the inlines and perpendicular to the crosslines. The faults are striking E-W, NE-SW and ENE-WSW with dips in the SE and NW directions (Figures 4.11 and 4.12). The NE-SW striking faults are the major faults that dominantly tip out upward to shallower depths (600 ms TWTT or 600 m) and tip out downward in the carboniferous Formations (H1). Some of the shallower faults are oriented differently and have a N-S trend. The major faults separate the field into different segments of graben structures dipping towards the NW and SE (Figure 4.10). The ENE-WSW striking faults are the dominant in the western highly faulted part of the field. These faults change their strike to the south-western and north-western ends of the field. The biggest acoustic masking is observed to east of this part, which extend vertically from the H9 to H7. Furthermore, the

western part of the field is dominated by NNE-SSW striking faults. Most of the faults appear as linear (2D) and planar geometry (3D) and some of them are curved in the western part of the field (Figure 4.10).
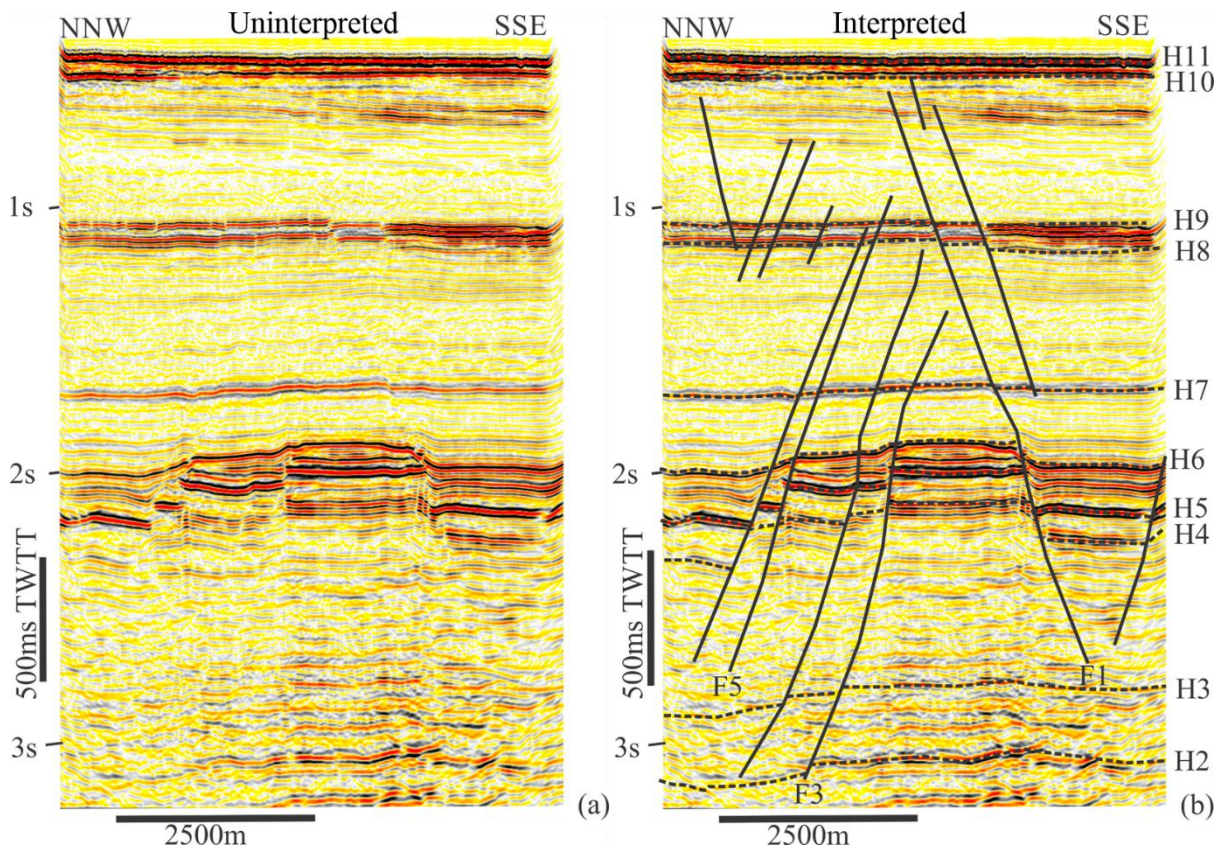

Figure 4.8 (a) Uninterpreted and (b) interpreted seismic profile showing the three major faults in the study area (F1, F3 and F5). *See the location on Figure 4.7a*
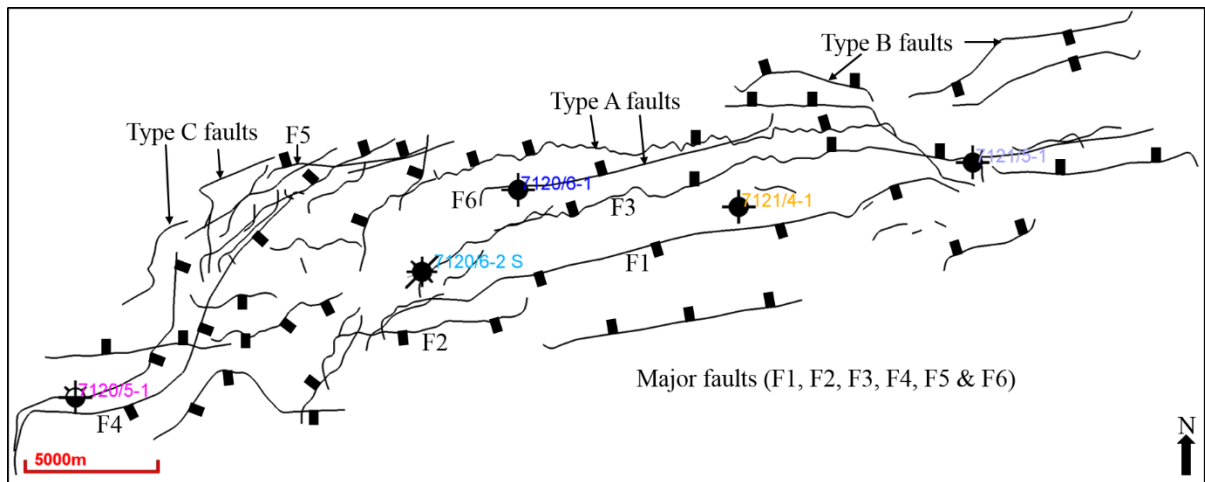
Figure 4.9 2D planar view of modelled faults showing the Type A, Type B, and Type C faults in the study area. The major faults and intermediate faults are ENE-WSE oriented except F4. Most of the minor faults are oriented E-W. *The location of the five wells used in this study are also shown, i.e., 7120/5-1, 7120/6-2 S, 7120/6-1, 7121/4-17121/5-1.*
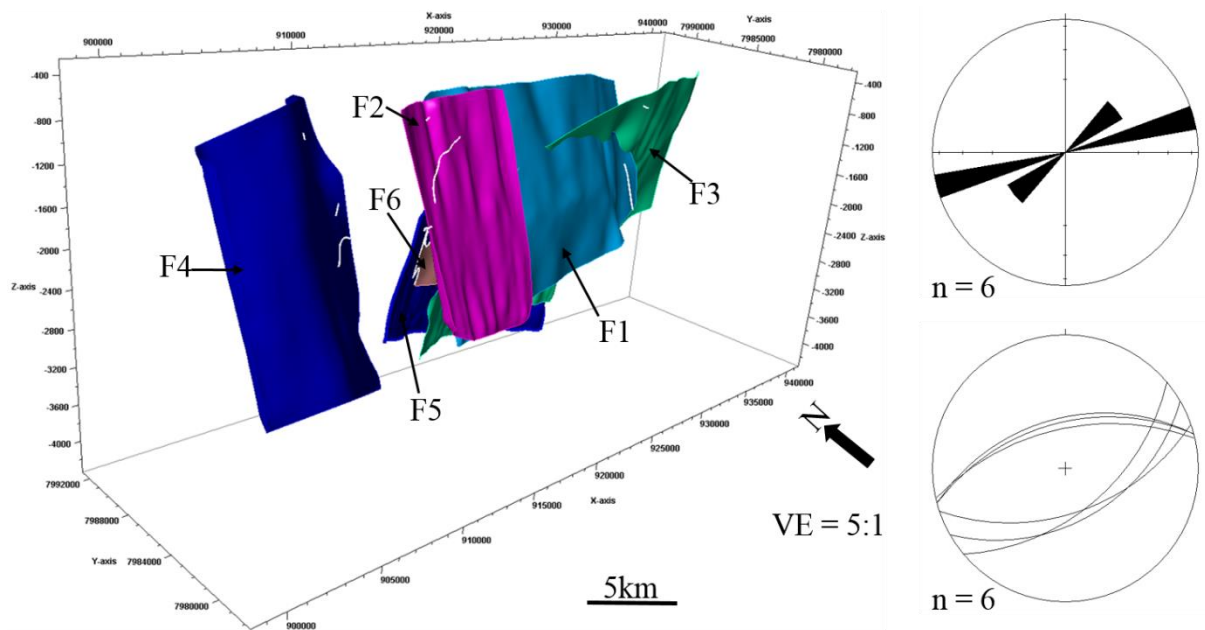
Figure 4.10 Fault plane geometry, rose diagram and equal area plot for the six major faults (Type A) in the study area. The faults extend down to the Triassic, Permian and Carboniferous formations and their upper tips are reaching to Eocene.

48
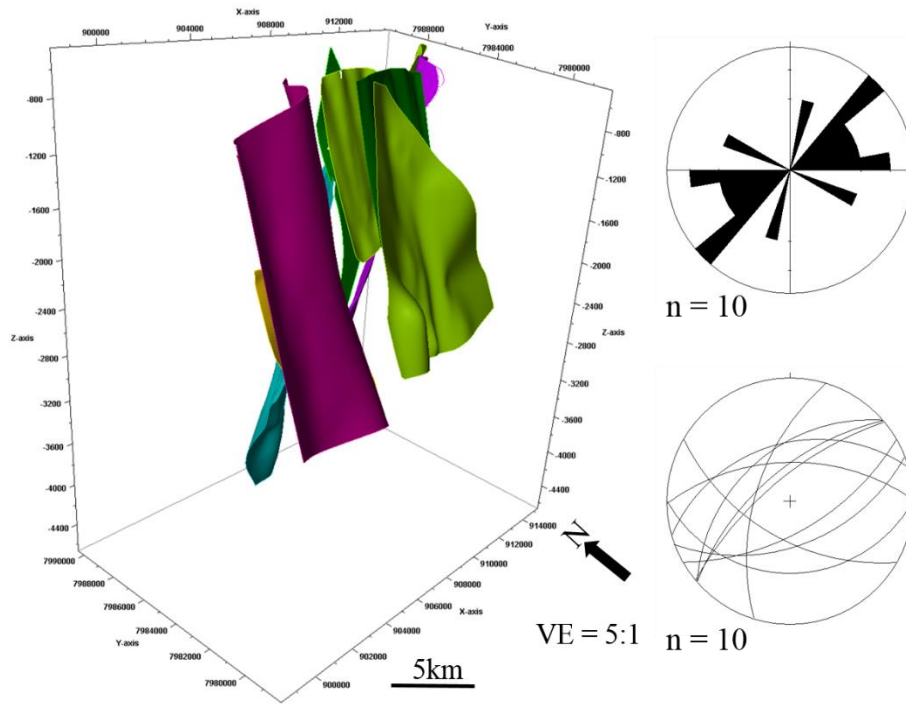
Figure 4.11 Fault plane geometry, rose diagram and equal area plot for the intermediate faults (Type B) in the study area..
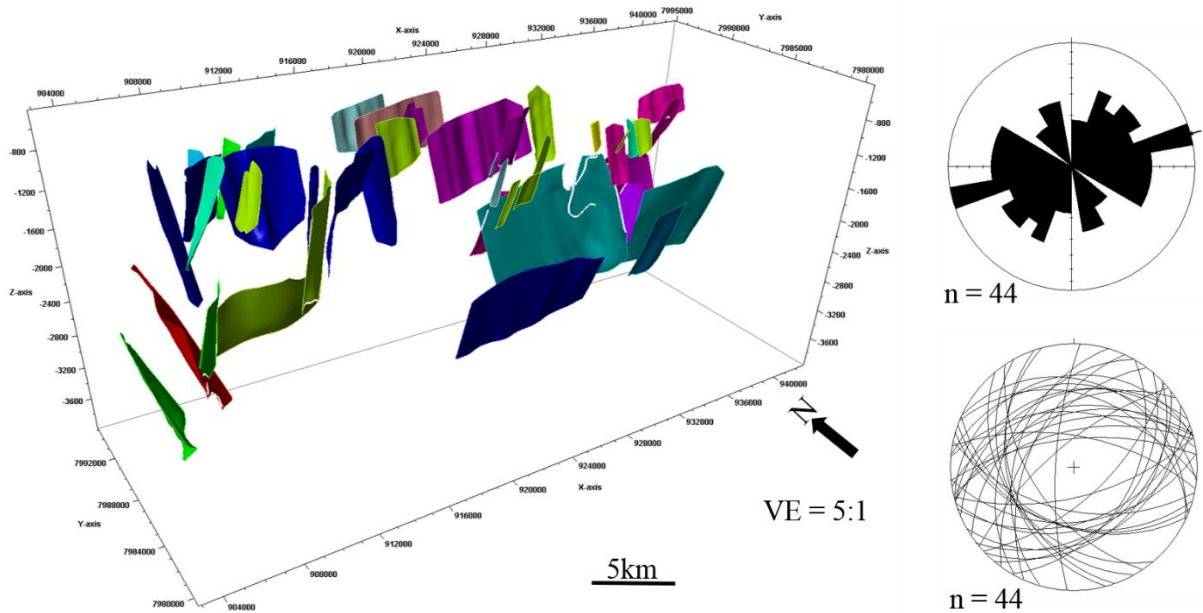
Figure 4.12 Orientation of minor faults (Type C) in the eastern and the western parts of the field.

The strikes and dips of F1, F2 and F3, and F4, F5 and F6 are relatively similar but with different dip directions. The strike/dip of F1, F2 and F3 are 076°/60°SE, 078°/64°SE and 078°/68°NW, respectively. For F4, F5 and F6 strike and dips are 083/65SE, 082/60NW and 084/36NW, respectively. The dip of the faults varies from ~40° to 80° with dominant strike of 070°-080°/60°-070°SE/NW (See Appendix Table A1).

4.2.3 Drag along faults

Fault drag along the flanks of the major faults on Units U-6a and U5 has been observed. Both normal and reverse drags are observed along H4, H5 and H6 (Figure 4.14). The cause of the these drag structures may be related to: (1) lithological changes; (2) sudden change in throw and displacement along these horizons from normal drag at the first phase and progressive sediment buildup along the fault plane to form reverse drag, and (3) more regionally caused by subsidence followed by uplift causing normal and reverse drags. The first and second reason is more possible because of the drag effect is observed only in these units and variation of the normal and reverse drag on F3. This may imply variation in degree and timing of reactivation of each of the faults.
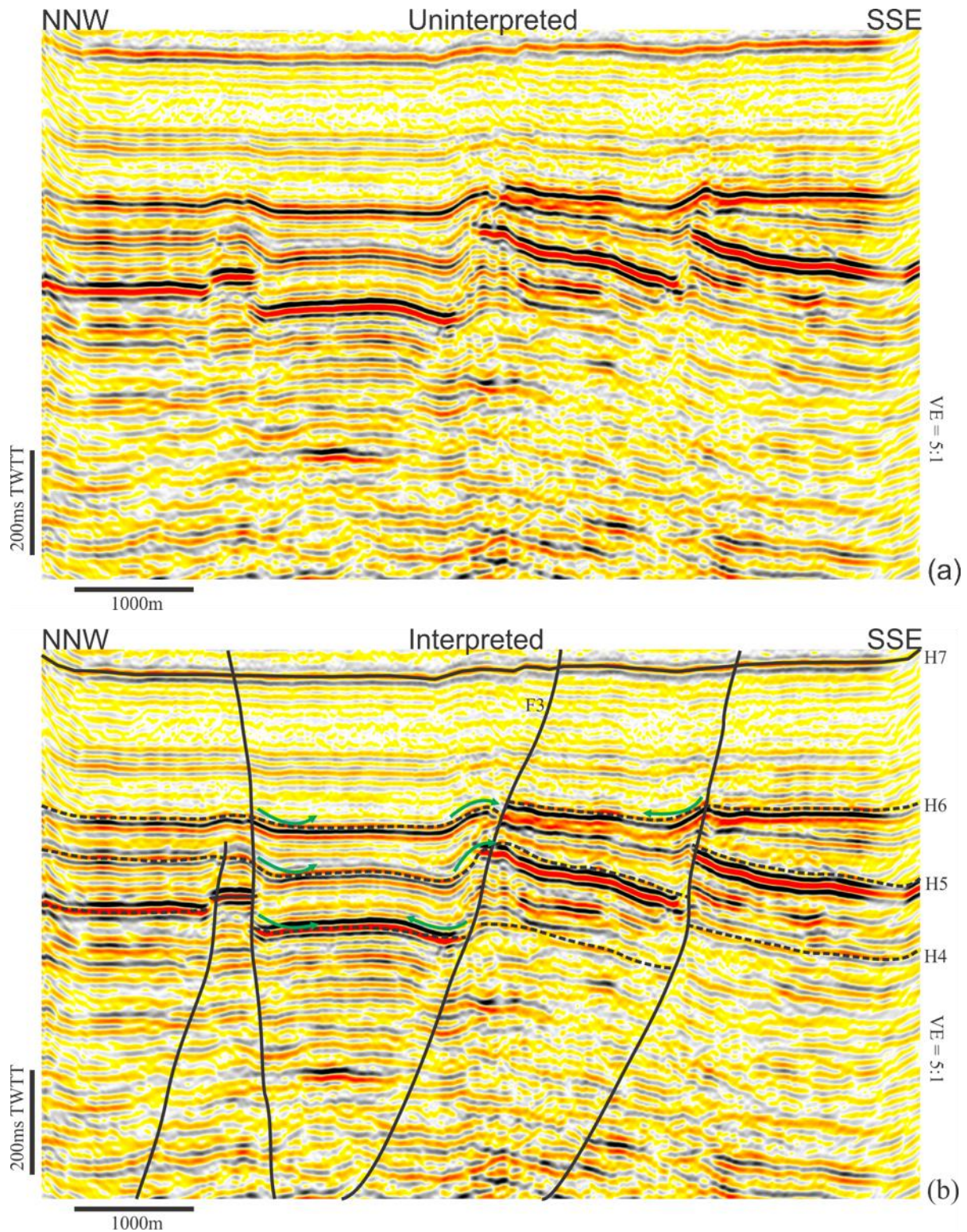
Figure 4.13 Normal and reverse drag example along the faults forming convex and concave up (indicated by green arrow) along the slip of the fault, respectively. The drag along F3 on H5 and H6 forms reverse drags, reflectors deflect upward while on H4 the drag is a normal drag (NB: This figure is enlarged on the drag structure of Figure 4.5).

4.2.4 Throw versus depth (t-z) plots

Fault 1 (F) has a gentle negative t-z gradient (-3.4), and a decrease in throw with depth from its basal tip to H8 with maximum throw of ~140 m on H5 (Figure 4.14). The maximum t-z gradient is recorded on H5 for all faults except F6 in which the maximum gradient is on horizon H3. Further upward from H3 the gradient is steep. Some increase in throw has been observed for less than 100 m. Toward the upper part, throw values decrease up to minimum throw values of ~10 m and zero at upper tips.

The lower parts of Fault 2 (F2) and F1 have similar t-z plot profiles. F2 has a negative t-z gradient (~5.5), a decrease in throw as depth increases, with an increase in values from its basal tips to the H4 and maximum throw value of ~130 m measured on H5 (Figure 4.14). The throw values decrease from H5 to H6. However, above H6 the throw profiles are opposite to F2, generally increasing towards the upper tip. Towards the upper tip, the throw gradient decreases rapidly to zero.

Fault 3 (F3) has a very gentle t-z gradient in its lower part and decreases in throw values upward. Below H4 the gradient becomes steep and negative (~-2.8) and increases further to H5, with the maximum throw value of ~65 m (Figure 4.14). Toward the upper part, the throw values decreases until it reaches zero at the upper tip.

Fault 4 (F4) has steep gradient to its basal part with maximum throw values of ~70 m on H5. The throw values decrease from H6 upward and become zero (at the middle) (Figure 4.14). Similarly, Fault 5 (F5) has steep negative t-z gradient in its lower part and the throw increases towards H4 with maximum of ~110 m between H4 and H5 (Figure 4.14). The throw value decreases from the H5 to its upper part with different values of positive t-z gradients.

Fault 6 (F6) and F4 have positive t-z gradients throughout their profiles, gentle t-z gradient in the lower part which decrease towards the middle (Figure 4.14). The minimum gradient in the middle of the F6 profiles could suggest dip linkage, but with further modification of throw values during fault reactivation.
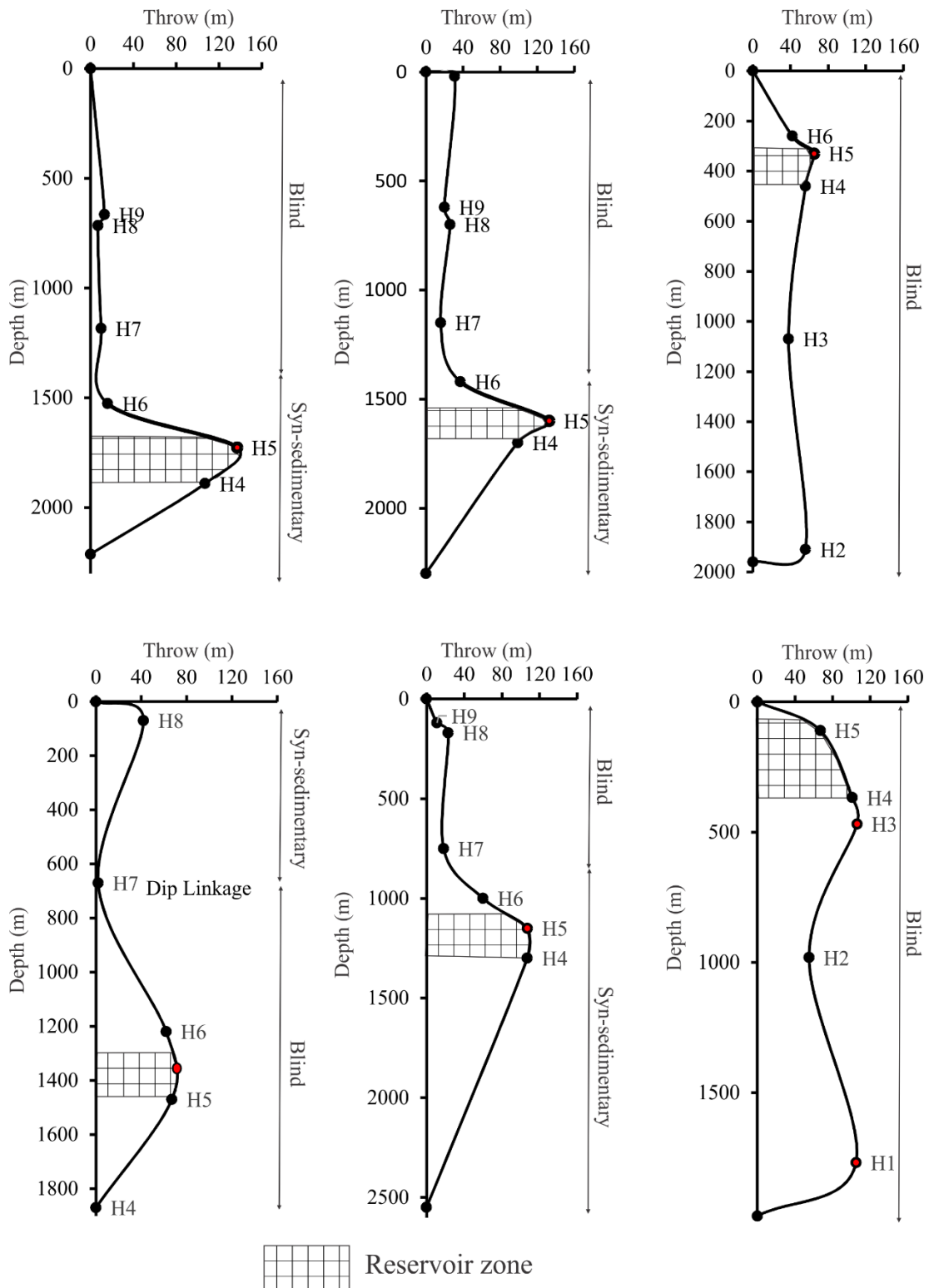
Figure 4.14 Throw-depth (t-z) plots of the six major faults from (a) to (f) for F1 to F6, respectively. F1, F2, F3 and F5 have relatively steep gradients towards the lower part of the throw profiles with maximum throw at H5 with increase from the H4 to H5. The general shape of t-z profile of F3, F4 and F6 shows dip linkage while F1, F2 and F5 does not show this character. *N.B: the red dot indicates location of the maximum throw value.*

4.2.5 Displacement versus distance (t-x) plots

The displacement-distance (t-x) plots of F1 have lower displacement from the origin and progressively increase with distance along the H4 horizon (Figure 4.15c). The maximum displacement value has been recorded on H5 for most of the faults. The displacement along this horizon is almost zero (Figure 4.15b). This is related to lateral merge of two or more different faults along the strike. This fault has generally multi-skewed C-type profiles and maximum displacement peak varies in each of the three key horizons with two dominant maximum displacement (dmax) (see Appendix Figure A1). Based on this, two major segments have been identified (Figure 4.15a).

The displacement-distance (t-x) plots of F2 are changing displacement frequently along the H4 (Figure 4.17). The t-z plot along the H5 increases from its origin and 370 m maximum displacement was recorded on this horizon (Figure 4.15e). The t-x plots of H5 and H6 are relatively similar except some increase towards the origin along H6 (Figure 4.15d and Appendix Figure A2).

The displacement-distance (t-x) plots of F3 increases with distance (Figure 4.15g-i). Along H4, an abrupt displacement increase has been observed along H5 reaching up to an average displacement of 700 m (Figure 4.15h and also see Appendix Figure A3).

In contrary to F3, the t-x plots of F4 have a maximum displacement (550 m) at smaller distance and minimum at higher distances (1.7 km) (Figure 4.16a-c). The maximum displacement is along H5 and lower upward (H6) and downward (H4) (Appendix Figure A4). The t-z plot of this fault is highly segmented along H4 (Figure 4.16a).

The displacement of F5 along the three horizons (H6, H5 and H4) is generally upward from H8 to H6. There is rapid local variation in displacement constant with the maximum displacement at H5 and lower at H6 and H4 (Figure 4.16d-f).

The displacement profile of F6 is different form the faults described before. The higher displacement was between 500 m to 5000 m (Figure 4.16g-i). The t-x plot along H4 has C-type profile along the H6 and H4 and M-type profile along the H5 (Muraoka and Kamata, 1983).

54
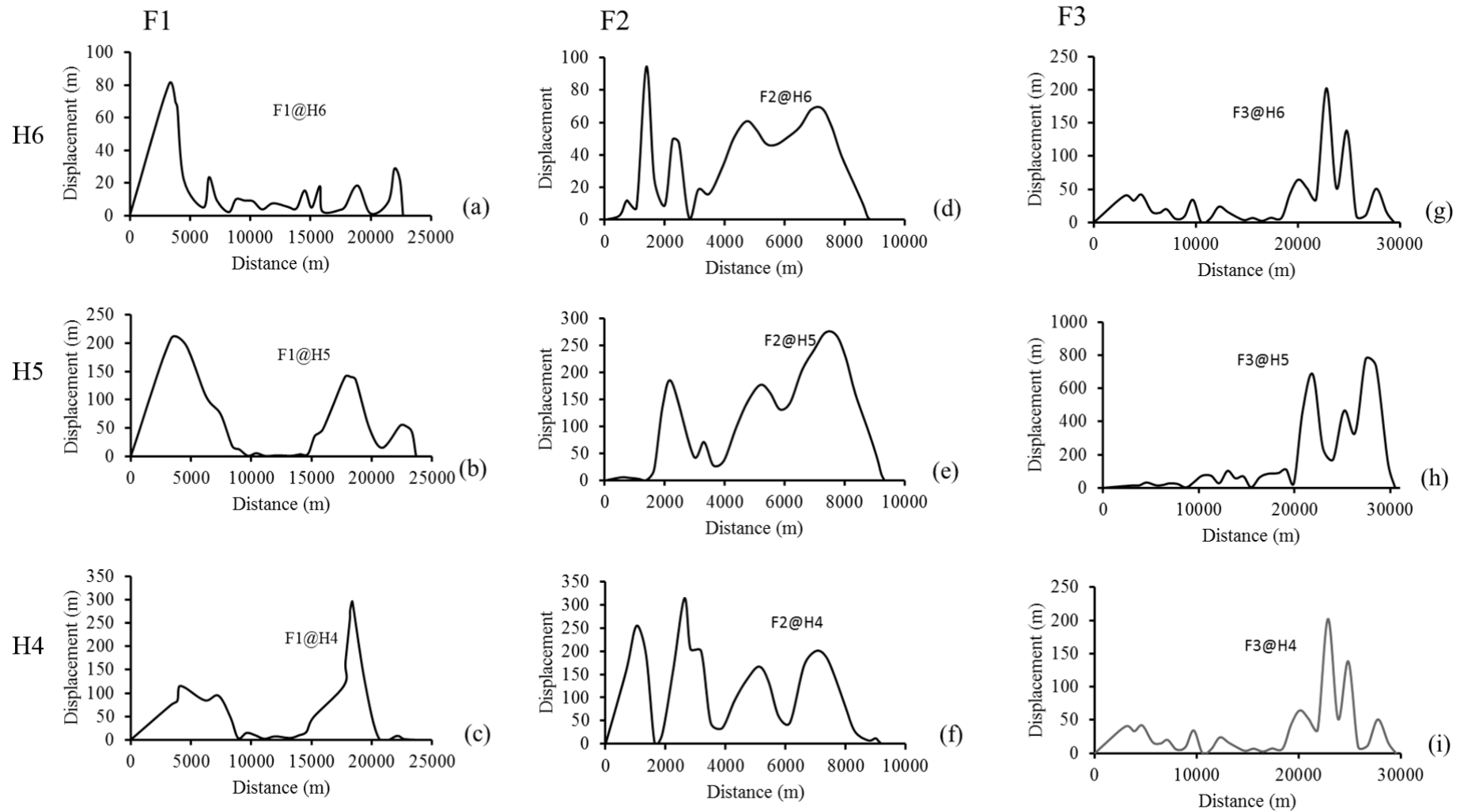
Figure 4.15 Distance-displacement (t-x) plots of F1, F2 and F3 along H6 , H5 and H4. The displacement is higher at shorter distance for H6 and H5 and for H8 at larger distances, and the displacement along H6 is less than along H5 and H4. The profiles are in general multi-skewed C-type profiles.
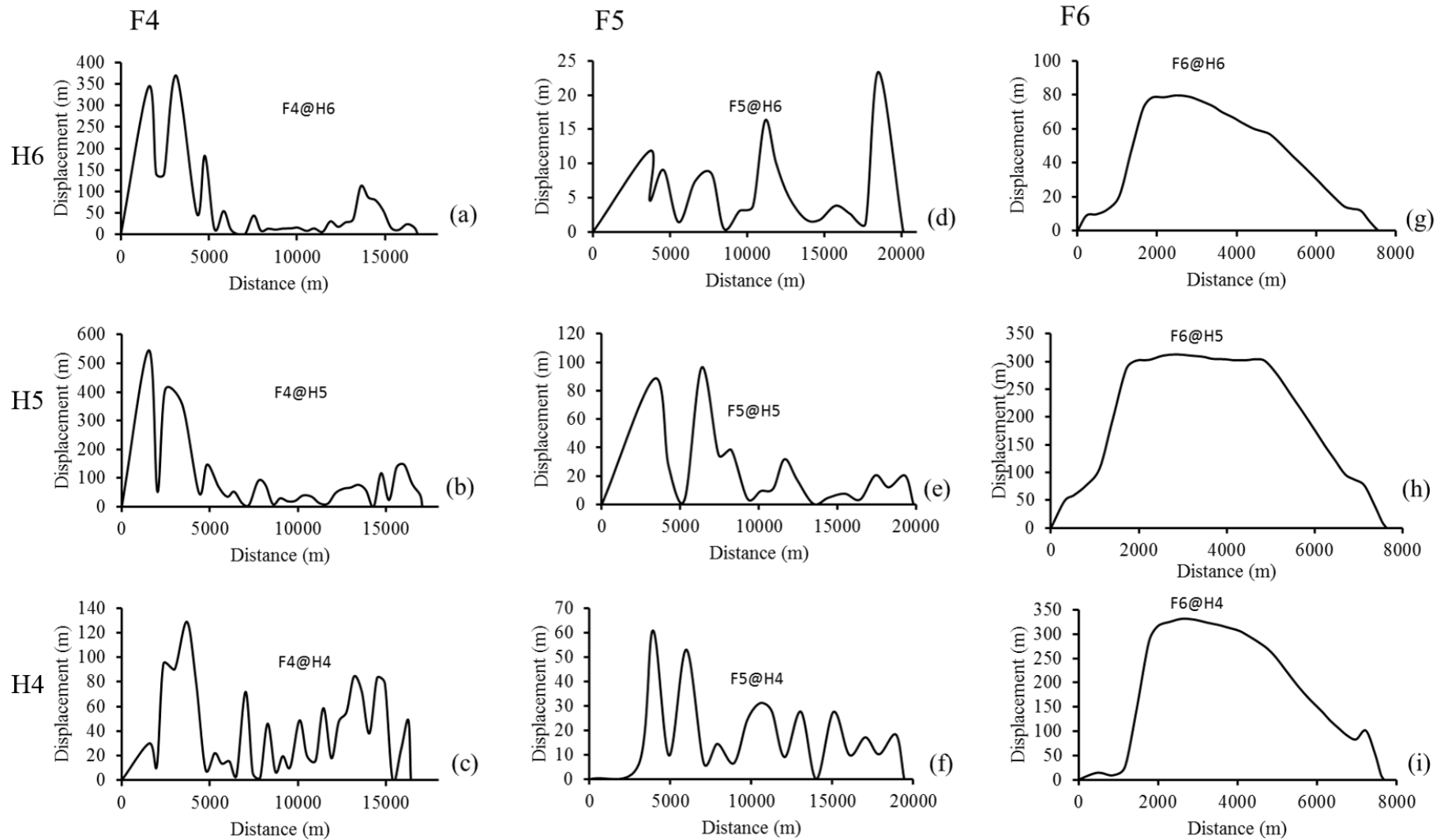
Figure 4.16 Distance-displacement (t-x) plots of F4, F5 and F6 along horizons H6, H5 and H4. The t-x profiles of F4 and F5 (a-f) show multi-skewed C-type profiles while F6 has skewed C-type profile on H4 and F6 and M-type profile on H5

4.2.6 Expansion and growth indices

Fault 1 (F1) has expansion indices of greater than 1 for U5, U6 and U8 which implies thickening of sediments in the hangingwall section of the fault (Figure 4.17). No change in EI was observed for units U4 and U7 (Figure 4.17) while strata thinning at U9 are signified by EI < 1. The maximum expansion of F1 occurs on U5b. The maximum growth index was recorded on U8 (GI = 0.018) (Figure 4.18). The expansion indices along Fault 2 (F2) show thickening of hangingwall strata on Unit 5 and no change in thickness from U6 to U9 (Figure 4.17). In contrast, the growth index of U5 is negative and > 0 upward to U7, U8 and U9.

Similarly, the expansion indices of Fault 3 (F3) are almost one on all of the Units except U5. The maximum growth index is on U5 (0.28). In contrast to the above, fault expansion and growth indices for Fault 4 (F4) have thickening on the hangingwall strata of U6, U7 and U9 and thinning on U4, U5 and U8 (Figure 4.17). Most of the stratal units have negative GI values. On U6 the growth index approaches 0.5 indicating the reverse drag as observed on the seismic sections (Figure 4.18). This could be informative for the negative values of GI are related to reverse drag by compression during the uplift. The normal fault reverse drag on U5 corresponds to the minimum growth index (GI = - 2) values along F3.

For Fault 5 (F5), there is strata thickening of the hangingwall section for U5b, U6, and U9 (Figure 4.17) and there is no thickness variation on the U2 (EI = GI = 0). The maximum expansion and growth indices measured on U5b along F5 are 1.1 and 0.3, respectively. And, progressively decrease in expansion and growth indices upward till U8 (Figures 4.17 & 4.18).

Consequently, The expansion indices strata units along Fault 6 (F6) does not show thickness variation on U4, U5a and U6 and maximum expansion index of 1.4 and growth index of 0.3 has been recorded on U5b (Figure 4.18). Generally, the expansion and growth indices indicates thickening on the hangingwall stratal and fault growth on U5.
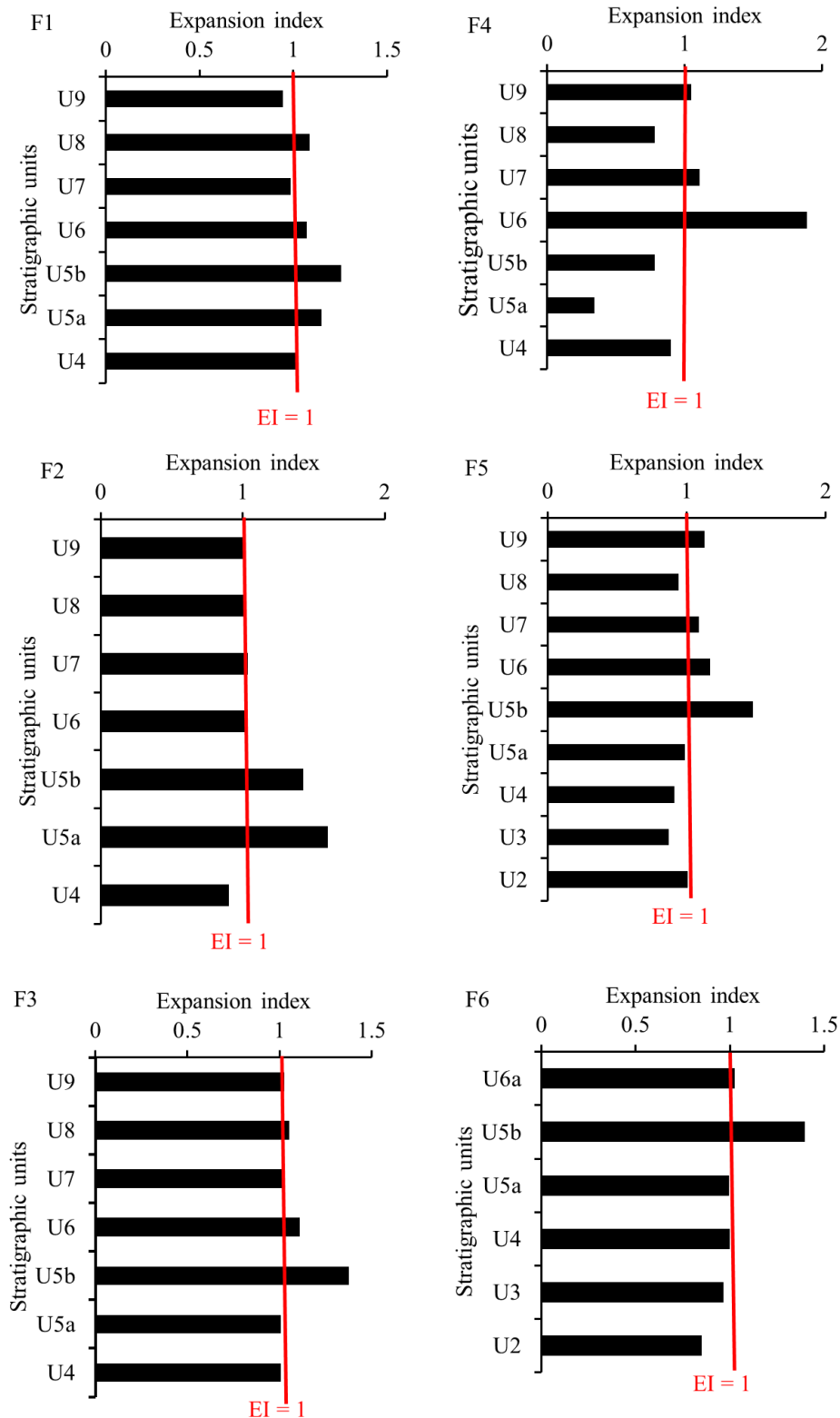
Figure 4.17 The expansion index for the major faults showing strata thinning/thickening. EI > 1 implies thickening of the hangingwall section while EI < 1 means thinning.
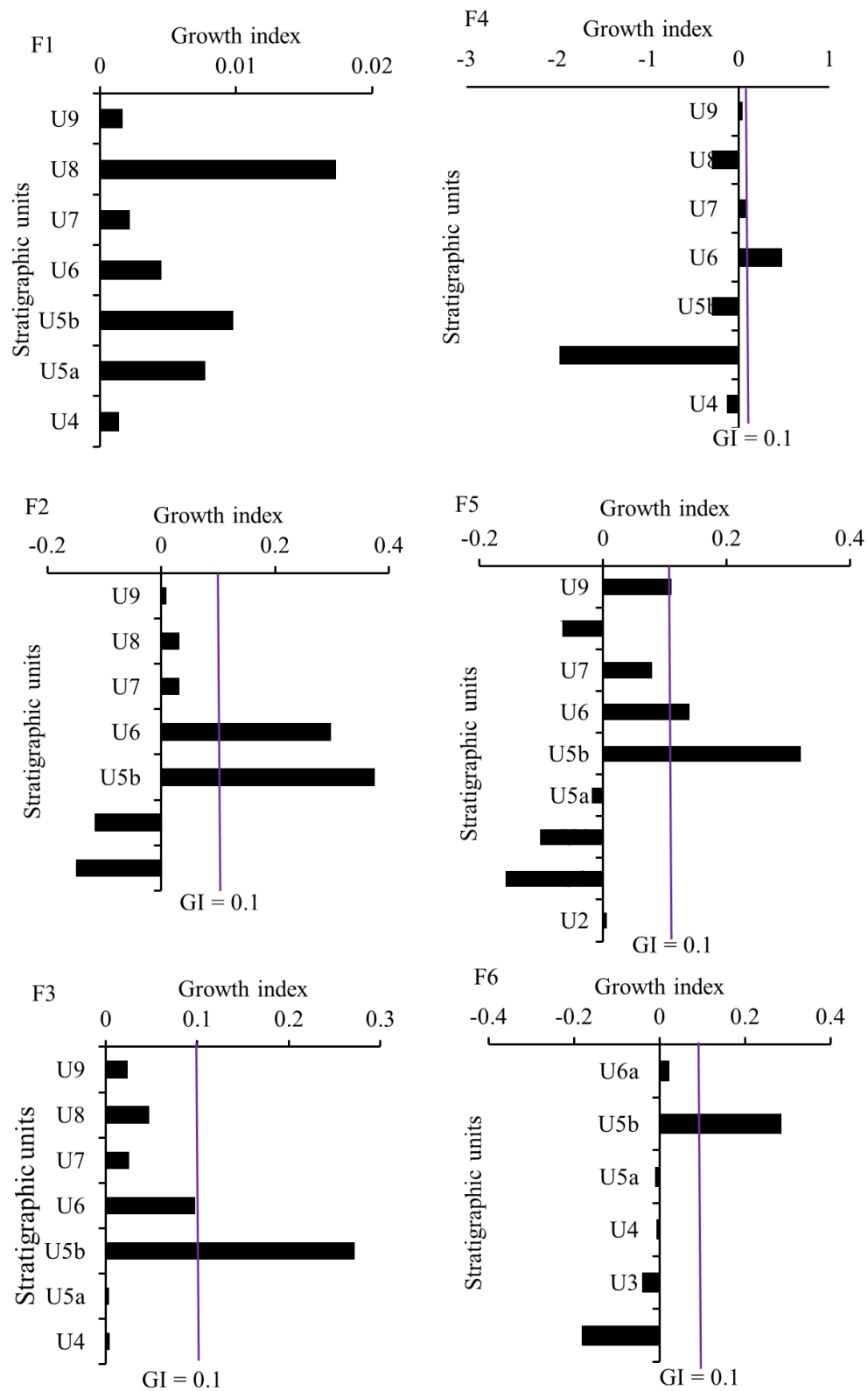
Figure 4.18: The growth index for the major faults . GI > 1 implies the fault interacted with a free surface during its growth while GI < 1 means blind faults.

4.3 High-amplitude anomalies (HAAs)

4.3.1 Interpreted HAAs

Soft-on-hard anomalies in this work are thought to be related to subsurface fluid accumulations and were mapped based on the following criteria; (1) their high amplitude values, (2) opposite polarity to the seabed reflectors, and (3) structurally unconformable to the background reflectors (Alves et al., 2015; Calvès et al., 2008). Nine high-amplitude anomalies or 'soft-on-hard' reflections were interpreted and displayed in Figure 4.19. The anomalies are spatially dominant in the eastern and western parts of Unit 9. Most of the anomalies (A1, A2, A3, A6, A7, A8) occur approximately at the same stratigraphic (600-700 ms TWTT) level within the Torsk Formation while anomalies A4 and A5 are hosted within the Kveite/Kviting Formations. On the E-W oriented seismic sections, most of them are intersected by the upper tips of the deep-seated normal faults, while the others are juxtaposed by the minor faults.

Furthermore, RMS amplitude extraction was done on the seismic volume and the nine mapped soft-on-hard HAAs were further examined. The result shows more anomalies which were not visualized during anomaly mapping. The geometry and character of each of the anomalies are discussed as follows:
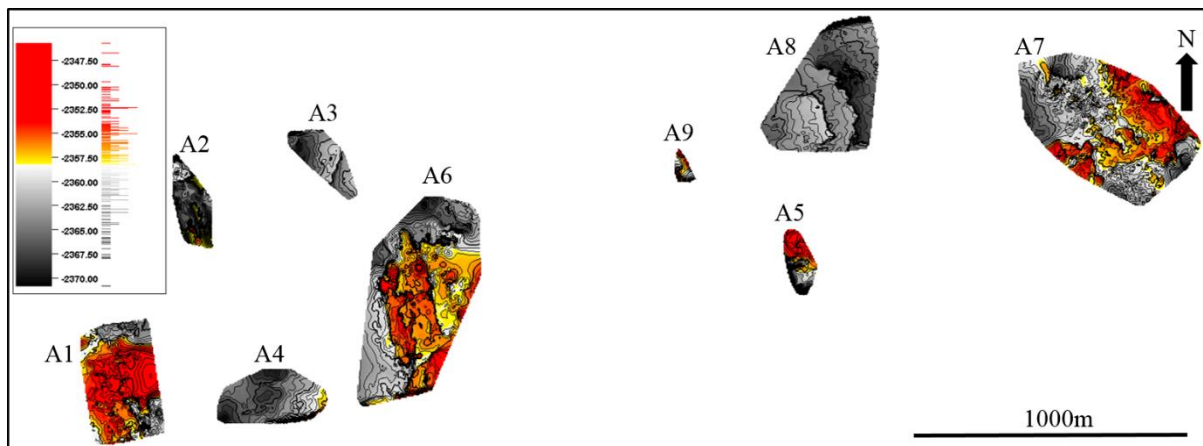
Figure 4.19: 2D planar view of the interpreted HAAs and their spatial distribution in the Snøhvit Field. Anomalies A2, A3, A5, A7 and A9 are oriented NW-SE, A6 and A8 NNE-SSW, A1 in the N-S and A4 E-W.

Anomaly 1 (A1)

Anomaly 1 (A1) is located in the western part of the study area approximately 600 m below the seabed. The anomaly is characterized by strong, high-amplitude reflectors, with reverse polarity to the seabed (Figure 4.20a & b). It is structurally unconformable with the background reflectors and cross-cuts stratigraphy. A1 is bounded on the top by a strong toplapping reflector of the Ha (arbitrary horizon, erosional unconformity) and on the bottom by the downlapping bottom reflectors of the host package. The anomaly extends 4.3 km in the north-south direction and 2.5 km in the east-west direction (Table 4.1) and covers an area of ~10.8 km^2 (Figure 4.20c). Spatially, this anomaly is intersected by a deep-seated fault (F4) and some other NNE-SSW trending faults (Figure 4.29). The bright nature of the NW-SE fault zone on the time slice may show a channel flowing along the fault scarps (Figure 4.20c and see Appendix Figure A7).

Anomaly 2 (A2)

Anomaly 2 (A2) is located in the northwest margin of the field, oriented in N-S direction and approximately 3.6 km in a N-S direction and 1.3 km in an E-W direction (Figure 4.19 and Table 4.1). This anomaly has strong negative amplitude and shows reverse polarity as compared to the seabed. The reflectors in this anomaly are structurally unconformable with the background reflectors (Figure 4.21a & b). Below this anomaly the reflectors are affected by the acoustic masking of a gas chimney. This gas chimney is the second largest gas chimney and extends from the Triassic to Paleocene formations. The anomaly is located 616 m below the seabed and covers an area of ~3.2 km^2. It is intersected by upper the tips of fault F4 and some local small faults (Figure 4.21c).

Anomaly 3 (A3)

Anomaly 3 (A3) is located to the eastern part of A2 in the northwestern part of the field and extends 3.3 km in a N-S direction and 1.2 km in an E-W direction (Table 4.1), approximately 664 m below the seabed. It is characterized by strong amplitude reflectors, polarity reversal as compared to the seabed and structurally unconformable with the background reflectors (Figure 4.22a & b). It covers an area of approximately ~3.2 km^2 (Figure 4.19). The RMS amplitude shows local variation in this anomaly and is intersected by east-west trending faults and by the upper tip of fault F4 (Figure 4.22c).

Anomaly 4 (A4)

Anomaly 4 (A4) is located in the southwestern margin of the field, is approximately 3.8 km in an E-W direction and 2 km in a N-S direction (Figure 4.23c and Table 4.1), and approximately 1300 m below the seabed, covering an area of ~6.2 km^2. The reflectors in this anomaly have relatively similar high-amplitudes except where the polarity reversal has been identified on the anomaly (Figure 4.23a & b). It is also structurally conformable with the background reflectors in Unit 8 (Figure 4.23a). The amplitude decreases upward towards to the east and it is separated by the NE-SW striking faults from the other anomaly to the northwest. It is located on the upper part of the major fault F4 (Figure 4.23a).

Anomaly 5 (A5)

Anomaly 5 (A5) is located in the central part of the field approximately 2.3 km north-south direction and 1 km in east-west direction (Figure 4.19 and Table 4.1). The reflectors are locally high and strong in the anomaly zone and polarity reversal has been noticed as compared to the seabed (Figure 4.24b). It also structurally conformable with the background reflectors (Figure 4.24a). It is located in a depth of 1112 m and its calculated area from the surface maps is ~2 km^2. However the RMS amplitude extraction shows as the anomaly further extents of the anomaly, to the east with very strong RMS amplitude and to the west relatively lower amplitude distributed within the zone of polygonal faults. This suggests that the polygonal faults have been serving as local conduit which distribute the fluids laterally or vertically (A'5) (Figure 4.24c).

Anomaly 6 (A6)

Anomaly 6 (A6) is located in the central part of the volume in a depth of approximately 724 m beneath the seabed. It is extended 7.5 km in a NE-SW direction and 3.6 km in an E-W direction (Table 4.1) and covers an area of ~23.5 km^2 (Figure 4.19). This anomaly is located on the top of the largest gas chimney zone. This gas chimney reaches to the Triassic formations with decreasing masking effect downwards.   The reflectors in the anomaly are structurally unconformable to the background reflectors (Figure 4.25a). Polarity reversal relative to the seabed has been observed (Figure 4.25b). The boundary of this anomaly has a diffuse boundary to relatively lower RMS amplitude to the margin. Some other anomalies have been also identified at the same stratigraphic level which is distributed through the local smaller faults (Figure 4.25c).

Anomaly A7

Anomaly 7 (A7) is located in the eastern part of the field and is approximately 7 km in a NW-SE direction and 4 km in a SW-NE direction (Table 4.1). It is located at a depth of 700 m below the seabed and covers an area of ~23 km2. The reflectors in this anomaly are characterized by high amplitudes which have opposite polarity to the seabed (Figure 4.26a & b). The reflectors in this anomaly zone also show reverse polarity as compared to the seabed (Figure 4.26b). Its distribution in a NE-SW direction may be influenced by local faults (Figure 4.26c).

Anomaly 8 (A8*)*

Anomaly 8 (A8) is located in the northeastern part of the field and is approximately 5 km in a NE-SW direction and 3 km in a NW-SE direction (Figure 4.19 and Table 4.1). It is located at approximately 670 m below the seabed and covers an area of ~14.5 km^2. The reflectors of this anomaly are very strong amplitude characterized by polarity reversal as compared to the seabed and structurally unconformable with the background reflectors (Figure 4.27a & b). This anomaly is lined-up with upper tip of F5 and some polygonal faults to the western and southern parts (Figure 4.27c).

Anomaly 9 (A9)

Anomaly 9 (A9) is located in the central part of the field and is the deepest and the smallest anomaly. It extends approximately 0.7 km in a N-S direction and 0.4 km in a E-W direction (Table 4.1). The anomaly located at a depth of 2360 m and covers an area of ~ 0.5 km^2. It has no spatial relationship with the major faults. Discontinuities have been observed even though faults were not identified in the region, probably related to depositional features. The anomaly was identified based on its locally strong amplitude reflectors and polarity reversal as compared to the seabed. Besides, the anomaly is structurally conformable with the background reflectors (Figure 4.28a & b). Even though it is small in size the RMS attribute is similar character, strong and which clearly isolated from the background (Figure 4.28c).

Table 4.1 The geometry and orientation of the anomalies , where the average length of the anomalies is twice of their width, and have spherical and rectangular shapes in a planar view (see Figure 4.19).

HAA	Length (m)	Width (m)	Aspect ratio	Shape	Elongation direction
A1	4252	2534	0.595955	Rectangular	NW-SE
A2	3615	1302	0.360166	Spherical	NW-SE
A3	3272	1248	0.381418	Rectangular	NW-SE
A4	3827	1953	0.510321	Spherical	E-W
A5	2340	983	0.420085	Spherical	NW-SE
A6	7549	3648	0.483243	Rectangular	N-S
A7	6942	4111	0.592192	Spherical	NW-SE
A8	4942	2990	0.605018	Rectangular	N-S
A9	681	362	0.531571	Rectangular	NW-SE
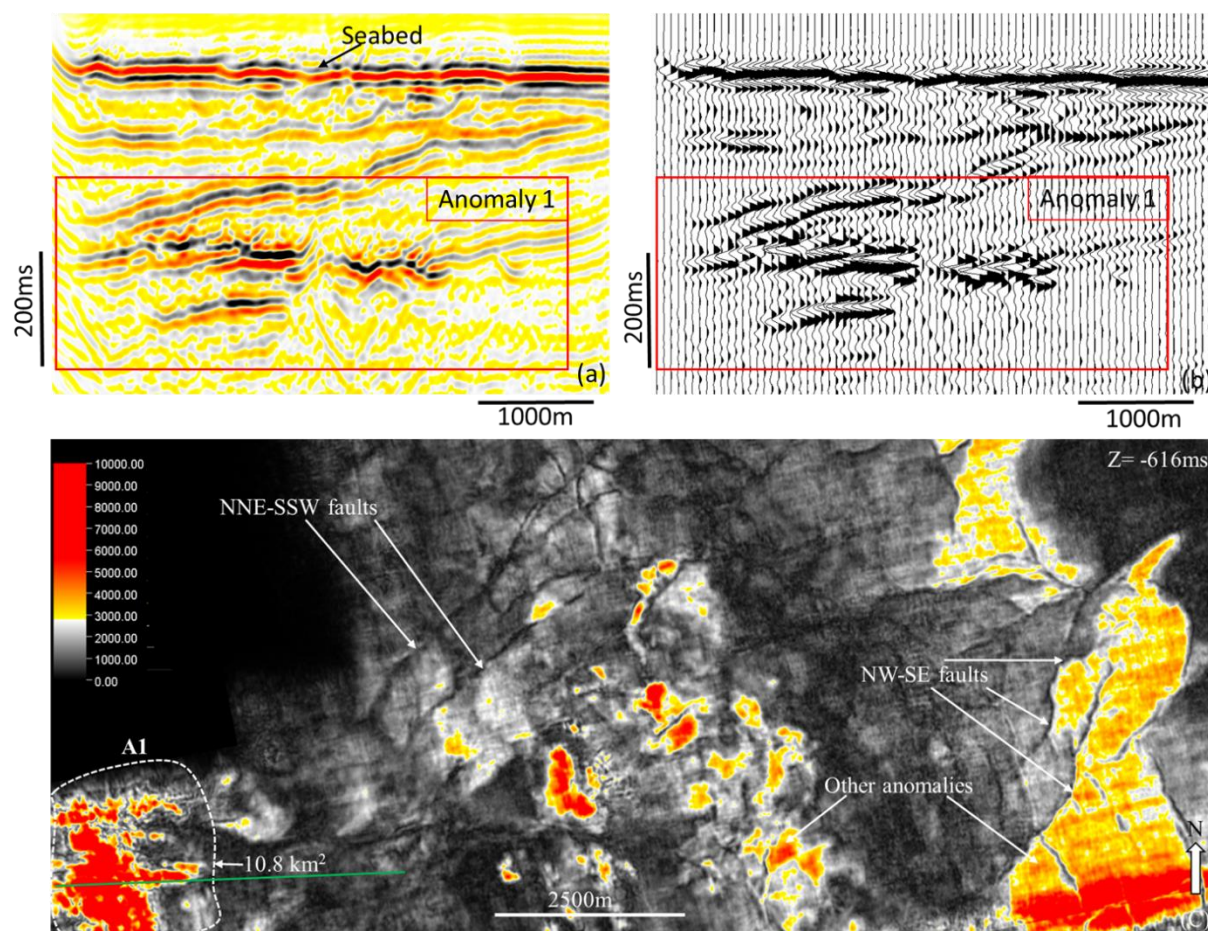
Figure 4.20: Anomaly A1 on the seismic section (a) as compared to the seadbed (b) seismic wiggle, showing polarity reversal of the anomaly as compared to the seabed and (c) RMS amplitude of A1 oriented north-south direction covering an area of 10.8 km^2 and some other anomalies at the same stratigraphic position. The NNE-SSW and N-E oriented faults are also reocognized on this RMS amplitude map at a depth of 616 m. The bright in the NW-SE fault zone may indicate a channel flowing along fault scarps. The green line is the location of the seismic section on (a).
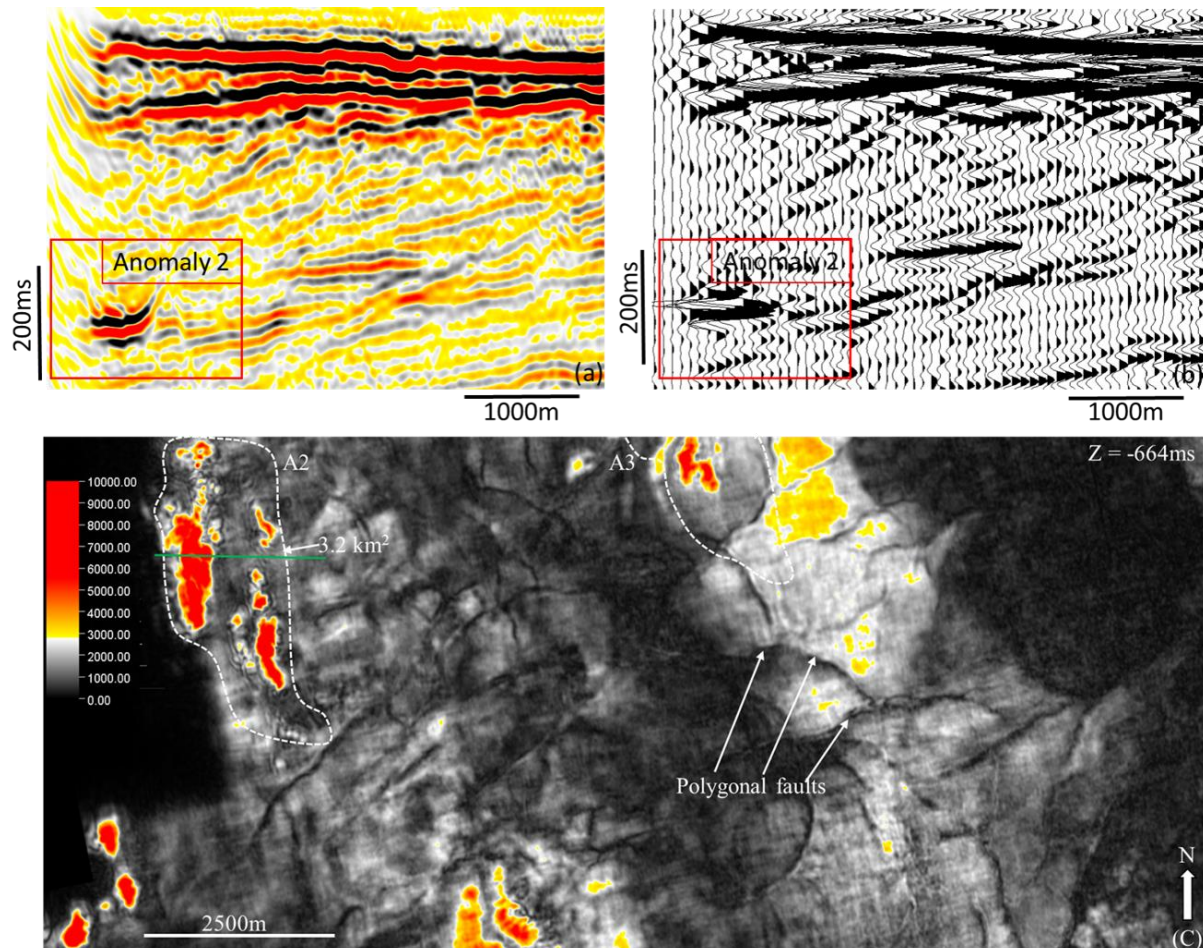
Figure 4.21 Anomaly A2 on seismic section (a) showing high-amplitude reflectors with to the seadbed (b) seismic wiggle, showing polarity reversal of the anomaly as compared to the seabed, and (c) the RMS amplitude map of A2 which extended in north-south direction covering an area of ~3.2 km^2. Polygonal faults may cause distribution of the anomaly as smaller pods. The green line is the location of the seismic section on (a).
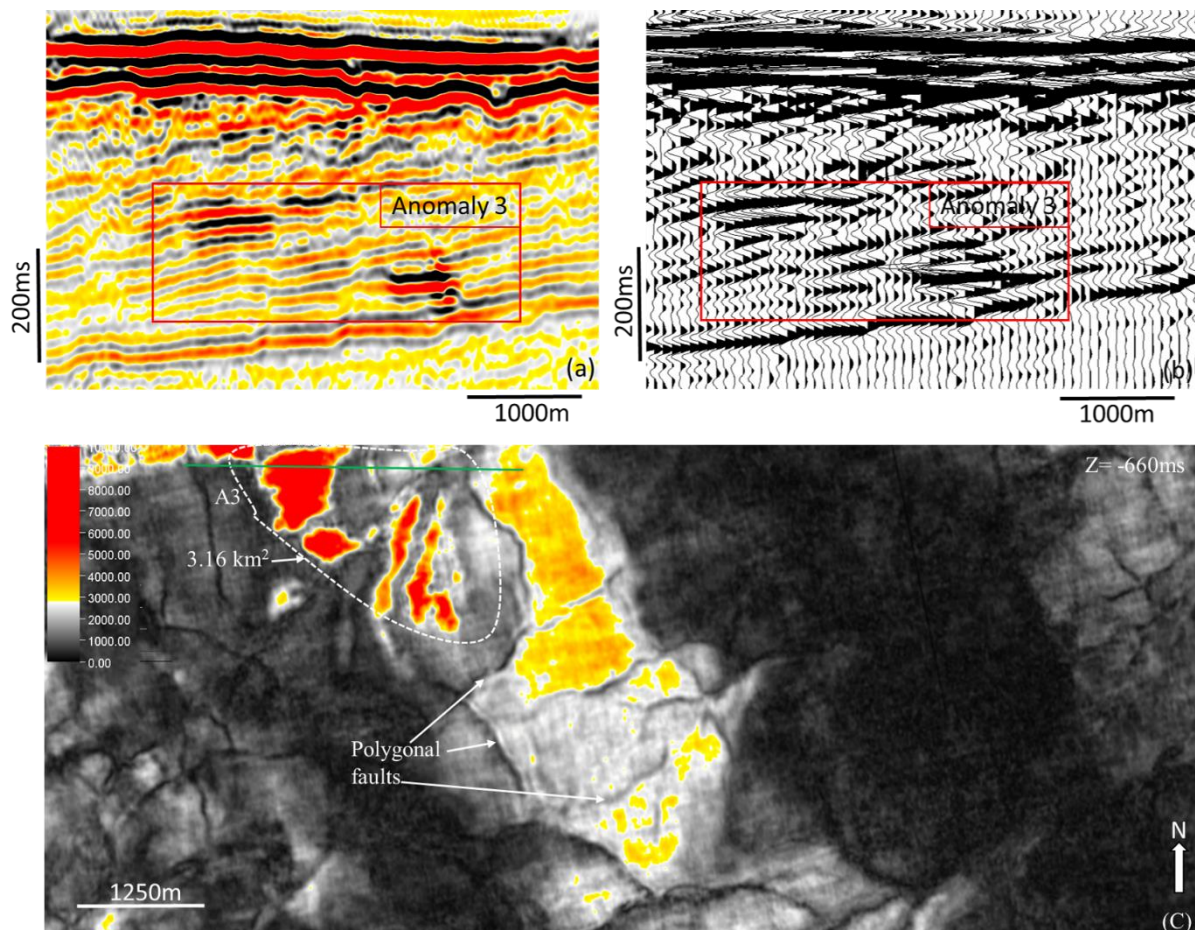
Figure 4.22 Anomaly A3 on a seismic section (a) showing high amplitude reflectors with (b) a polarity reversal as compared to the seabed reflector, and (c) RMS amplitude showing the extent of the anomaly covering an area of 3.16 km^2 and the relationship with polygonal faults. This anomaly is on the same stratigraphic position with A2. The green line is the location of the seismic section on (a).
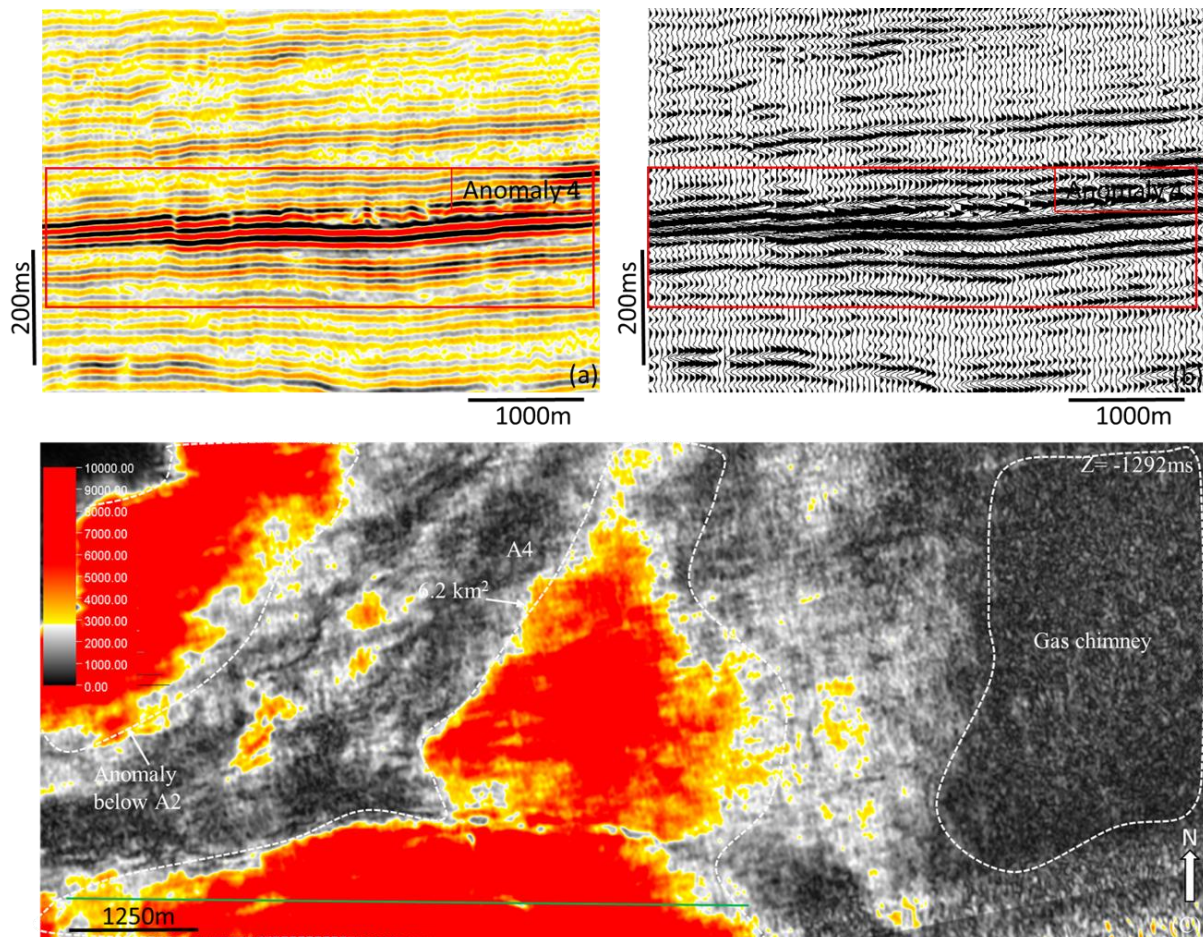
Figure 4.23 Anomaly A4 on a seismic section (a) where the top of the gas chimney is bounded by downlapping clinoform (package B) showing the control of the stratigraphy on the fluid accumulations. (b) This amomaly has high amplitude reflectors having a reverse polarity to the seabed and (c) covering and area of 6.2 km^2 , at ~1292 m depth, bisected by a fault which extends from the anomaly to northwest. The green line is the location of the seismic section on (a).
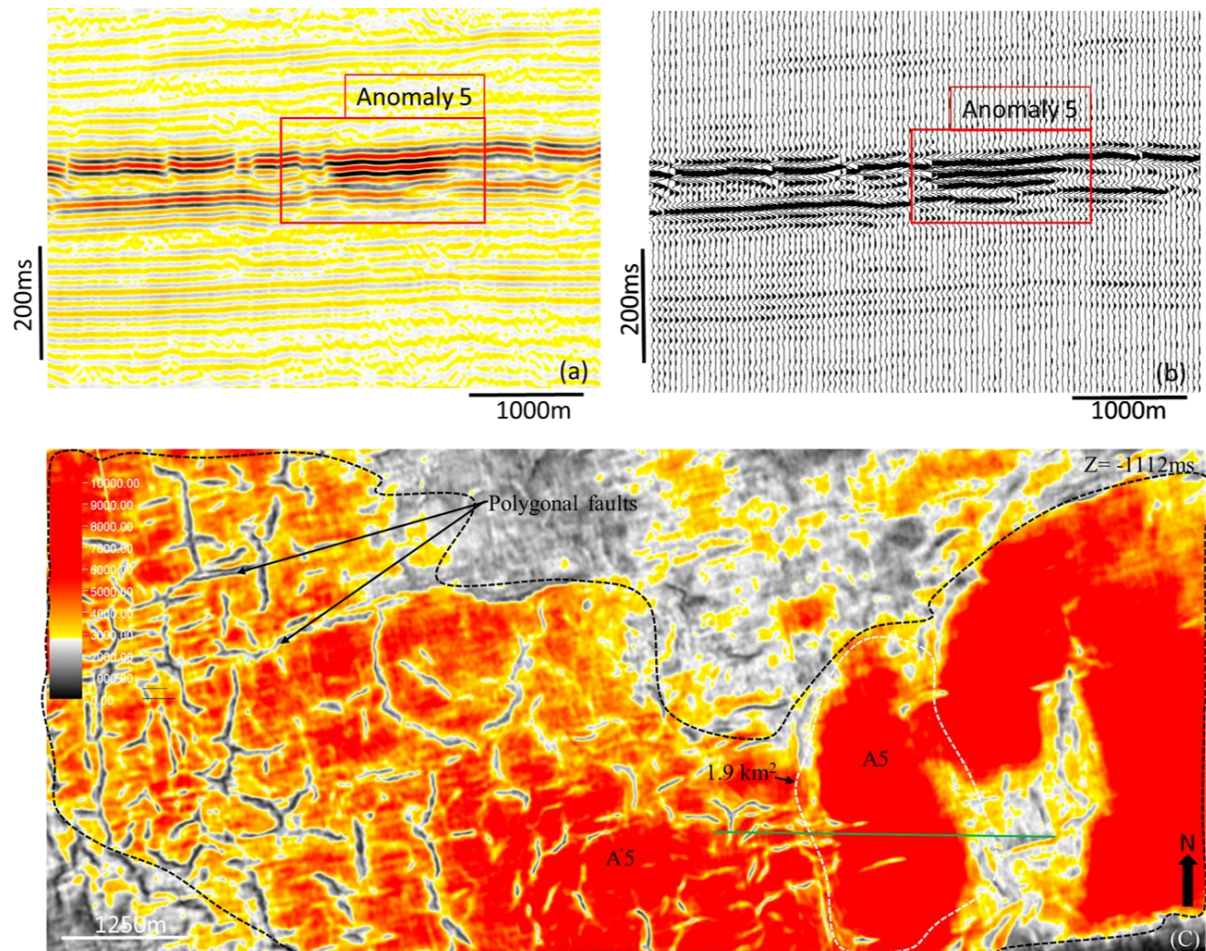
Figure 4.24 Anomaly A5 on a seismic section (a) showing high amplitude (b) in a reverse polarity and conformable to the background reflectors. (c) The anomaly during mapping (dotted line) was estimated smaller than extracted from RMS amplitude. The polygonal faults have an influence to disperse fluids laterally and vertically. The green line is the location of the seismic section on (a).
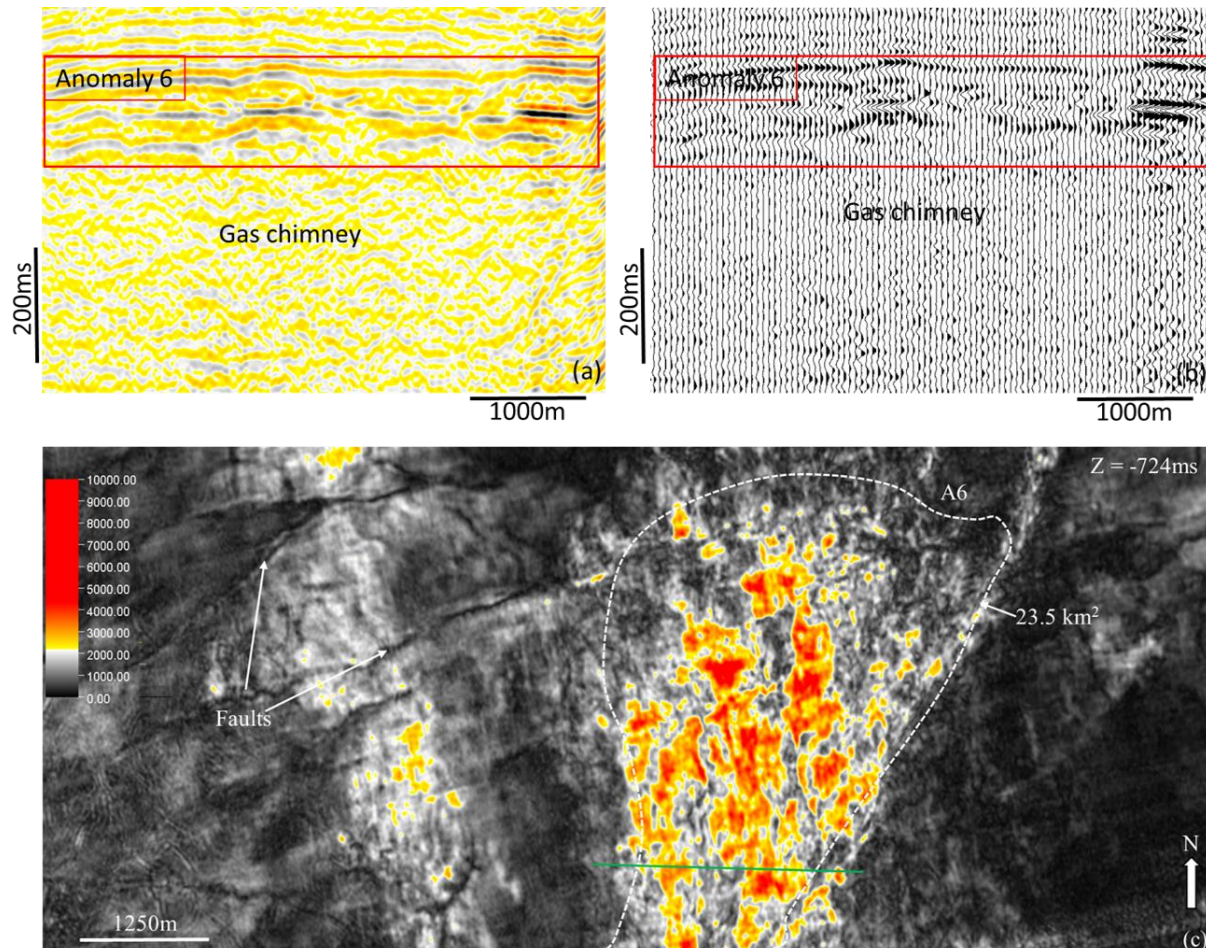
Figure 4.25 Anomaly A6 on a seismic section (a) showing the gas chimney which extends down to the Triassic formations (b) It has polarity reversal as compared to the seabed and structurally unconformable to the background reflectors. (c) This anomaly is highly affected by the polygonal faults which act as local conduit for laterally and vertically migrating fluids. The flow pattern is from south to the north direction and diffused out through the local polygonal faults and covers an area of 23.5 km^2. The green line is the location of the seismic section on (a).
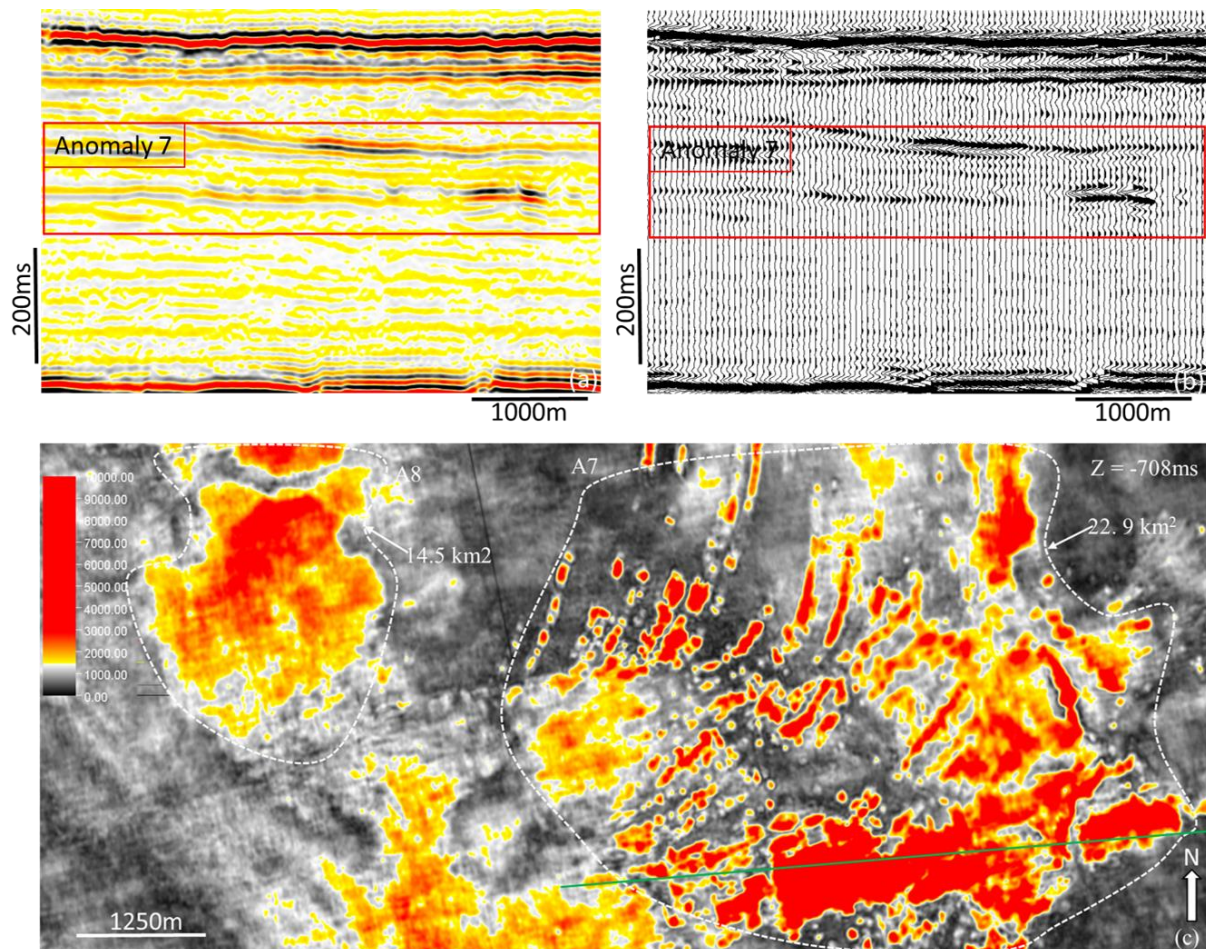
Figure 4.26 Anomaly A7 on a seismic section (a) showing high-amplitude reflectors, (b) cross-cutting the local stratigraphy with opposite polarity to the seabed. (c) The RMS amplitude extraction shows circular shaped and diffused anomaly oriented in NE-SW direction covering an area of ~23 km^2. To the west of this anomaly is relatively lower amplitude anomaly, and extended in a NW-SE direction along polygonal faults. A8 is also visible at this depth increasing in amplitude downward. The green line is the location of the seismic section on (a).
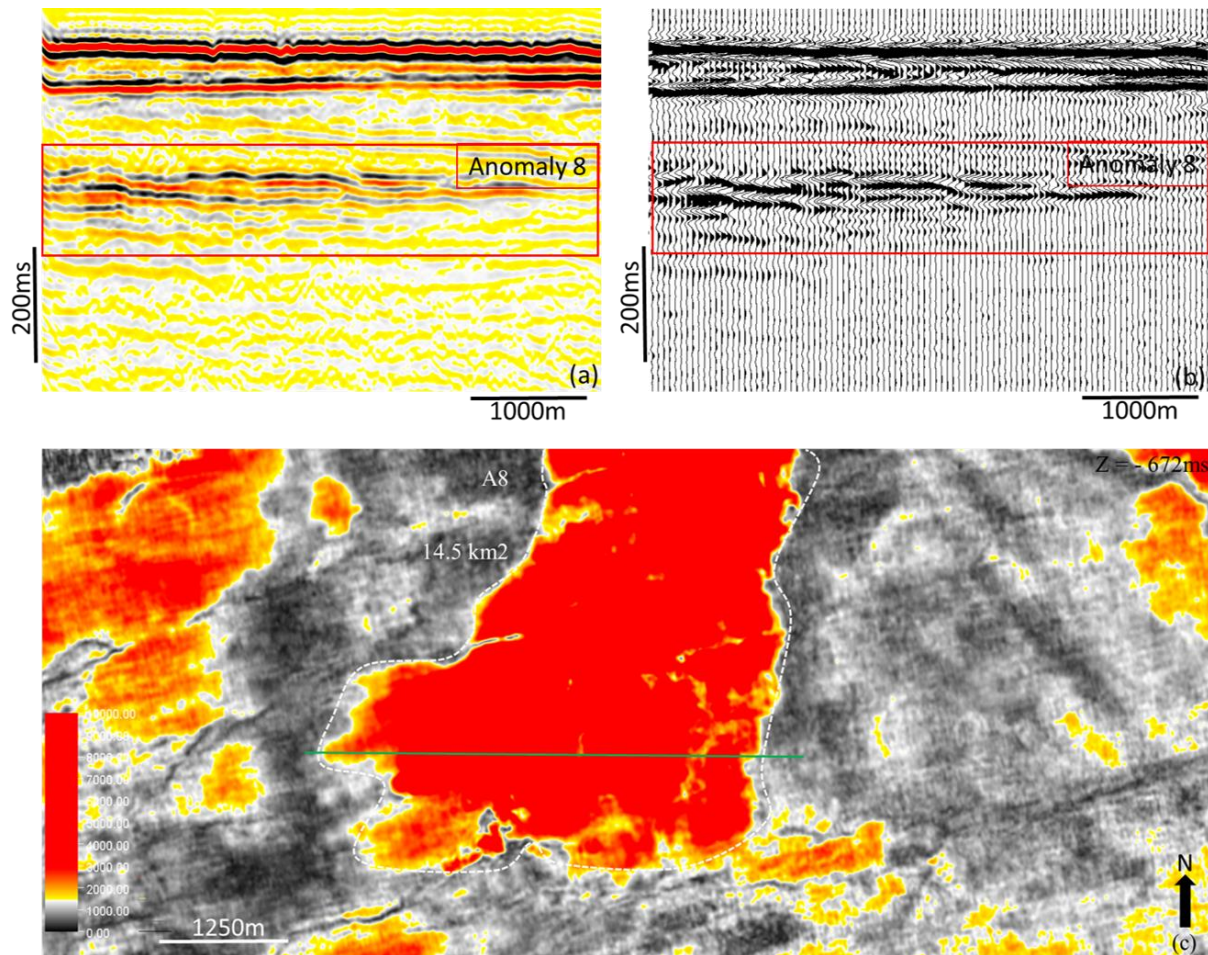
Figure 4.27 Anomaly A8 on a seismic section (a) showing high amplitude reflectors (b) in a reverse polarity as compared to the seabed, unconformably with the background reflectors. (c) It is located approximately at a depth of 672 m, in the western part of the field, covering an area of ~14.5 km^2. The green line is the location of the seismic section on (a).
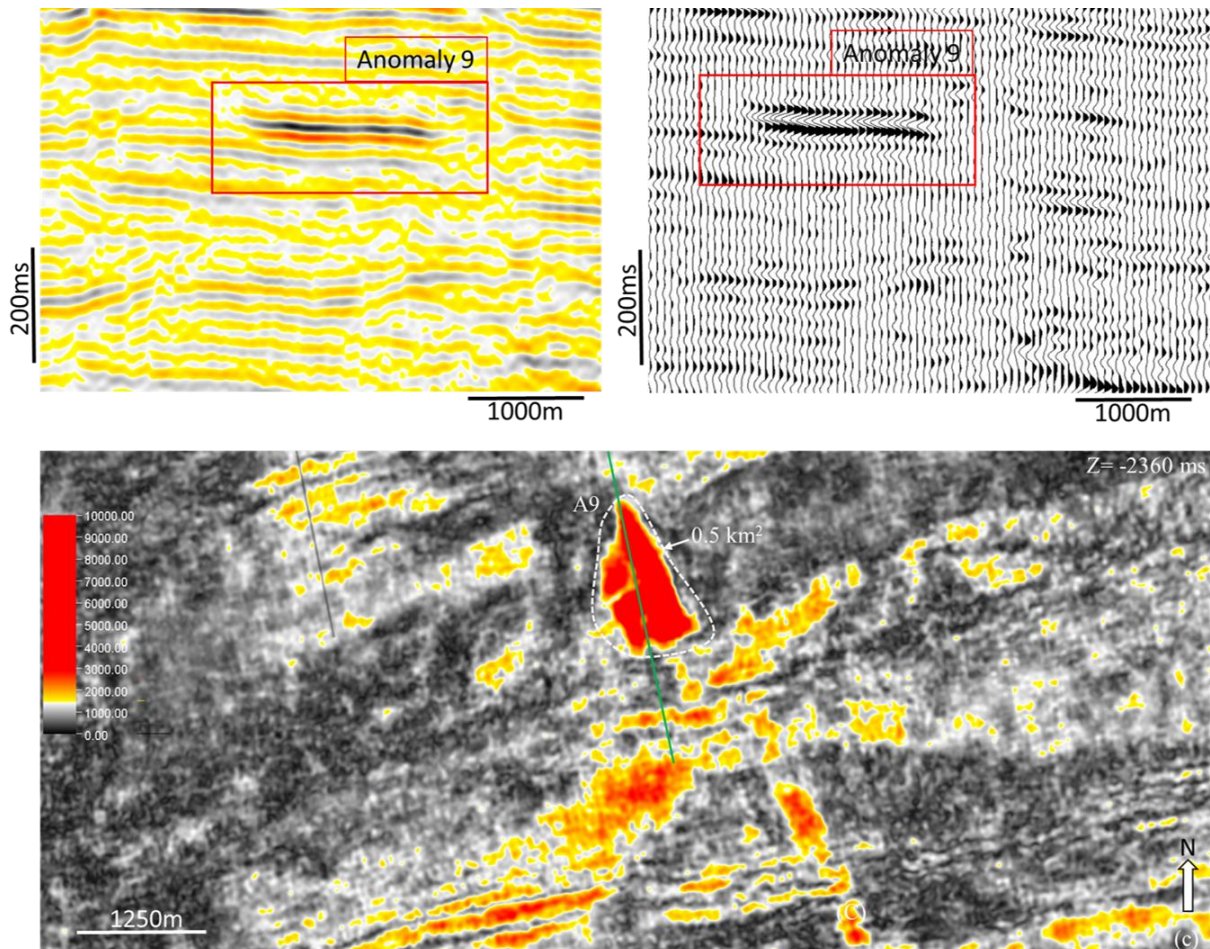
Figure 4.28 Anomaly A9 on seismic section (a) at 2360 m, in the Triassic formations (b) which has reverse polarity and conformable to the background reflectors. (c) The RMS amplitude also show this anomaly, covering an area of 0.5 km^2. The green line is the location of the seismic section on (a).

4.3.2 Spatial relationship of faults and high-amplitude anomalies (HAAs)

The HAAs are spatially related to the major Jurassic faults (Figure 4.29. Most of the HAAs are located on the hangingwall upper part of these faults. Furthermore, the seabed fluid flow features line up along the fault tips. Most observed pockmarks and buried pockmarks lie over the fault tips. The spatial relation of the seabed pockmarks is not restricted to upper tips of the major faults but also to the shallow intermediate antithetic faults (Figure 4.2). These antithetic faults have been acting as subsurface fluid conduits. The other interesting observation is that the HAAs have been observed on the top part of the major gas chimneys.
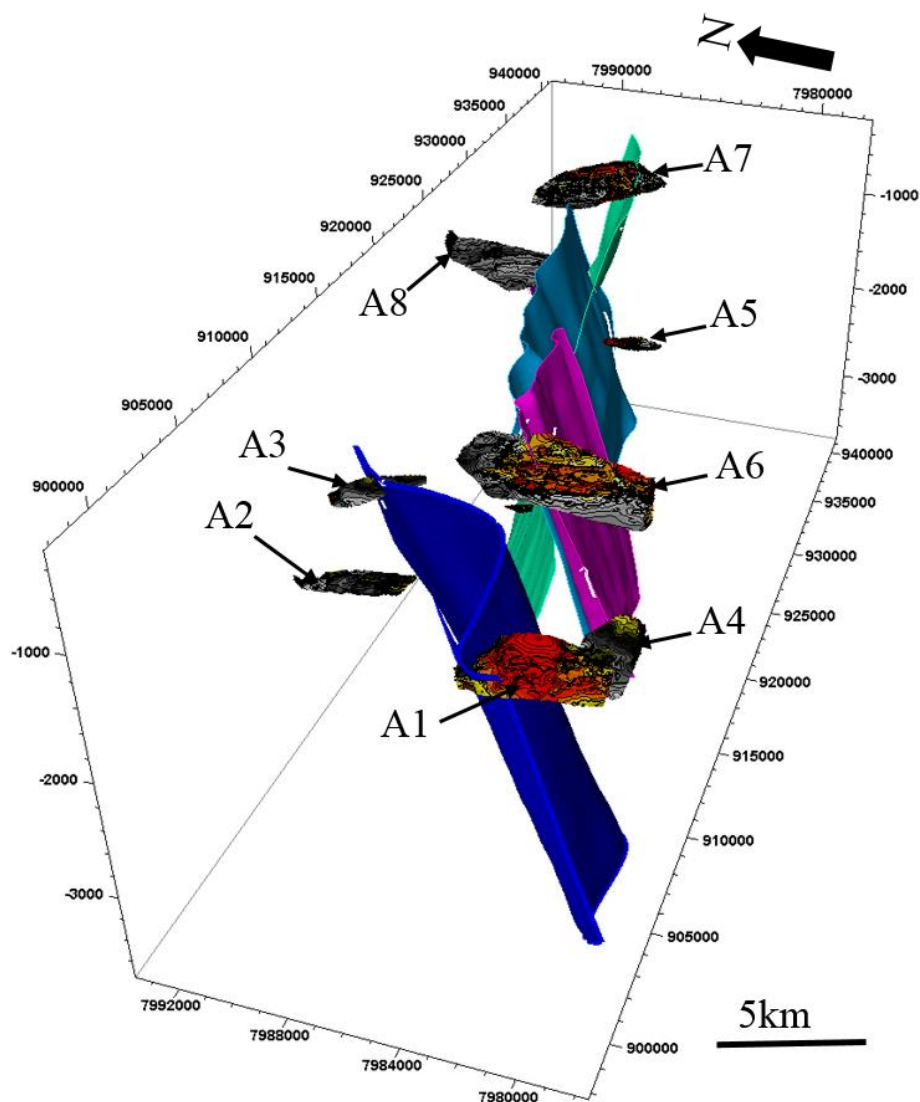
Figure 4.29 The spatial relationship of HAAs and the major faults . The HAAs are located on the top tips of the major faults (F1, F2, F3, F4 and F5), more towards the hangingwall side of the faults.

4.3.3 HAAs related to lithology

Very high-amplitude anomalies are dominantly observed in the western part of Unit 8, the reservoir zone and in Carboniferous Formations (Unit 1). These hard-on-soft anomalies have similar polarity to the seabed and are structurally conformable to the background reflectors. The anomaly in Figure 4.30 shows very high amplitude anomaly related to lithology in the Unit 8. The HAAs in the reservoir region are partly related to lithology and the presence of hydrocarbons (Figure 4.32). The HAAs in this zone are continuous throughout Unit 5.

Figure 4.30 Lithology related HAA located in the western part of the Unit 8 (Kveite/Kviting Formations) related to the lithological effect (Z = -1048 ms).

The anomalies in Unit 1 also show shifting upward to the west as the depth decreases. The geometry and shifting pattern of these features supports to interpret as a channel. However, flow patterns were difficult to recognize based on the extracted amplitude (Figure 4.31a & b).
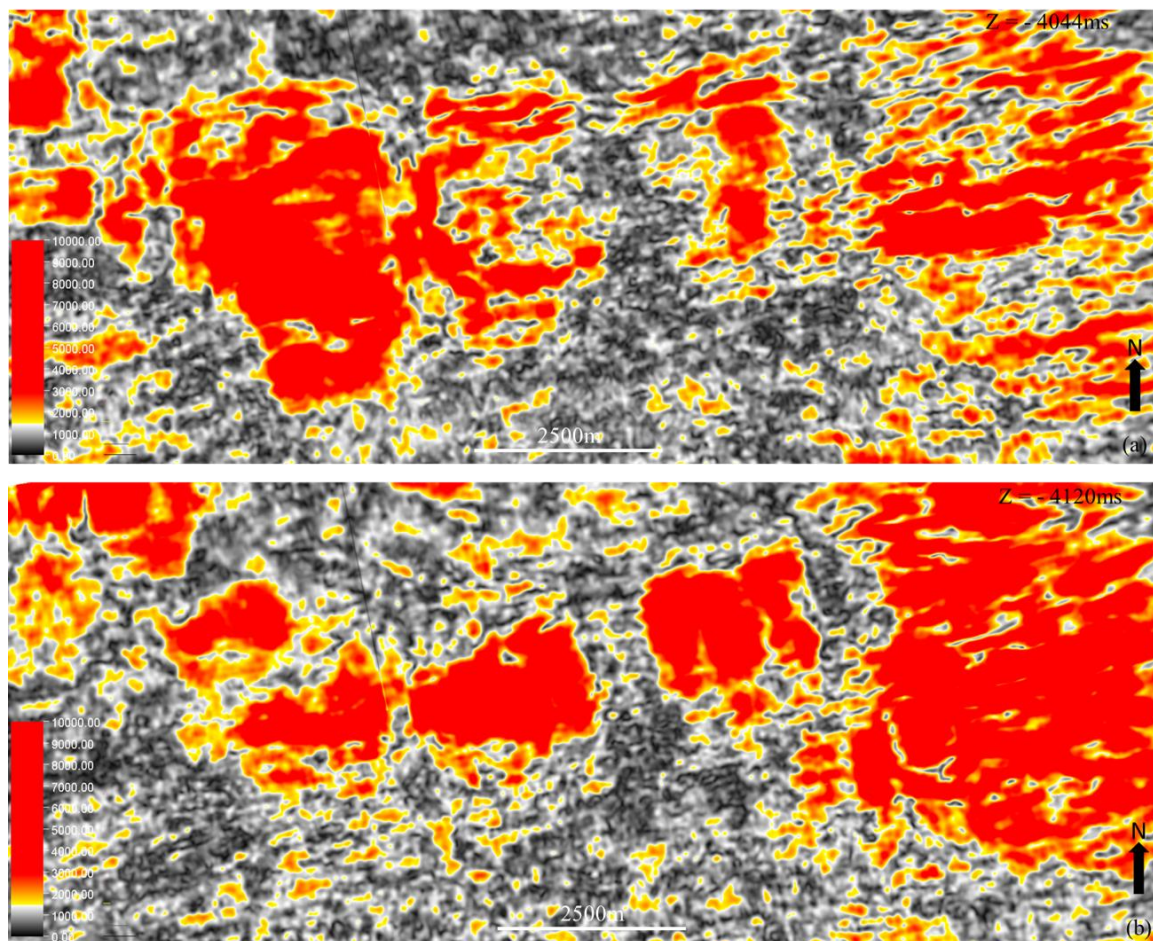
Figure 4.31 Interpreted channel feature using RMS attribute show shifting of flow from E to W direction (see Figures 4.3 and 4.4).

4.3.4 Migration pathways and hydrocarbon plumbing systems

Most of the HAAs are located in the hanging-wall and the upper part of the major deep-seated faults (e.g., A2, A3, A7 and A8). Others are spatially linked to the topmost part of the gas chimneys (e.g. A1 and A6). The geobodies extracted through RMS amplitude show both fluid and lithological related high-amplitude anomalies (Figure 4.32). The top and the bottom part were extracted for the fluid related anomalies while the lithological related anomalies extracted more solid geobodies (Figure 4.32).

The gas chimneys in this attribute could not be extracted. Conversely, the chaos and variance attributes were used instead to extract the gas chimneys in the south-western and north-eastern parts of the seismic volume (Figures 4.33 & 4.34). The variance extractions for the three major gas chimneys show vertically tabular (Gas chimney 1), conical (Gas chimney 2) and patchy

circular (Gas chimney 3) shapes (Figures 4.33 & 4.34). The gas chimneys extend from 3000ms (~3 km). The area of each gas chimney was estimated approximately as 12 km^2, 60 km^2 and 17 km^2, from Gas chimneys 1, 2 and 3, respectively. Based on this, approximately 276 billion m^3 volume of fluids has been migrated from the gas chimneys alone.
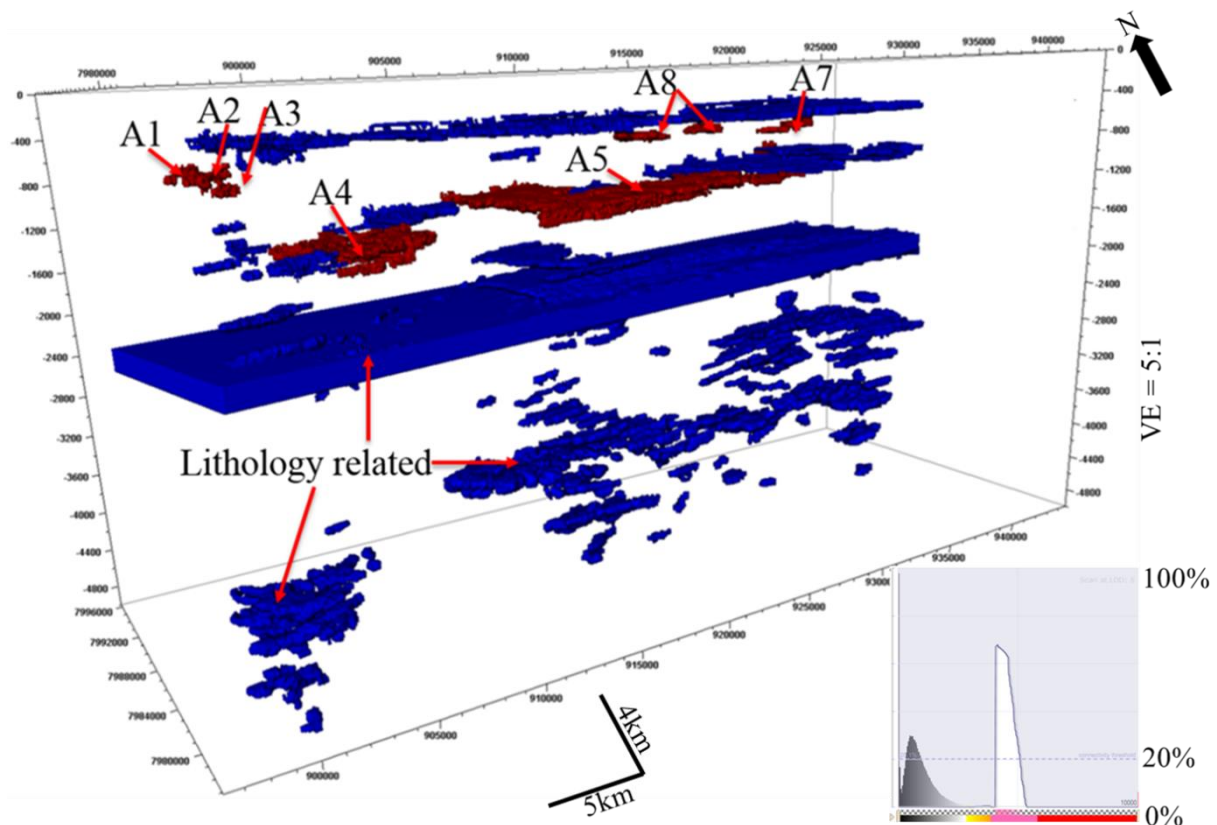
Figure 4.32 Fluid-related and lithology-related HAAs . The HAAs (red) and lithological related high-amplitude (blue) extracted from RMS amplitude using opacity threshold value of 20%. However, A6 is located on the top of the biggest gas chimney and it was not extracted with this threshold value.
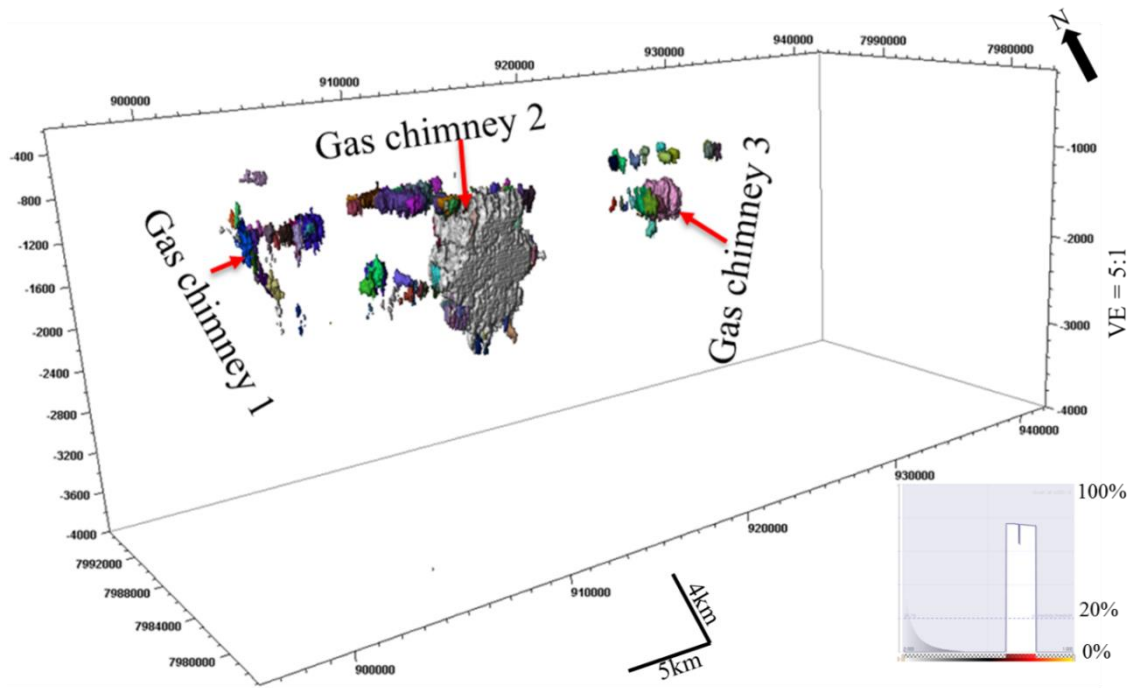
Figure 4.33 Gas chimneys extraction from variance attribute at the western (Gas chimney 1), southwestern (Gas chimney 2) and northeastern (Gas chimney 3) parts of the study area extracted as geobodies. Gas chimney 2 is the biggest gas chimney in the field where Anomaly 6 is located on the top pf this gas chimney.
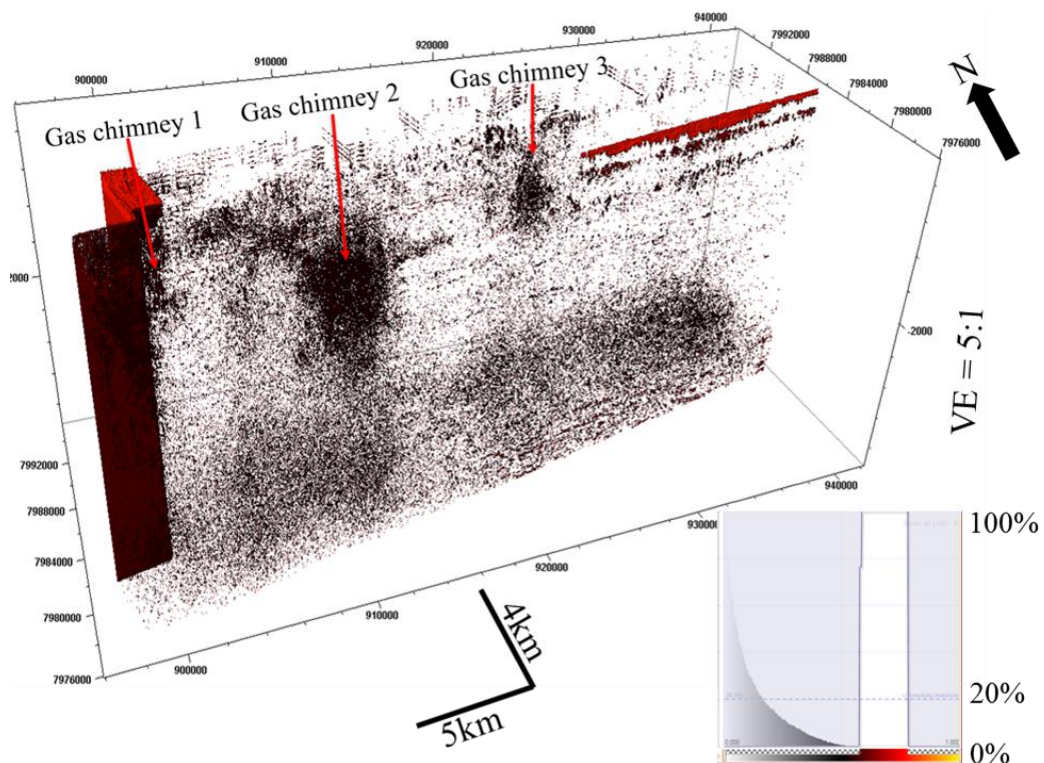
Figure 4.34 Gas chimneys extraction from chaos attribute in the southwestern and northeastern part of the study area. However, the lower part in this volume is not related to the gas chimney, and could be related to the lithological effect.

Chapter 5 Discussion and Conclusions

5.1 Discussion

5.1.1 History and growth of faults in the study area

Faults in the study area are normal dip-slip faults (Figures 4.8 to 4.13). Fault drag observed on some of the faults provided insights to mechanical heterogeneity and complex evolution of the faults (Figure 4.13). The displacement plots in Chapter 4 were used to assess the period of fault nucleation, reactivation and their interactions through time. The t-z profiles for the deep-seated faults can be grouped into three types; (a) those characterized by centrally located point of maximum displacement (d_{max}) and general decrease in gradient at their upper and lower tips e.g., F1, F2 and F5, (b) those profiles with a general upward increase in gradient increasing e.g., F3 and F4, and (c) a profile characterized by the two points of maximum displacement where the upper tip displayed a gradual decrease in fault throw. Except for faults F4 and F6, the other faults have their point of maximum displacement at horizon H5. If the point of nucleation coincides with the point of maximum displacement, then most of the deep-seated faults in the study area nucleated from H5. However, the points of maximum displacement can vary as a factor of mechanical heterogeneity, fault segmentation, and linkage. Similarly, the t-x plots also complex geometries such as C-type, M-type and multi-skewed C-type profiles (Figures 4.15 and 4.16). It is noted that the shape of the profiles is variable across horizons H4 to H6. Both throw plots show that the studied faults are characterized by both complex lateral and vertical segmentation.

Furthermore, analysis of the t-z profiles in terms of their mode of propagation revealed that the faults display multiple mode of propagation including radial propagation and syn-sedimentary activity. For example, Fault F1 shows evidence for syn-sedimentary activity from Horizon H4 to H6 while the rest of the profile shows blind propagation character. The lower part of faults F1, F2 and F5, and upper part of F4 have syn-sedimentary fault growth. Only faults F3 and F6 show that they developed solely through blind propagation of their tips as they are characterized by elliptical to sub-elliptical profiles with centrally located displacement maxima (Figure 4.14). In terms of their interaction with sedimentation, the growth and expansion indices show that the majority are syn- sedimentary at their upper most sections while some of them did not interact with a free surface during their growth (Figures 4.17 & 4.18). Majority of the faults have growth indices > 0.1 suggesting that strata growth on their hanging-wall

section exceeds the footwall section. For example, F1 shows a t-z profile with both syn-sedimentary and blind character. At horizons H4 to H6, where the faults propagated by syn-sedimentary activity, F1 was also formed coevally with sedimentation, but never exposed above any of the stratigraphic units during its growth. Hence, the majority of the deep-seated faults were formed by coalescence of initial isolated fault strands and were later reactivated. Evidence for reactivation is shown as displacement minima along some of the t-z profiles e.g., faults F1 and F4 (Figure 4.14). These points of dip linkage indicates that the upper and the lower segments of F1 and F4 have been linked by reactivation through dip linkage (Mansfield and Cartwright, 1996; Omosanya and Alves, 2014; Tvedt et al., 2013).

Fault reactivation by dip linkage was only inferred for the deep-seated faults. In the study area, the non-reactivated faults include: (1) the shallow minor faults extending down to the Paleocene Unit 8 (Kveite/Kviting Formations) and upwards above URU (Upper Regional Unconformity), localized faults in Upper Cretaceous (Unit 8), Paleocene (Unit 9a), and Eocene (Unit 9b) Formations, and (2) eroded faults terminated upward to Unit 5 (Figure 4.5). Since the oldest non-reactivated faults were found in Upper Cretaceous to younger formations, it is proposed that fault reactivation was dominant in pre-late Cretaceous times presumably at the end of Jurassic i.e. during Kimmeridgian extensional tectonics. Evidence for the Kimmeridgian tectonics is shown by faults F1 and F2 with significant change in their t-z profiles at horizon H6 (Late Jurassic). The obvious displacement minima or dip-linkage is noted at horizon H7 which is Lower Cretaceous. In addition, a minor evidence for fault reactivation during Paleocene times is shown by F1 at Horizon H9 which is the base of the Torsk Formation. Hence, three episodes of fault reactivation in late Jurassic, early Cretaceous and Early Paleocene times are proposed.

The minor faults are common above Unit 8 and are characterized by straight fault arrays, and are probably formed after the fault reactivation phases. Some of the minor faults intersected unit U9a and tip out upward to the topmost part of U9b and are dominantly antithetic to the major reactivated faults. The maximum throw of these faults is estimated on Horizon Ha i.e., the late Eocene Unconformity (Figure 4.2). Similarly, most of the reactivated faults penetrated upward from Unit 4 to Unit 9, hence their fault arrays are highly segmented (Figure 4.8Figure 4.8). As noted earlier, their maximum throw and displacement is recorded on H5. In the study area, the throw values of reactivated faults are greater than non-reactivated faults. Average throw values of 100 ms TWTT (100 m) were estimated for the reactivated faults. Reactivated

major faults in the study area are presumably formed by one of three modes: (a) by upward propagation of existing faults, (b) by dip-linkage, and (c) interaction and linkages along strike i.e, strike-linkage (Baudon and Cartwright, 2008; Omosanya and Alves, 2014; Tvedt et al., 2013; Jackson and Rotevatn, 2013). As the preferred direction of fault reactivation is directly related to the orientation of the fault plane relative to the principal stress direction, the strain causes reactivation, friction coefficients and cohesion, fault segmentation, maximum dimension and throw values (Sibson, 1985; Baudon and Cartwright, 2008; Richard and Krantz, 1991; White et al., 1986). The principal stress direction during the first fault reactivation at the end of Jurassic can be inferred as N-S from the E-W orientated faults and probably shifted towards ENE-WSW as indicated by NNW-SSE oriented major faults.

5.1.2 Implications of fault growth and reactivation for hydrocarbon migration

The timing of fault activity has direct application on hydrocarbon migration and sealing of faults (McClay, 1990). Knowing accurate time of fault reactivation phases would be an important factor for hydrocarbons spilling out of the structures which is critical for evaluation of seal risk and seal integrity (Gartrell et al., 2002; Hooper, 1991; Cartwright et al., 2007). In addition, understanding the complete phases of reactivation can provide insights on subsurface fluid-flow or hydrocarbon migration. Identifying reactivated and non-reactivated faults and their modes/mechanisms of linkage can bring better understanding about the possible migration pathways for hydrocarbon migration from the source-to-trap and leakage from trap-to-near subsurface and seabed/surface.

Different indicators have been examined to understand whether the faults are sealing or leaking. The first evidence is the spatial proximity of the major faults with the high-amplitude anomalies (HAAs). In Figure 4.29, it is shown that the majority of the HAAs are located on and are intersected by the major faults. The second evidence is the high throw values estimated for the major faults especially at the reservoir zone in which it was predicted that high fracturing has led to hydrocarbons migrating out of the reservoirs. These high throw or displacement values along the reservoir zone are not unrelated to the high degree of reactivation. The third evidence is the presence of gas chimneys that penetrated all the way upward from the Triassic (Snadd and Kobbe Formations) to the Paleocene to Eocene (Torsk) Formations. Pockmarks are useful to constrain the timing of episodes of fluid flow which can be traced on the seismic reflections (Judd and Hovland, 2007). The pattern and regular spacing of the pockmarks on the

seabed (Ligtenberg, 2005), and their spatially alignment vertically with the faults, provided insights on the timing of hydrocarbon leakage and migration pathways. Seabed pockmarks in the study area are lined up with the upper tips of the Paleocene-Eocene small faults and these faults are linked downward to the HAAs. This indicates these faults were the conduits for fluids from the shallow fluid accumulations, HAAs, to the seabed.

As for fault reactivation, the multiple drags interpreted on Unit 5 show that the fault zones are probably highly fractured. Fault reactivation can mechanically fracture and brecciate fault zones creating secondary porosity and can also spill hydrocarbons out of the reservoir. Since the HAAs are affected and juxtaposed by the small faults, it implies that the fluid accumulations have migrated to their current stratigraphic position before the onset of the Paleocene-Eocene faulting phase. Based on this, the last episode of fluid migration from the source rock to the shallow subsurface accumulation is before the onset of Paleocene-Eocene faulting. Furthermore, the shallow fluid accumulations are not also affected by the late Cretaceous faults as observed as observed seismic sections and RMS amplitude time slices. This suggests the first phase of fluid migration was probably during the late Jurassic. It is recalled that this corresponds to the Kimmeridgian tectonics and the first episode of fault reactivation. The second and third phases of fluid migration could be follow the late Cretaceous and Paleocene fault reactivations. However, it is hard to constrain the amount of fluid migrated during each of the phases. The degree of fault reactivation during late Cretaceous is relatively less, which in turn implies that the amount of fluid leaked or migrated during this period is less relative to late Jurassic and Paleocene times. Pockmarks and furrows on the URU and seabed would are evidence that fluid-flow was active during the early stages of glaciation and is an ongoing process in the study area (Løseth et al., 2009). Hence, a phase of fluid migration may have taken place shortly after the last glacial maximum as documented by the large number of buried pockmarks on the URU (see the works of Ostanin et al., 2012a, 2012b, 2013).

5.1.3 Source of fluids, types and their migration pathways

The nine high-amplitude anomalies in this work have reversed or opposite polarities, negative high amplitudes, and can be further classified based on their conformability with their background structural reflectors. The first groups of anomalies are structurally conformable and are aligned in the same direction to the background reflectors, e.g., A4, A5 and A9. Based on their flatness, these are difficult to interpret as flat spots especially when the seismic volume

is interpreted in the time domain. Alternatively, their flat geometry may imply they are static fluid accumulations. In addition, this group of anomalies is not spatially related to the major faults and is controlled largely by the stratigraphic or geomorphic structures. A4 and A5 are hosted in Unit 8 while A9 is hosted in Unit 4. The second group of anomalies (A1, A2, A3, A6, A7 and A8) are structurally unconformable to the background reflectors and are also interpreted as fluid accumulations. They are hosted in Unit 9 and spatially located on the upper parts of the major faults. Apart from the high-amplitude anomalies, fluid flow features interpreted in the study area include iceberg plough marks, pockmarks and gas chimneys.

The source area for fluids or hydrocarbons in the study area includes; (a) Triassic formations, since the gas chimneys extend from Unit 4 upward to Eocene Unit 9, and (b) Jurassic intervals through which the deep-seated faults intersected (Figure 5.1). The variance and chaos attributes indicate that the major gas chimneys in the southwestern and northeastern part of the field originated from the Triassic source and reservoir rocks. The areal extent of acoustic masking increases upward from the reservoir zone indicating that more hydrocarbons were leaked from the reservoir through the chimneys. Faults can act as fluid-flow barriers or conduits depending on the nature of the fault. The fault zone can be brecciated and fractured to enhance porosity, permeability, and fluid migration pathways. On the other hand, fault-related diagenesis, clay smearing can block the permeability of the fault zone in which case it will act as a subsurface fluid-flow barrier. Since most of the anomalies are located on the hanging-wall side of the deep-seated faults and for the fact that, the throws estimated along most of the faults are more than 30 ms (30 m), it is hypothesized that faults are conduits for the hydrocarbon-related anomalies. Although no fault seal analysis was done in this work, the degree of fault juxtaposition across the faults provided proof for fluid leakage and transmission through the faults. Hence, the mechanism of fluid leakage is through tectonic fracturing. At shallow levels or during the proposed fourth episode of fluid migration, hydro-fracturing is thought to be enhanced by uplift and erosion. These are main mechanisms driving fluid migration during the glaciation periods.
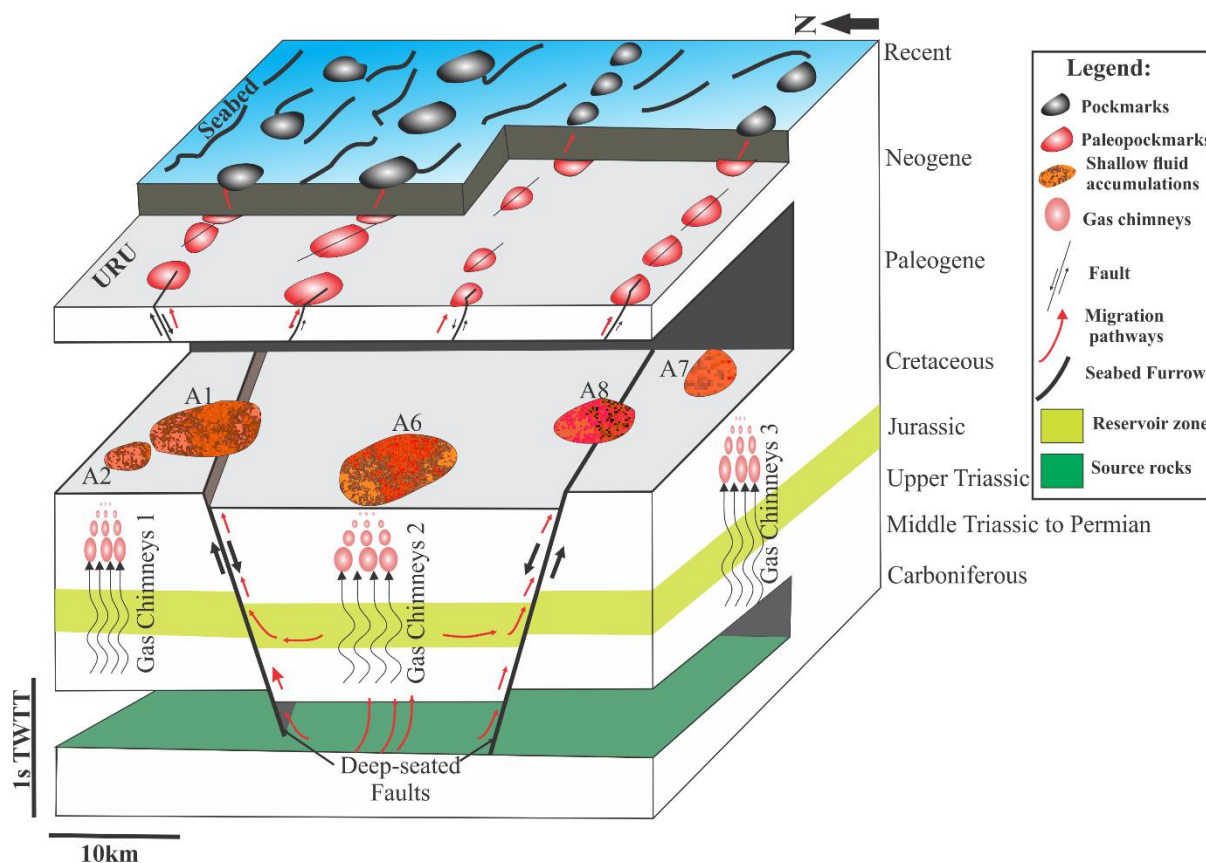
Figure 5.1 Conceptual diagram illustrating the hydrocarbon plumbing system in the study area, the spatial relationship between the deep-seated faults, shallow fluid accumulations and fluid-flow features like pockmarks. The red dashed arrow indicates the migration pathways from the source to the shallow fluid accumulations. The smaller faults start approximately at the depth of shallow fluid accumulations and line-up upward with pockmarks on the seabed. Most of these faults are antithetic to the major faults. *N.B: URU is the Upper Regional Unconformity.*

In addition to tectonic stress and intense faulting, sea level fluctuations and depositional loading/unloading caused by differential and disequilibrium compaction and erosion related to: uplift (Jolly and Lonergan, 2002); lateral pressure transfer during fault interaction and reactivation (Andresen et al., 2009); overpressure caused by influx of fluids from the source and the reservoir (Huuse et al., 2010; Osborne and Swarbrick, 1997); tilting of the reservoir; diagenetic transformations (Davies et al., 2008, 2006); and seal failure are other mechanisms that could enhance hydrocarbon migration and plumbing systems in the study area. Migration is possible through vertical transmission of fluid through the faults and laterally along the margins of the gas chimneys (Figure 5.1).

5.2 Conclusions

- Six major deep-seated faults extending from Upper Carboniferous to Eocene have been linked with hydrocarbon migration from the reservoir rocks in the Snøhvit Field, Hammerfest Basin. These faults have their maximum throw values at the reservoir interval and have possible been reactivated during late Jurassic (Kimmeridgian) tectonic activity.

- Throw and displacement profiles of the major faults in the study area show that the faults have a polycyclic fault history involving both blind propagation and syn-sedimentary activity.

- The faults are characterized by complex lateral and vertical segmentation or linkage. Most of the major faults interacted and linked along the strike direction having multi-skewed C-type profiles. Fault reactivation was dominantly through dip-linkage.

- The expansion indices of the deep-seated major faults are consistent with displacement analysis and show thickening along the hanging-wall side on Unit 5 which is the reservoir zone. The growth indices signified the major faults are interacted with the free surface, except F6, which is a blind fault.

- Three phases of fault reactivation in Late Jurassic, Early Cretaceous and Paleocene-early Eocene predated fluid migration in the study area. Migration of hydrocarbons took place after each phase of fault reactivation since the source rocks were mature before the fault reactivation.

- Nine high-amplitude anomalies related to hydrocarbon are mapped and analyzed using multiple seismic attribute. Of these anomalies, six of them are structurally unconformable and interpreted as fluid accumulations. The fluid accumulations are spatially located in the upper parts of the major faults (A2, A3, A7 and A8) and on the top of gas chimneys (A1 and A6). Structurally conformable HAAs (A4, A5 and A9) are stratigraphically controlled and have no spatial relationship with the major deep-seated faults.

- The major deep-seated faults are the main hydrocarbon migration pathways from the Triassic source rocks and the Jurassic reservoirs; further leakage to the seabed was through the smaller Paleocene to Early Eocene faults.

- The main driving and trigger mechanisms for fluid-flow in the study area are tectonic fracturing and/or hydro-fracturing. Fluids or hydrocarbons migrated laterally and vertically from Jurassic and Triassic units into shallow levels. Fluid-flow is an active process in the Snøhvit Field as evidenced by the presence of present-day seabed pockmarks and furrows.

5.3 Recommendations

High-quality seismic data is needed for better stratigraphic interpretations, fault analysis and migration pathway detection. Specifically reconstructing the phases of fault reactivation and periods of fluid migration are difficult. Further work on fault seal analysis is needed to fully understand the migration pathways identified from multi-seismic attribute analysis. Basin modelling, rock physics and AVO analysis are recommended to identify the fluid types and history of hydrocarbon generation and maturation.

References

Alves, T.M., Omosanya, K., Gowling, P., 2015. Volume rendering of enigmatic high-amplitude anomalies in southeast Brazil: A workflow to distinguish lithologic features from fluid accumulations. Interpretation 3, A1–A14.

Andreassen, K., Laberg, J.S., Vorren, T.O., 2008. Seafloor geomorphology of the SW Barents Sea and its glaci-dynamic implications. Geomorphology 97, 157–177.

Andresen, K.J., 2012. Fluid flow features in hydrocarbon plumbing systems: What do they tell us about the basin evolution? Mar. Geol. 332, 89–108.

Andresen, K.J., Clausen, O.R., Huuse, M., 2009. A giant (5.3× 10 7 m 3) middle Miocene (c. 15Ma) sediment mound (M1) above the Siri Canyon, Norwegian–Danish Basin: Origin and significance. Mar. Pet. Geol. 26, 1640–1655.

Andresen, K.J., Huuse, M., 2011. "Bulls-eye"pockmarks and polygonal faulting in the Lower Congo Basin: relative timing and implications for fluid expulsion during shallow burial. Mar. Geol. 279, 111–127.

Arntsen, B., Wensaas, L., Løseth, H., Hermanrud, C., 2007. Seismic modeling of gas chimneys. Geophysics 72, SM251–SM259.

Barnett, J.A.M., Mortimer, J., Rippon, J.H., Walsh, J.J., Watterson, J., 1987. Displacement geometry in the volume containing a single normal fault. Am. Assoc. Pet. Geol. Bull. 71, 925–937.

Barrère, C., Ebbing, J., Gernigon, L., 2009. Offshore prolongation of Caledonian structures and basement characterisation in the western Barents Sea from geophysical modelling. Tectonophysics 470, 71–88.

Baudon, C., Cartwright, J., 2008a. The kinematics of reactivation of normal faults using high resolution throw mapping. J. Struct. Geol. 30, 1072–1084.

Baudon, C., Cartwright, J., 2008b. Early stage evolution of growth faults: 3D seismic insights from the Levant Basin, Eastern Mediterranean. J. Struct. Geol. 30, 888–898.

Beach, A., 1984. Structural evolution of the Witch Ground Graben. J. Geol. Soc. London. 141, 621–628.

Bellahsen, N., Daniel, J.M., 2005. Fault reactivation control on normal fault growth: an experimental study. J. Struct. Geol. 27, 769–780.

Berglund, L.T., Augustson, J., Færseth, R., Gjelberg, J., Ramberg-Moe, H., 1986. The evolution of the Hammerfest Basin. Habitat Hydrocarb. Nor. Cont. shelf 319–338.

Berndt, C., 2005. Focused fluid flow in passive continental margins. Philos. Trans. R. Soc. London A Math. Phys. Eng. Sci. 363, 2855–2871.

Bischke, R.E., 1994. Interpreting Sedimentary Growth Structures from Well Log and Seismic Data (With Examples). Am. Assoc. Pet. Geol. Bull. 78, 873–892.

Breivik, A.J., Faleide, J.I., Gudlaugsson, S.T., 1998. Southwestern Barents Sea margin: late Mesozoic sedimentary basins and crustal extension. Tectonophysics 293, 21–44.

Breivik, A.J., Mjelde, R., Grogan, P., Shimamura, H., Murai, Y., Nishimura, Y., 2005. Caledonide development offshore–onshore Svalbard based on ocean bottom seismometer, conventional seismic, and potential field data. Tectonophysics 401, 79–117.

Breivik, A.J., Mjelde, R., Grogan, P., Shimamura, H., Murai, Y., Nishimura, Y., Kuwano, A., 2002. A possible Caledonide arm through the Barents Sea imaged by OBS data. Tectonophysics 355, 67–97.

Brown, A.R., 2004. Interpretation of three-dimensional seismic data. AAPG Memoir 42,, SEG Investigation in Geopysics.

Brown, A.R., 2008. Phase and Polarity Issues in Modern Seismic Interpretation. In: AAPG International Conference and Exhibition. AAPG, Cape Town, pp. 1–22.

Calvès, G., Huuse, M., Schwab, A., Clift, P., 2008. Three-dimensional seismic analysis of high-amplitude anomalies in the shallow subsurface of the Northern Indus Fan: Sedimentary and/or fluid origin. J. Geophys. Res. 113, B11103.

Cartwright, J., Bouroullec, R., James, D., Johnson, H., 1998. Polycyclic motion history of some Gulf Coast growth faults from high-resolution displacement analysis. Geology 26, 819–822.

Cartwright, J., Huuse, M., Aplin, A., 2007. Seal bypass systems. Am. Assoc. Pet. Geol. Bull. 91, 1141–1166.

Cathles, L.M., Su, Z., Chen, D., 2010. The physics of gas chimney and pockmark formation, with implications for assessment of seafloor hazards and gas sequestration. Mar. Pet. Geol. 27, 82–91.

Cavanagh, A.J., Di Primio, R., Scheck-Wenderoth, M., Horsfield, B., 2006. Severity and timing of Cenozoic exhumation in the southwestern Barents Sea. J. Geol. Soc. London. 163, 761–774.

Chand, S., Knies, J., Baranwal, S., Jensen, H., Klug, M., 2014. Structural and stratigraphic controls on subsurface fluid flow at the Veslemøy High, SW Barents Sea. Mar. Pet. Geol. 57, 494–508.

Chand, S., Mienert, J., Andreassen, K., Knies, J., Plassen, L., Fotland, B., 2008. Gas hydrate stability zone modelling in areas of salt tectonics and pockmarks of the Barents Sea suggests an active hydrocarbon venting system. Mar. Pet. Geol. 25, 625–636.

Chand, S., Thorsnes, T., Rise, L., Brunstad, H., Stoddart, D., Bøe, R., Lågstad, P., Svolsbru, T., 2012. Multiple episodes of fluid flow in the SW Barents Sea (Loppa High) evidenced by gas flares, pockmarks and gas hydrate accumulation. Earth Planet. Sci. Lett. 331–332, 305–314.

Childs, C., Nicol, A., Walsh, J.J., Watterson, J., 2003. The growth and propagation of synsedimentary faults. J. Struct. Geol. 25, 633–648.

Dalland, A., Worsley, D., Ofstad, K. (eds.)., 1988. A lithostratigraphic scheme for the Mesozoic and Cenozoic succession offshore mid- and northern Norway. NPD-Bulletin, No. 4 65.

Davies, R.J., Brumm, M., Manga, M., Rubiandini, R., Swarbrick, R., Tingay, M., 2008. The East Java mud volcano (2006 to present): An earthquake or drilling trigger? Earth Planet. Sci. Lett. 272, 627–638.

Davies, R.J., Huuse, M., Hirst, P., Cartwright, J., Yang, Y., 2006. Giant clastic intrusions primed by silica diagenesis. Geology 34, 917–920.

Dimakis, P., Braathen, B.I., Faleide, J.I., Elverhøi, A., Gudlaugsson, S.T., 1998. Cenozoic erosion and the preglacial uplift of the Svalbard–Barents Sea region. Tectonophysics 300, 311–327.

Doré, A.G., Jensen, L.N., 1996. The impact of late Cenozoic uplift and erosion on hydrocarbon exploration: offshore Norway and some other uplifted basins. Glob. Planet. Change 12, 415–436.

Dörr, N., Lisker, F., Clift, P.D., Carter, A., Gee, D.G., Tebenkov, A.M., Spiegel, C., 2012. Late Mesozoic–Cenozoic exhumation history of northern Svalbard and its regional significance: Constraints from apatite fission track analysis. Tectonophysics 514, 81–92.

Dugan, B., Flemings, P.B., 2000. Overpressure and fluid flow in the New Jersey continental slope: implications for slope failure and cold seeps. Science (80-.). 289, 288–291.

Dupré, S., Woodside, J., Klaucke, I., Mascle, J., Foucher, J.-P., 2010. Widespread active seepage activity on the Nile Deep Sea Fan (offshore Egypt) revealed by high-definition geophysical imagery. Mar. Geol. 275, 1–19.

Elverhøi, A., Solheim, A., 1983. The Barents Sea ice sheet-a sedimentological discussion. Pol. Res. 23-42.

Faleide, J.I., Gudlaugsson, S.T., Jacquart, G., 1984. Evolution of the western Barents Sea. Mar. Pet. Geol. 1, 123–150.

Faleide, J.I., Solheim, A., Fiedler, A., Hjelstuen, B.O., Andersen, E.S., Vanneste, K., 1996. Late Cenozoic evolution of the western Barents Sea-Svalbard continental margin. Glob. Planet. Change 12, 53–74.

Faleide, J.I., Tsikalas, F., Breivik, A.J., Mjelde, R., Ritzmann, O., Engen, O., Wilson, J., Eldholm, O., 2008. Structure and evolution of the continental margin off Norway and the Barents Sea. Episodes 31, 82.

Faleide, J.I., Vågnes, E., Gudlaugsson, S.T., 1993. Late Mesozoic-Cenozoic evolution of the south-western Barents Sea in a regional rift-shear tectonic setting. Mar. Pet. Geol. 10, 186–214.

Fossen, H., 2010. Structural geology. Cambridge University Press.

Gabrielsen, R.H., Færseth, R.B., Jensen, L.N., Kalheim, J.E., Riis, F., 1990. Structural elements of the Norwegian Continental Shelf. Part 1: The Barents Sea region. NPD-Bulletin, No. 6 33 PP.

Gartrell, A., Lisk, M., Underschultz, J., 2002. Controls on the trap integrity of the Skua oil field, Timor Sea. In: The Sedimentary Basins of Western Australia 3: Proceedings of the Petroleum Exploration Society of Australia Symposium, Perth. 389-407. pp. 389–407.

Gawthorpe, R.L., Leeder, M.R., 2000. Tectono-sedimentary evolution of active extensional basins. Basin Res. 12, 195–218.

Gay, A., Takano, Y., Gilhooly Iii, W.P., Berndt, C., Heeschen, K., Suzuki, N., Saegusa, S., Nakagawa, F., Tsunogai, U., Jiang, S.Y., 2011. Geophysical and geochemical evidence of large scale fluid flow within shallow sediments in the eastern Gulf of Mexico, offshore Louisiana. Geofluids 11, 34–47.

Gee, D.G., Fossen, H., Henriksen, N., Higgins, A.K., 2008. From the early Paleozoic platforms of Baltica and Laurentia to the Caledonide Orogen of Scandinavia and Greenland. Episodes 31, 44.

Gernigon, L., Brönner, M., 2012. Late Palaeozoic architecture and evolution of the southwestern Barents Sea: insights from a new generation of aeromagnetic data. J. Geol. Soc. London. 169, 449–459.

Gernigon, L., Brönner, M., Roberts, D., Olesen, O., Nasuti, A., Yamasaki, T., 2014. Crustal and basin evolution of the southwestern Barents Sea: from Caledonian orogeny to continental breakup. Tectonics 33, 347–373.

Gibbs, A.D., 1983. Balanced cross-section construction from seismic sections in areas of extensional tectonics. J. Struct. Geol. 5, 153–160.

Glørstad-Clark, E., Faleide, J.I., Lundschien, B.A., Nystuen, J.P., 2010. Triassic seismic sequence stratigraphy and paleogeography of the western Barents Sea area. Mar. Pet. Geol. 27, 1448–1475.

Green, P.F., Duddy, I.R., 2010. Synchronous exhumation events around the Arctic including examples from Barents Sea and Alaska North Slope. Geol. Soc. London, Pet. Geol. Conf. Ser. 7, 633–644.

Gudlaugsson, S.T., Faleide, J.I., Johansen, S.E., Breivik, A.J., 1998. Late Palaeozoic structural development of the south-western Barents Sea. Mar. Pet. Geol. 15, 73–102.

Heggland, R., 1998. Gas seepage as an indicator of deeper prospective reservoirs. A study based on exploration 3D seismic data. Mar. Pet. Geol. 15, 1–9.

Heggland, R., Meldahl, P., Bril, B., de Groot, P., 1999. The chimney cube, an example of semi-automated detection of seismic objects by directive attributes neural networks: Part II; Interpretation. 69th SEG Conf.

Henriksen, E., Bjørnseth, H.M., Hals, T.K., Heide, T., Kiryukhina, T., Kløvjan, O.S., Larssen, G.B., Ryseth, A.E., Rønning, K., Sollid, K., 2011. Uplift and erosion of the greater Barents

Sea: impact on prospectivity and petroleum systems. Geol. Soc. London, Mem. 35, 271–281.

Hongxing, G., Anderson, J.K., 2007. Fault throw profile and kinematics of normal fault: conceptual models and geologic examples. Geol. J. China Univ 13, 75–88.

Hooper, E.C.D., 1991. Fluid migration along growth faults in compacting sediments. J. Pet. Geol. 14, 161–180.

Hovland, M., Judd, A.G., 1988. Seabed pockmarks and seepages: impact on geology, biology and the marine environment.

Hustoft, S., Bünz, S., Mienert, J., 2010. Three-dimensional seismic analysis of the morphology and spatial distribution of chimneys beneath the Nyegga pockmark field, offshore mid-Norway. Basin Res. 22, 465–480.

Huuse, M., Jackson, C.A., Van Rensbergen, P., Davies, R.J., Flemings, P.B., Dixon, R.J., 2010. Subsurface sediment remobilization and fluid flow in sedimentary basins: an overview. Basin Res. 22, 342–360.

Jackson, C.A.L., Rotevatn, A., 2013. 3D seismic analysis of the structure and evolution of a salt-influenced normal fault zone: A test of competing fault growth models. J. Struct. Geol. 54, 215–234.

Johansen, S.E., Ostisty, B.K., Birkeland, Ø., Fedorovsky, Y.F., Martirosjan, V.N., Christensen, O.B., Cheredeev, S.I., Ignatenko, E.A., Margulis, L.S., 1992. Hydrocarbon potential in the Barents Sea region: play distribution and potential. Arct. Geol. Pet. Potential, Nor. Pet. Soc. (NPF), Spec. Publ. 2, 273–320.

Jolly, R.J.H., Lonergan, L., 2002. Mechanisms and controls on the formation of sand intrusions. J. Geol. Soc. London. 159, 605–617.

Josenhans, H.W., King, L.H., Fader, G.B., 1978. A side-scan sonar mosaic of pockmarks on the Scotian Shelf. Can. J. Earth Sci. 15, 831–840.

Judd, A., Hovland, M., 2007. Seabed fluid flow: the impact on geology, biology and the marine environment. Cambridge University Press.

Kim, Y.-S., Sanderson, D.J., 2005. The relationship between displacement and length of faults: a review. Earth-Science Rev. 68, 317–334.

Klitzke, P., Faleide, J.I., Scheck-Wenderoth, M., Sippel, J., 2014. A lithosphere-scale structural model of the Barents Sea and Kara Sea region. Solid Earth Discuss. 6, 1579–1624.

Knies, J., Matthiessen, J., Vogt, C., Laberg, J.S., Hjelstuen, B.O., Smelror, M., Larsen, E., Andreassen, K., Eidvin, T., Vorren, T.O., 2009. The Plio-Pleistocene glaciation of the Barents Sea–Svalbard region: a new model based on revised chronostratigraphy. Quat. Sci. Rev. 28, 812–829.

Knutsen, S.-M., Vorren, T.O., 1991. Early Cenozoic sedimentation in the Hammerfest Basin. Mar. Geol. 101, 31–48.

Laberg, J.S., Andreassen, K., Knutsen, S.-M., 1998. Inferred gas hydrate on the Barents Sea shelf—a model for its formation and a volume estimate. Geo-Marine Lett. 18, 26–33.

Ligtenberg, J.H., 2005. Detection of fluid migration pathways in seismic data: implications for fault seal analysis. Basin Res. 17, 141–153.

Linjordet, A., Olsen, G.R., 1992. The jurassic Snøhvit gas field, Hammerfest Basin, offshore northern Norway. Giant oil and gas fields Decad. 1988, 349–370.

Løseth, H., Gading, M., Wensaas, L., 2009. Hydrocarbon leakage interpreted on seismic data. Mar. Pet. Geol. 26, 1304–1319.

Løseth, H., Wensaas, L., Arntsen, B., Hanken, N., Basire, C., Graue, K., 2001. 1000 m long gas blow-out pipes. In: 63rd EAGE Conference & Exhibition.

Løseth, H., Wensaas, L., Arntsen, B., Hanken, N.-M., Basire, C., Graue, K., 2011. 1000 m long gas blow-out pipes. Mar. Pet. Geol. 28, 1047–1060.

Mansfield, C.S., Cartwright, J.A., 1996. High resolution fault displacement mapping from three-dimensional seismic data: evidence for dip linkage during fault growth. J. Struct. Geol. 18, 249–263.

Marello, L., Ebbing, J., Gernigon, L., 2013. Basement inhomogeneities and crustal setting in the Barents Sea from a combined 3D gravity and magnetic model. Geophys. J. Int. 1–28.

McClay, K.R., 1990. Extensional fault systems in sedimentary basins: a review of analogue model studies. Mar. Pet. Geol. 7, 206–233.

Mienert, J., Vanneste, M., Bünz, S., Andreassen, K., Haflidason, H., Sejrup, H.P., 2005. Ocean warming and gas hydrate stability on the mid-Norwegian margin at the Storegga Slide. Mar. Pet. Geol. 22, 233–244.

Moss, J.L., Cartwright, J., 2010. 3D seismic expression of km-scale fluid escape pipes from offshore Namibia. Basin Res. 22, 481–501.

Muraoka, H., Kamata, H., 1983. Displacement distribution along minor fault traces. J. Struct. Geol. 5, 483–495.

Nickel, J.C., di Primio, R., Mangelsdorf, K., Stoddart, D., Kallmeyer, J., 2012. Characterization of microbial activity in pockmark fields of the SW-Barents Sea. Mar. Geol. 332, 152–162.

NPD, N.P.D., 2015. Wellbore information. URL http://factpages.npd.no/factpages/ (accessed 01.01.2015).

Ohm, S.E., Karlsen, D.A., Austin, T.J.F., 2008. Geochemically driven exploration models in uplifted areas: Examples from the Norwegian Barents Sea. Am. Assoc. Pet. Geol. Bull. 92, 1191–1223.

Omosanya, K.O., Alves, T.M., 2014. Mass-transport deposits controlling fault propagation, reactivation and structural decoupling on continental margins (Espírito Santo Basin, SE Brazil). Tectonophysics 628, 158–171.

Osborne, M.J., Swarbrick, R.E., 1997. Mechanisms for generating overpressure in sedimentary basins: a reevaluation. Am. Assoc. Pet. Geol. Bull. 81, 1023–1041.

Ostanin, I., Anka, Z., di Primio, R., Bernal, A., 2012a. Identification of a large Upper Cretaceous polygonal fault network in the Hammerfest Basin: Implications on the reactivation of regional faulting and gas leakage dynamics, SW Barents Sea. Mar. Geol. 332, 109–125.

Ostanin, I., Anka, Z., Di Primio, R., Bernal, A., 2012b. Hydrocarbon leakage above the Snøhvit gas field, Hammerfest Basin SW Barents Sea. first Break 30.

Ostanin, I., Anka, Z., di Primio, R., Bernal, A., 2013. Hydrocarbon plumbing systems above the Snøhvit gas field: structural control and implications for thermogenic methane leakage in the Hammerfest Basin, SW Barents Sea. Mar. Pet. Geol. 43, 127–146.

Ottesen, S., Folkestad, A., Gawthorpe, R., 2005. Tectono-stratigraphic development of the Hammerfest Basin (Northern Norway) during the Jurassic to Cretaceous. AAPG Annual Meeting. abstruct volume .

Pilcher, R., Argent, J., 2007. Mega-pockmarks and linear pockmark trains on the West African continental margin. Mar. Geol. 244, 15–32.

Pochat, S., Castelltort, S., Choblet, G., Van Den Driessche, J., 2009. High-resolution record of tectonic and sedimentary processes in growth strata. Mar. Pet. Geol. 26, 1350–1364.

Reeve, M.T., Bell, R.E., Duffy, O.B., Jackson, C.A.L., Sansom, E., 2015. The growth of non-colinear normal fault systems; What can we learn from 3D seismic reflection data? J. Struct. Geol. 70, 141–155.

Richard, P., Krantz, R.W., 1991. Experiments on fault reactivation in strike-slip mode. Tectonophysics 188, 117–131.

Ritzmann, O., Faleide, J.I., 2007. Caledonian basement of the western Barents Sea. Tectonics 26.

Roberts, D., 2003. The Scandinavian Caledonides: event chronology, palaeogeographic settings and likely modern analogues. Tectonophysics 365, 283–299.

Rodrigues Duran, E., di Primio, R., Anka, Z., Stoddart, D., Horsfield, B., 2013. 3D-basin modelling of the Hammerfest Basin (southwestern Barents Sea): A quantitative assessment of petroleum generation, migration and leakage. Mar. Pet. Geol. 45, 281–303.

Rønnevik, H., Jacobsen, H.-P., 1984. Structural highs and basins in the western Barents Sea. Pet. Geol. North Eur. Margin 19–32.

Ryseth, A., Augustson, J.H., Charnock, M., Haugerud, O., Knutsen, S.M., Midbøe, P.S., Opsal, J.G., Sundsbø, G., 2003. Cenozoic stratigraphy and evolution of the Sørvestsnaget Basin, southwestern Barents Sea. Nor. Geol. Tidsskr. 83, 107–130.

Sheriff, R.E., Geldart, L.P., 1995. Exploration seismology. Cambridge university press.

Sibson, R.H., 1985. A note on fault reactivation. J. Struct. Geol. 7, 751–754.

Solheim, A., Elverhøi, A., 1985. A pockmark field in the Central Barents Sea; gas from a petrogenic source? Polar Res. 3, 11–19.

Thorsen, C.E., 1963. Age of Growth Faulting in Southeast Louisiana . Gulf Coast Assoc. Geol. Soc. Trans. 13, 103–110.

Tvedt, A.B.M., Rotevatn, A., Jackson, C.A.L., Fossen, H., Gawthorpe, R.L., 2013. Growth of normal faults in multilayer sequences: A 3D seismic case study from the Egersund Basin, Norwegian North Sea. J. Struct. Geol. 55, 1–20.

Vadakkepuliyambatta, S., Bünz, S., Mienert, J., Chand, S., 2013. Distribution of subsurface fluid-flow systems in the SW Barents Sea. Mar. Pet. Geol. 43, 208–221.

Vorren, T.O., Richardsen, G., Knutsen, S.-M., Henriksen, E., 1991. Cenozoic erosion and sedimentation in the western Barents Sea. Mar. Pet. Geol. 8, 317–340.

Walsh, J.J., Nicol, A., Childs, C., 2002. An alternative model for the growth of faults. J. Struct. Geol. 24, 1669–1675.

Walsh, J.J., Watterson, J., 1989. Displacement gradients on fault surfaces. J. Struct. Geol. 11, 307–316.

Watterson, J., 1986. Fault dimensions, displacements and growth. Pure Appl. Geophys. 124, 365–373.

White, S.H., Bretan, P.G., Rutter, E.H., 1986. Fault-Zone Reactivation: Kinematics and Mechanisms 317, 81–97.

Yilmaz, O., Doherty, S.M., 1987. Seismic Data Processing, Society of Exploration Geophysicists, Tulsa, OK.

Appendix

Appendix Table A1 The attitudes of interpreted faults

Fault	Strike	Dip	dip direction	Fault	Strike	Dip	dip direction
F1	75	62	161	F32	80	65	210
F2	78	57	110	F33	37	50	286
F3	73	62	345	F34	56	78	273
F4	50	63	100	F35	69	41	138
F5	77	66	310	F36	48	59	294
F6	82	59	345	F37	52	50	120
F7	77	49	351	F38	75	50	200
F8	62	51	127	F39	57	43	299
F9	78	70	166	F40	60	41	136
F10	85	53	347	F41	60	50	326
F11	88	69	10	F42	179	48	130
F12	76	54	344	F43	4	69	137
F13	71	53	5	F44	27	59	306
F14	81	40	337	F45	10	60	159
F15	56	69	205	F46	176	44	230
F16	126	67	287	F47	2	62	236
F17	46	71	354	F48	130	64	359
F18	47	75	320	F49	170	45	255
F19	40	70	345	F50	167	44	241
F20	39	41	22	F51	167	47	251
F21	78	50	196	F52	164	44	242
F22	70	53	160	F53	78	33	6
F23	80	40	150	F54	80	31	25
F24	77	46	142	F55	61	39	5
F25	96	51	204	F56	71	42	310
F26	92	53	174	F57	65	40	160
F27	85	27	346	F58	67	37	159
F28	84	61	192	F59	56	38	151
F29	74	38	344	F60	55	38	125
F30	70	48	163	F61	68	41	320
F31	63	56	320	F62	71	38	168
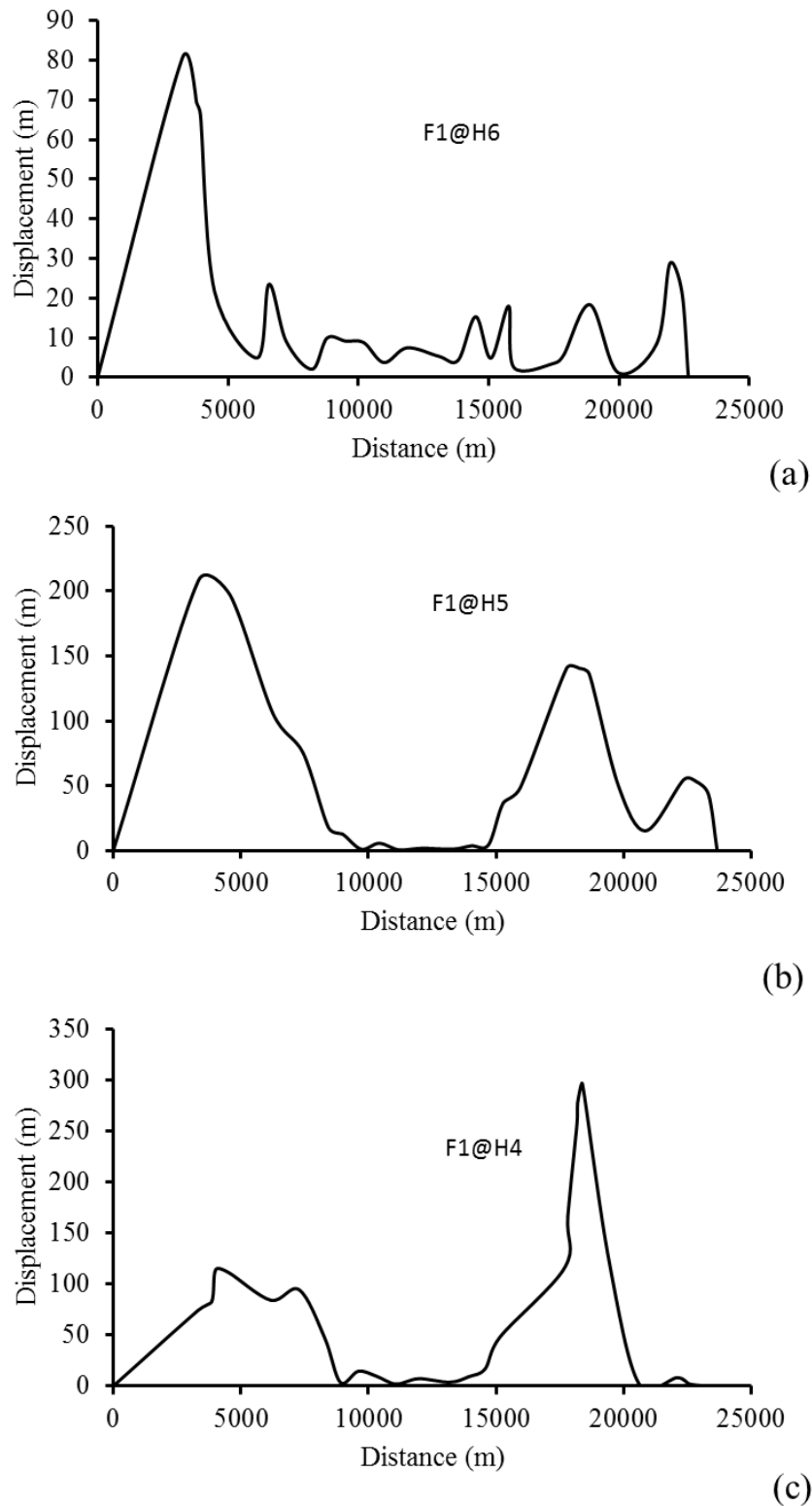
Figure A1 Distance-displacement (t-x) plots of F1 along H6 (a), H5 (b) and H4 (c).The displacement is higher at shorter distance for H6 and H5 and for H8 at larger distances, and the displacement along H6 is less than along H5 and H4. The profiles are in general multi-skewed C-type profiles.
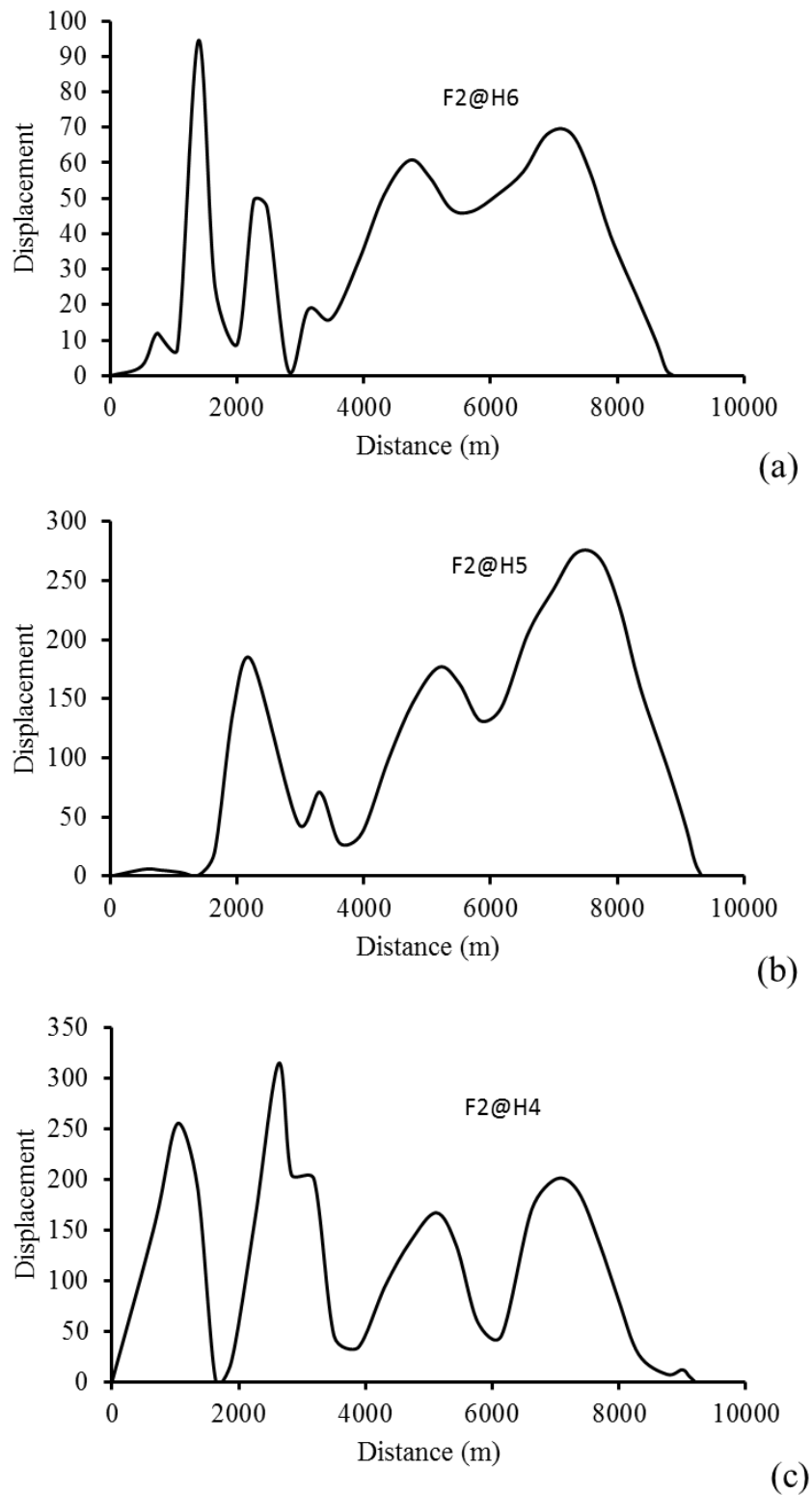
Figure A2 The general trend of distance-displacement (t-x) plot of F2 along H6 (a), H5 (b) and H4 (c).The profiles are in general multi-C-type profiles.
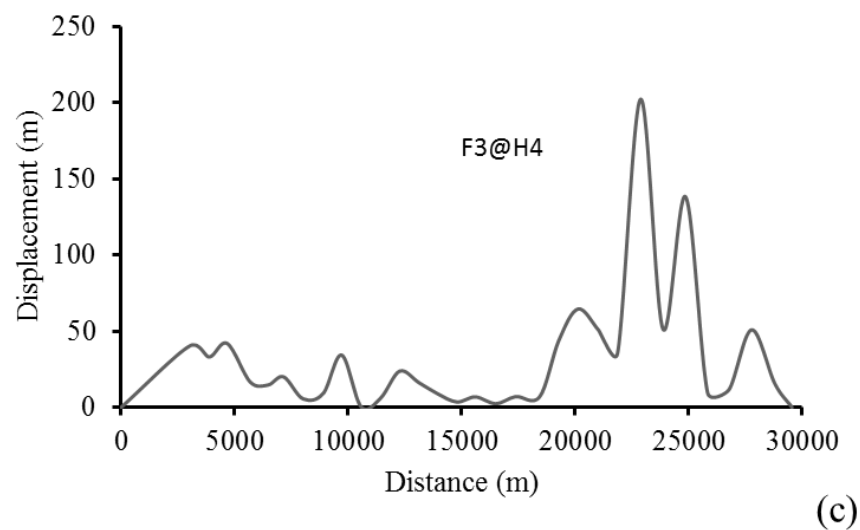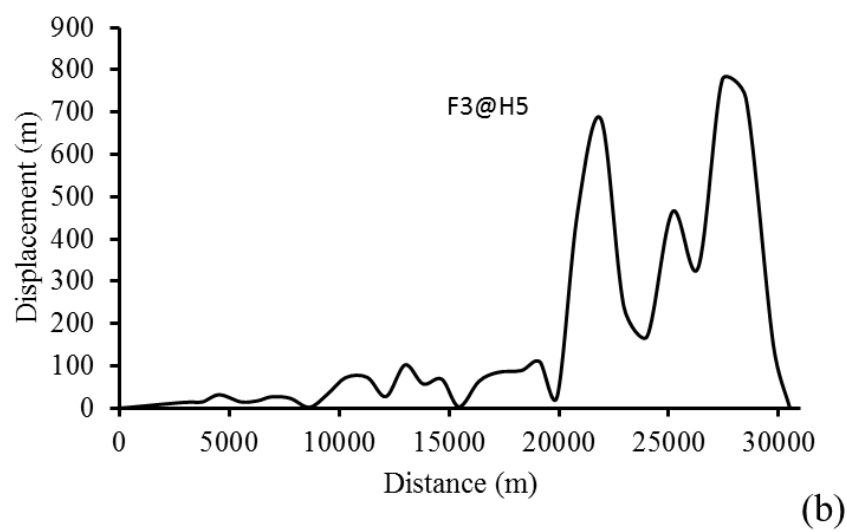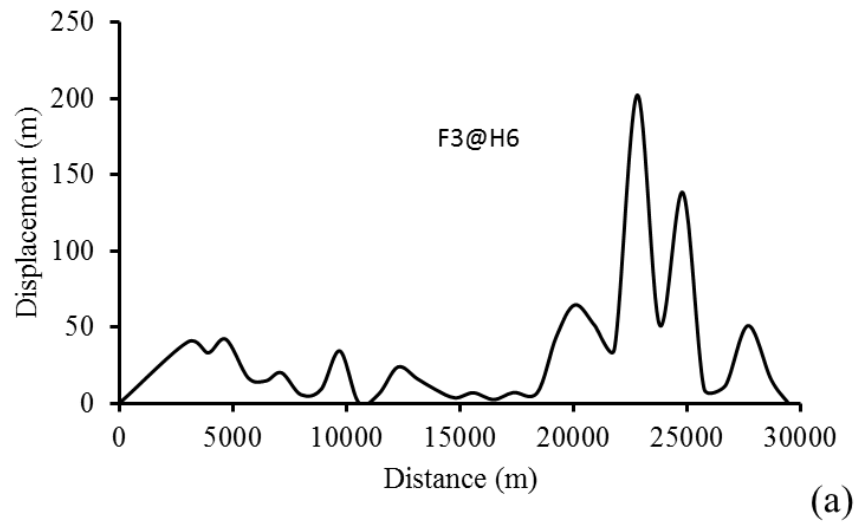
Figure A3 The distance-displacement (t-x) plots of F3 along (a) H6, (b) H5 and (c) H4; showing a general increase in displacement at larger distances. The profiles are in general multi-C-type profiles.
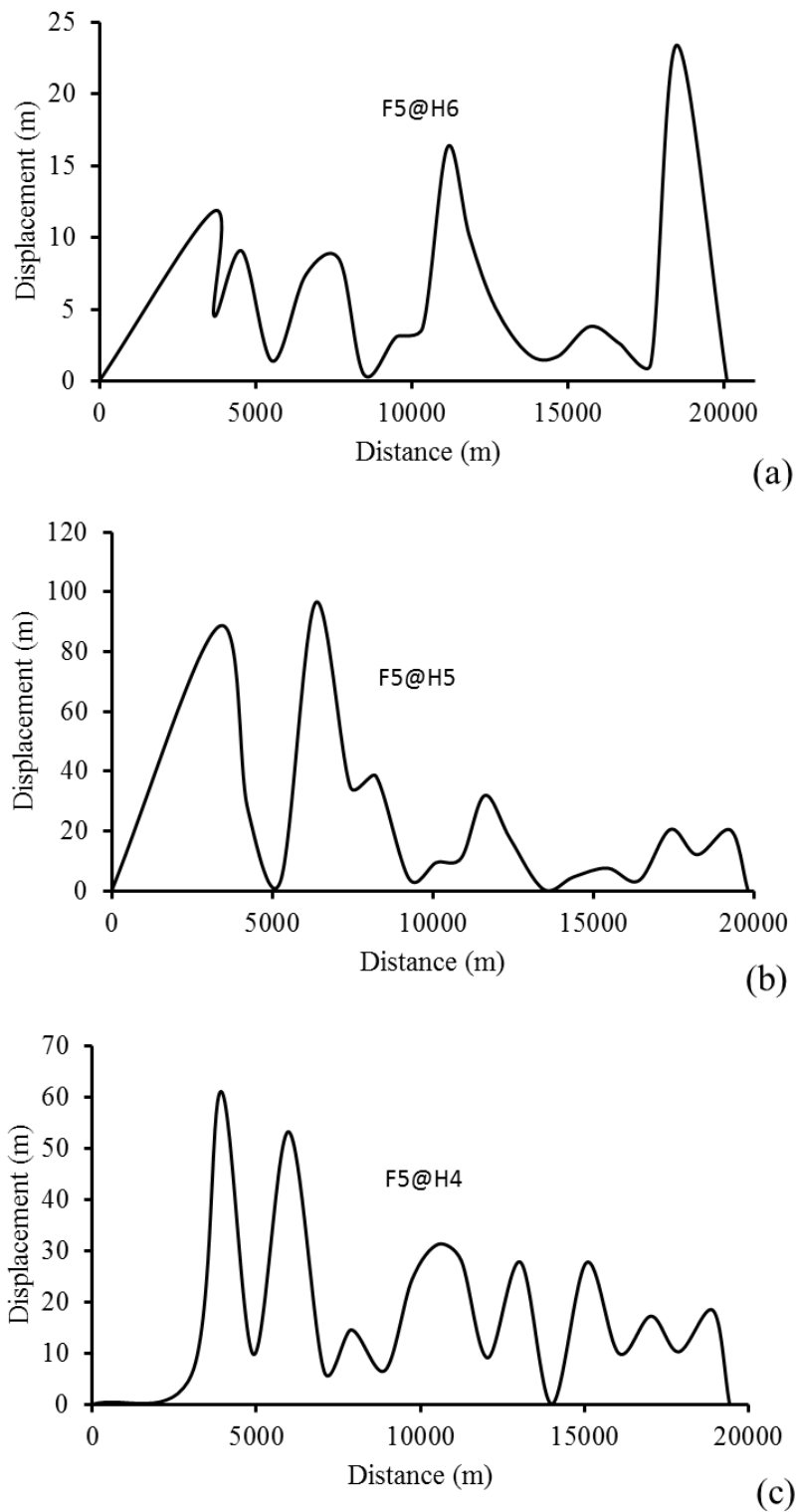
Figure A4 Distance-displacement (t-x) plot of F4 and showing of the profiles along (a) H6, (b) H5 and (c) H4; a general decrease in displacement at larger distances. The profiles are multi skewed C-type profiles.
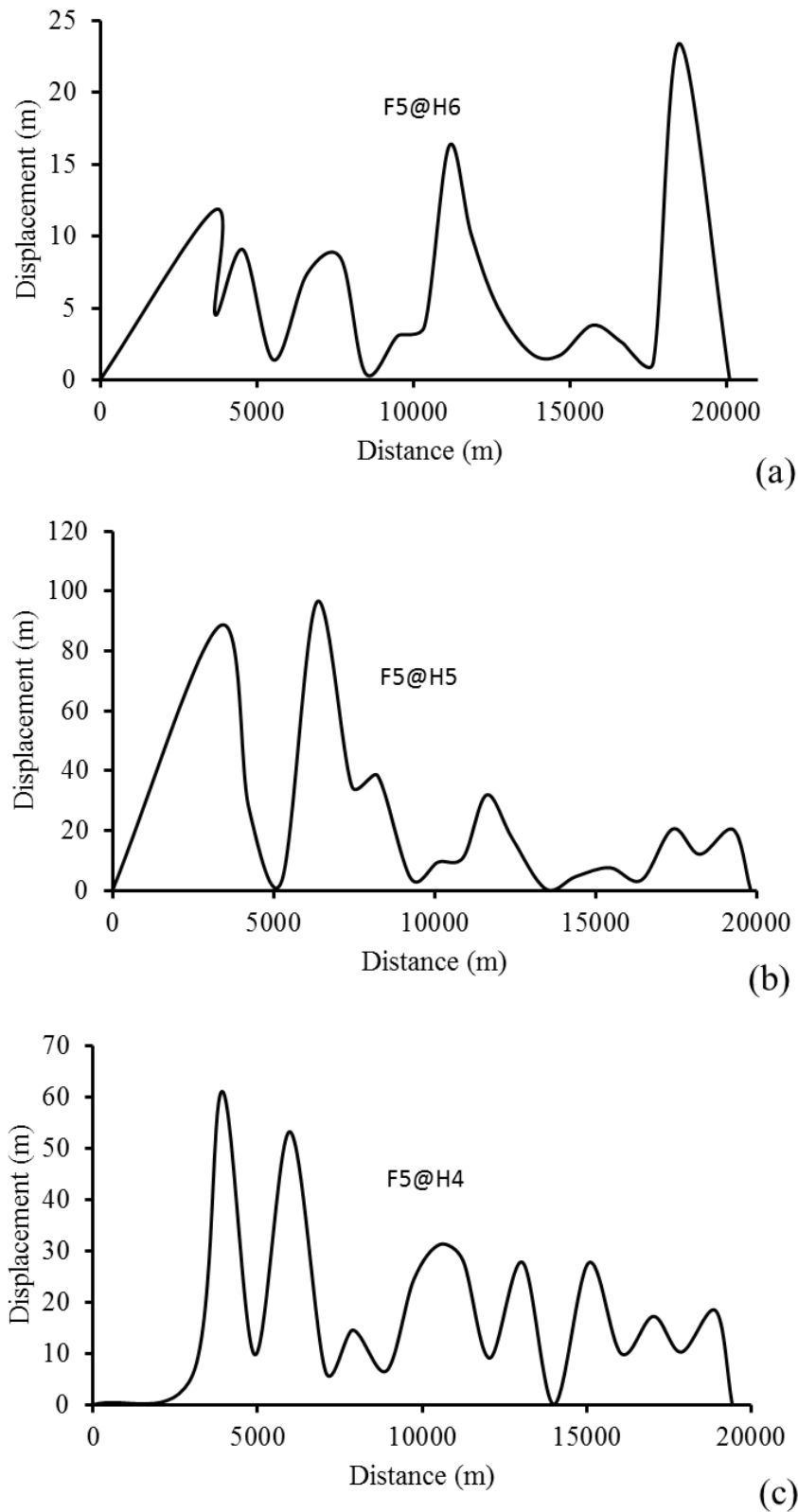
Figure A5 Distance-displacement (t-x) plots of F5 along (a) H6, (b) H5 and (c) H4 showing general decrease in displacement at larger distance on H4 and H5 while on H6 the displacement increase at larger distances. The profiles are in general multi-skewed C-type profiles.
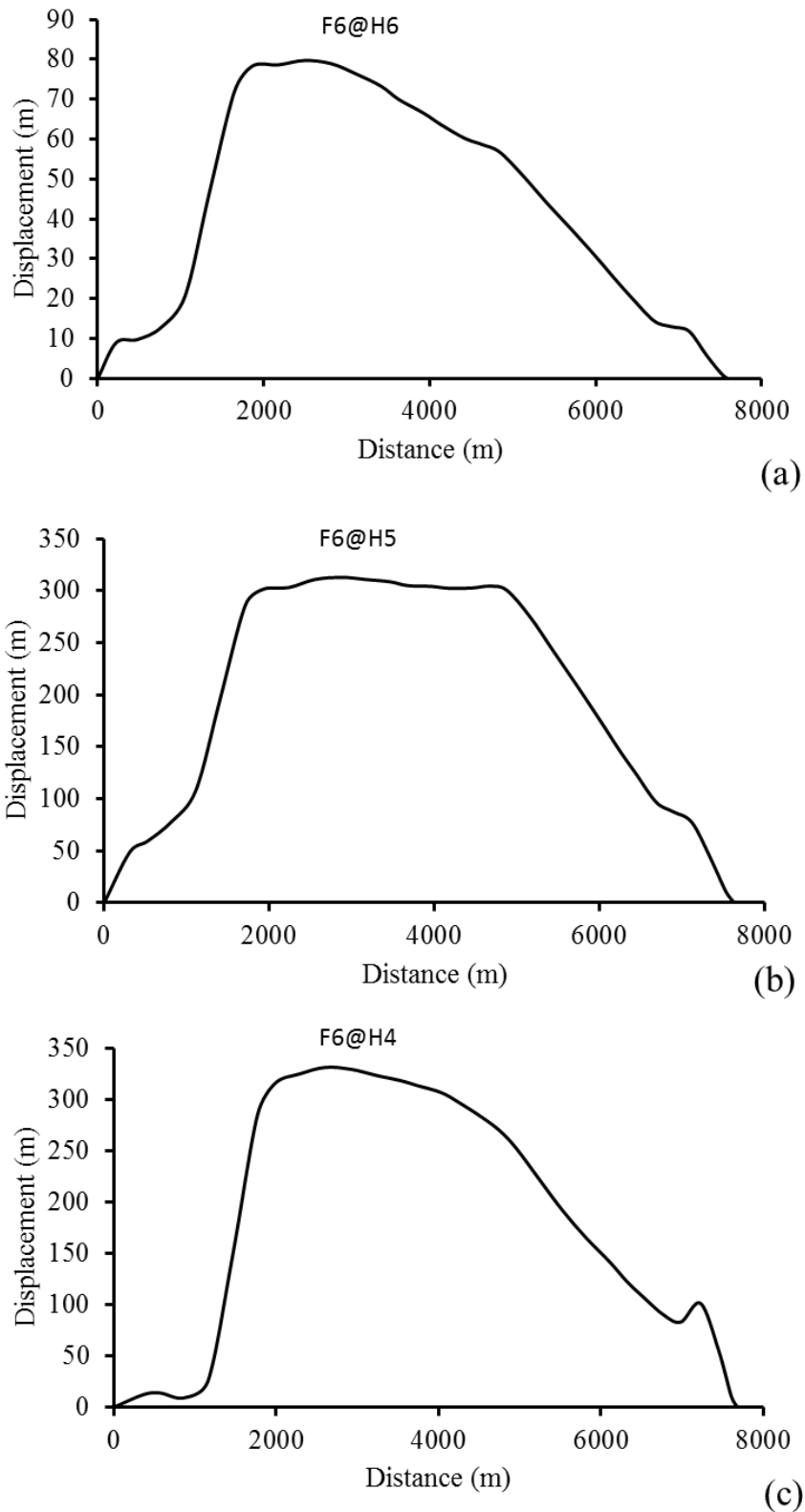
Figure A6 Distance-displacement (t-x) plots for F6 on H6, H5 and H4 shows constantly maximum displacement from 1 to 5 km distance along H7 and H4 and lower displacement along H6. The profile on H6 and H4 are skewed C-type profile while on H5 shows M-type profile.
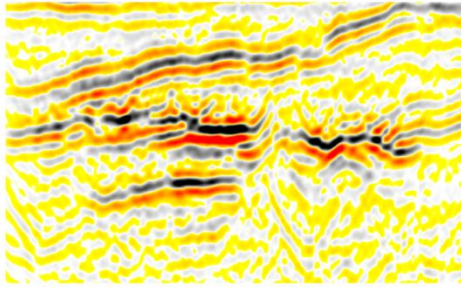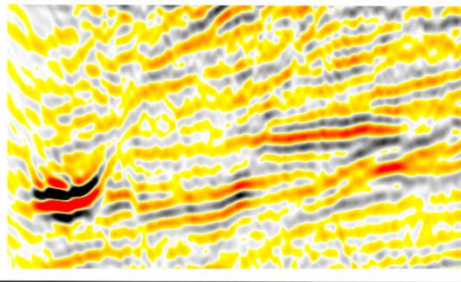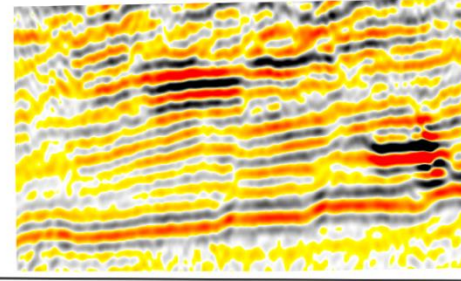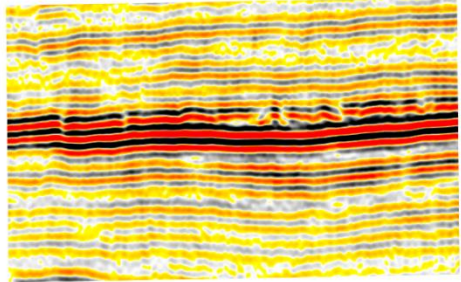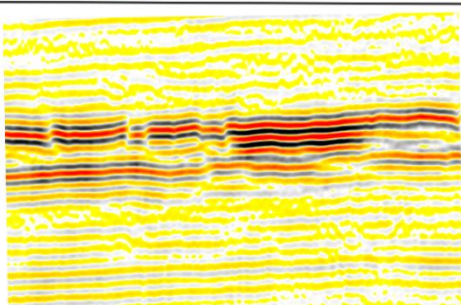
Anomaly	Polarity change as compared to the seabed	Stractual comformability with the background reflectors	Type of the anomaly	Example (VS = 200 ms and HS = 1 km)
Anomaly 1	Reverse in polarity	Unconformable	Fluid accumulations	
Anomaly 2	Reverse in polarity	Unconformable	Fluid accumulations	
Anomaly 3	Reverse in polarity	Unconformable	Fluid accumulations	
Anomaly 4	Reverse in polarity	Conformable	?	
Anomaly 5	Reverse in polarity	Conformable	?	

Figure A7 Summary for A1 to A5 , the criteria used for identification of the fluid type. Anomalies 4 and 5 can be flat spot or any static fluid accumulations/
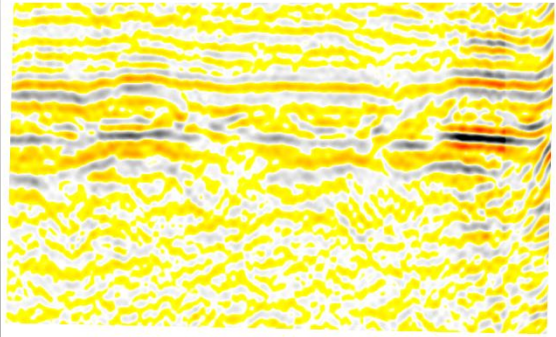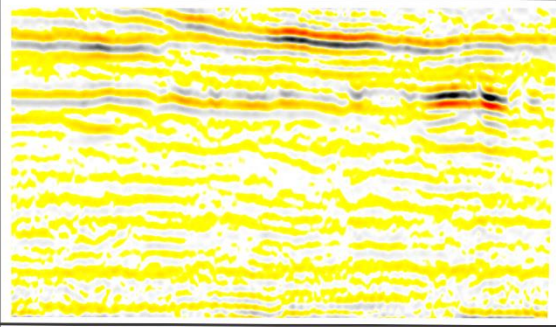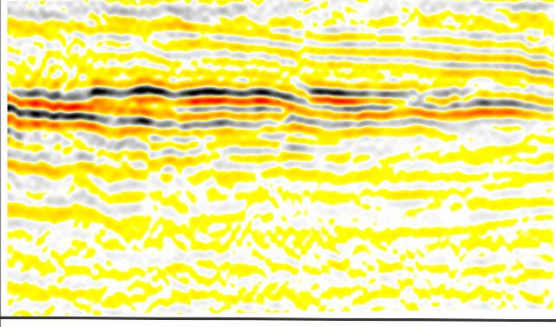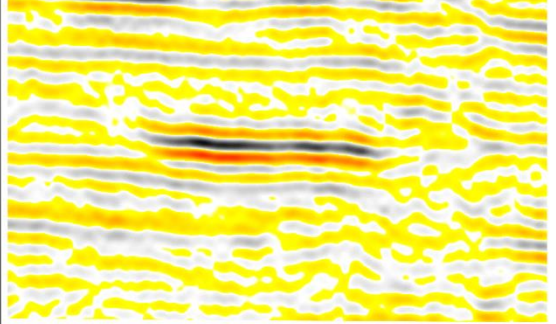
Anomaly	Polarity change as compared to the seabed	Stractual comformability with the background reflectors	Type of the anomaly	Example (VS = 200 ms and HS = 1 km)
Anomaly 6	Reverse in polarity	Unconformable	Fluid accumulations	
Anomaly 7	Reverse in polarity	Unconformable	Fluid accumulations	
Anomaly 8	Reverse in polarity	Unconformable	Fluid accumulations	
Anomaly 9	Reverse in polarity	Conformable	?	

Figure A8 Summary for A6 to A9 , the criteria used for identification of the fluid type. Anomaly 9 can be flat spot or any static fluid accumulations/